Gezamenlijke opleiding UHasselt en KU Leuven

Universiteit Hasselt | Campus Diepenbeek | Faculteit Industriële Ingenieurswetenschappen | Agoralaan Gebouw H - Gebouw B | BE 3590 Diepenbeek

Universiteit Hasselt | Campus Diepenbeek | Agoralaan Gebouw D | BE 3590 Diepenbeek
Universiteit Hasselt | Campus Hasselt | Martelarenlaan 42 | BE 3500 Hasselt

---

Faculteit Industriële Ingenieurswetenschappen

master in de industriële wetenschappen: chemie

Masterthesis

Optimizing ultrasonic spray coating for depositing a superhydrophobic coating with PVDF and nanoparticles

Wout Ruytinx
Scriptie ingediend tot het behalen van de graad van master in de industriële wetenschappen: chemie

PROMOTOR :
Prof. dr. ir. Wim DEFERME

BEGELEIDER :
ing. Tobias CORTHOUTS

2022
2023

Faculteit Industriële Ingenieurswetenschappen

master in de industriële wetenschappen: chemie

Masterthesis

Optimizing ultrasonic spray coating for depositing a superhydrophobic coating with PVDF and nanoparticles

Wout Ruytinx

Scriptie ingediend tot het behalen van de graad van master in de industriële wetenschappen: chemie

PROMOTOR :

Prof. dr. ir. Wim DEFERME

BEGELEIDER :

ing. Tobias CORTHOUTS

Preface

After completing my degree in Engineering Sciences in secondary school, I decided to enrol in the shared course of Industrial Engineering from UHasselt and KULeuven. This is because I have always been fascinated by science, but I found it challenging to narrow down my interests to a specific field. This transition from secondary school was too big in my case, so I quit this program after the first year. I then decided to base my next education on my highest grade obtained and began studying for a professional bachelor's degree in chemistry at UCLL.

As part of my professional bachelor's degree, I completed an internship at a company of my choice, where I worked as an employee and conducted research for my final paper. Although I found the work I was doing disappointing, given that I had studied for four years. I later discovered an option to bridge to Master of Chemical Engineering Technology, which was only a two-year program, and I decided to take this opportunity.

With my experience, I was keen to try a master's thesis opportunity with a research group. I was fortunate to be accepted into the FME group at Imo-imomec, where there was an opening for a master’s student to work on coatings. As my internship from my professional bachelor's degree also dealt with surface treatments, this seemed like an excellent fit for me.

During my time at Imo-imomec, I had the opportunity to work in the lab with talented individuals who were always available to answer my questions. I would like to thank my internal and external promotor, Prof. dr. ir. Wim Deferme, for the opportunities he provided for my professional growth, and my supervisor, Ing. Tobias Corthouts, for his guidance. I am also grateful to the entire FME group for creating a pleasant working environment because, as the saying goes, "it takes a village to raise a child."

I am delighted that I was able to complete my master's thesis at Imo-imomec. I have never enjoyed working for school as much as I did during this project, and I hope that my research has made a positive contribution to the FME group.

Content

Preface **1**

List of tables **5**

List of figures **7**

Glossary **13**

Abstract **15**

Abstract in Dutch **17**

1. Introduction **19**

- 1.1 Context 21
- 1.2 Problem statement/research question 21
- 1.3 Research objectives 22

2. Literature study **23**

- 2.1 Coating techniques 23
  - 2.1.1 Dip coating 23
  - 2.1.2 Spin coating 23
  - 2.1.3 Pressurised spray coating 24
  - 2.1.4 Ultrasonic spray coating 24
  - 2.1.5 Influence parameters USSC 25
- 2.2 Polymers 29
  - 2.2.1 PVP 29
  - 2.2.2 PLA 30
  - 2.2.3 PVDF 30
- 2.3 Nanoparticles 31
  - 2.3.1 SiO_2 31
  - 2.3.2 TiO_2 31
  - 2.3.3 Hydrolysis 32
- 2.4 Solvents 33
  - 2.4.1 Acetone 33
  - 2.4.2 Chloroform 33
  - 2.4.3 Ethanol 34
- 2.5 Substrates 34

2.6 Hydrophobicity 35

2.6.1 Surface energy 35

2.6.2 Surface roughness 36

2.8 Effects 37

2.8.1 Contact line pinning 37

2.8.2 Aggregation of nanoparticles 38

2.9 Analysis equipment 38

2.9.1 Contact angle measurement system 38

2.9.2 Sliding angle measurement system 39

2.9.3 Profilometer 39

2.9.4 Optical microscope 40

2.9.5 Scanning electron microscopy 41

3. Materials and methods 43

4. Results and discussion 47

4.1 Optimisation USSC 47

4.1.1 Distance nozzle-substrate 48

4.1.2 Pressure shroud gas 51

4.1.3 Flowrate 54

4.1.4 Temperature hotplate 56

4.1.5 Removing dark spots 57

4.1.6 Optimal USSC parameters (2.5 wt% PVDF) 59

4.2 Optimisation of hydrophobic properties 59

4.2.1 PVDF 59

4.2.2 SiO_2 nanoparticles 61

4.2.3 PVDF & SiO_2 hydrophobic nanoparticles 69

4.2.4 PVDF mixed SiO_2 hydrophobic nanoparticles 71

4.2.5 PVDF & PVDF mixed SiO_2 hydrophobic nanoparticles 73

4.3 Self-cleaning properties 74

4.4 Sliding angle 79

4.5 Adhesion properties 79

4.6 SEM 80

4.6.1 Surface ... 80
4.6.2 Cross-section ... 82

5. Conclusion ... 83
Reference list ... 85

List of tables

Table 1: Classification of hydrophobicity 35
Table 2: Parameters of global optimisation... 47
Table 3: Optimisation of hotplate temperature 56
Table 4: Optimal USSC parameters 2.5 wt% PVDF 59
Table 5: Distribution NP for different heights 61
Table 6: Parameters tested layers of PVDF... 74
Table 7: Parameters tested layers of NP... 74
Table 8: Parameters tested layers of PVDF & NP... 75
Table 9: Parameters tested layers of PVDF mixed NP 75
Table 10: Parameters tested layers of PVDF & PVDF mixed NP 75

List of figures

Figure 1: Air spray system ... 21
Figure 2: Working mechanism of dip coating ... 23
Figure 3: Working mechanism of spin coating ... 24
Figure 4: Schematic representation of USSC ... 25
Figure 5: Ultrasonic nozzle ... 25
Figure 6: Comparison of drop distribution pressure and ultrasonic nozzles ... 25
Figure 7: Influence of nozzle distance and substrate temperature on peak edge formation ... 26
Figure 8: Thickness as a function of substrate temperature and nozzle speed for 10 spray passes with 0.5 wt% PVP in water ... 26
Figure 9: Profile scan of 10 spray passes with 0.5 wt% PVP in water for 10 mm/s ... 26
Figure 10: 10 spray passes with 0.5 wt% PVP in water at different temperatures ... 27
Figure 11: 10 spray passes with 0.5 wt% PVP in water at different nozzle speeds ... 28
Figure 12: 10 spray passes with 0.5 wt% PVP in water at different heights ... 28
Figure 13: Formation of droplets ... 29
Figure 14: Chemical structure PVP ... 30
Figure 15: Chemical structure PLA ... 30
Figure 16: Contact angle PVDF ... 31
Figure 17: Nebulizing spray hydrolysis technique ... 32
Figure 18: Reaction of methyltrimethoxysilane ... 32
Figure 19: Influence of different solvents ... 33
Figure 20: Chemical structure acetone ... 33
Figure 21: Chemical structure chloroform ... 34
Figure 22: Chemical structure ethanol ... 34
Figure 23: PVP on different substrates ... 35
Figure 24: Water droplet on a hydrophilic substrate ... 36
Figure 25: Wenzel model ... 36
Figure 26: Cassie-Baxter model ... 37
Figure 27: Contact line pinning ... 38
Figure 28: OCA 15 system from DataPhysics (USA) ... 39
Figure 29: OCA 100 from DataPhysics (Germany) ... 39
Figure 30: Working mechanism contact profilometer ... 40
Figure 31: Dektak XT ... 40
Figure 32: Axiovert 40 MAT (Zeiss) ... 41
Figure 33: Schematic SEM ... 41
Figure 34: Different stacking layers ... 43
Figure 35: Uniform deposition of graphite ... 44
Figure 36: 3D printed 10° angle ... 44
Figure 37: Settings analysis particles ... 45
Figure 38: Initial 9µl droplet ... 45
Figure 39: 9µl droplet before rolling ... 45
Figure 40: 9µl droplet rolling ... 45
Figure 41: 9µl droplet after rolling ... 45
Figure 42: 3.5 cm (5x zoom) ... 48
Figure 43: 3.5 cm (20x zoom) ... 48

Figure 44: 3.5 cm (50x zoom) 48
Figure 45: 4.5 cm (5x zoom) 48
Figure 46: 4.5 cm (20x zoom) 48
Figure 47: 4.5 cm (50x zoom) 48
Figure 48: 5.5 cm (5x zoom) 48
Figure 49: 5.5 cm (20x zoom) 48
Figure 50: 5.5 cm (50x zoom) 48
Figure 51: 6.5 cm (5x zoom) 48
Figure 52: 6.5 cm (20x zoom) 48
Figure 53: 6.5 cm (50x zoom) 48
Figure 54: 7.5 cm (5x zoom) 48
Figure 55: 7.5 cm (20x zoom) 48
Figure 56: 7.5 cm (50x zoom) 48
Figure 57: 8.5 cm (5x zoom) 48
Figure 58: 8.5 cm (20x zoom) 48
Figure 59: 8.5 cm (50x zoom) 48
Figure 60: Ra value for different distances 49
Figure 61: Rt value for different distances 49
Figure 62: Wa value for different distances 49
Figure 63: 0.5 psi (5x zoom) 51
Figure 64: 0.5 psi (20x zoom) 51
Figure 65: 0.5 psi (50x zoom) 51
Figure 66: 1.0 psi (5x zoom) 51
Figure 67: 1.0 psi (20x zoom) 51
Figure 68: 1.0 psi (50x zoom) 51
Figure 69: 1.5 psi (5x zoom) 51
Figure 70: 1.5 psi (20x zoom) 51
Figure 71: 1.5 psi (50x zoom) 51
Figure 72: 2.0 psi (5x zoom) 51
Figure 73: 2.0 psi (20x zoom) 51
Figure 74: 2.0 psi (50x zoom) 51
Figure 75: 2.5 psi (5x zoom) 51
Figure 76: 2.5 psi (20x zoom) 51
Figure 77: 2.5 psi (50x zoom) 51
Figure 78: 3.0 psi (5x zoom) 51
Figure 79: 3.0 psi (20x zoom) 51
Figure 80: 3.0 psi (50x zoom) 51
Figure 81: 3.5 psi (5x zoom) 51
Figure 82: 3.5 psi (20x zoom) 51
Figure 83: 3.5 psi (50x zoom) 51
Figure 84: Ra value for different shroud pressures 52
Figure 85: Rt value for different shroud pressures 52
Figure 86: Wa value for different shroud pressures 52
Figure 87: 0.10 ml/min (5x zoom) 54
Figure 88: 0.10 ml/min (20x zoom) 54
Figure 89: 0.10 ml/min (50x zoom) 54

Figure 90: 0.25 ml/min (5x zoom) 54
Figure 91: 0.25 ml/min (20x zoom) 54
Figure 92: 0.25 ml/min (50x zoom) 54
Figure 93: 0.50 ml/min (5x zoom) 54
Figure 94: 0.50 ml/min (20x zoom) 54
Figure 95: 0.50 ml/min (50x zoom) 54
Figure 96: 1.00 ml/min (5x zoom) 54
Figure 97: 1.00 ml/min (20x zoom) 54
Figure 98: 1.00 ml/min (50x zoom) 54
Figure 99: 1.50 ml/min (5x zoom) 54
Figure 100: 1.50 ml/min (20x zoom) 54
Figure 101: 1.50 ml/min (50x zoom) 54
Figure 102: 2.00 ml/min (5x zoom) 54
Figure 103: 2.00 ml/min (20x zoom) 54
Figure 104: 2.00 ml/min (50x zoom) 54
Figure 105: 2.50 ml/min (5x zoom) 54
Figure 106: 2.50 ml/min (20x zoom) 54
Figure 107: 2.50 ml/min (50x zoom) 54
Figure 108: Ra value for different flowrates 55
Figure 109: Rt value for different flowrates 55
Figure 110: Wa value for different flowrates 55
Figure 111: Ra value for different hotplate temperatures 56
Figure 112: Rt value for different hotplate temperatures 57
Figure 113: Wa value for different hotplate temperatures 57
Figure 114: Control sample (5x zoom) 58
Figure 115: Control sample (20x zoom) 58
Figure 116: Post-spraying acetone (5x zoom) 58
Figure 117: Post-spraying acetone (20x zoom) 58
Figure 118: Filtered 450 nm (5x zoom) 58
Figure 119: Filtered 450 nm (20x zoom) 58
Figure 120: Curing 150°C 15' (5x zoom) 58
Figure 121: Curing 150°C 15' (20x zoom) 58
Figure 122: Curing 160°C 15' (5x zoom) 58
Figure 123: Curing 160°C 15' (20x zoom) 58
Figure 124: Curing 170°C 15' (5x zoom) 58
Figure 125: Curing 170°C 15' (20x zoom) 58
Figure 126: PVDF stacking layer 59
Figure 127: Thickness for different layers with 2.5 wt% PVDF 59
Figure 128: CA for different layers with 2.5 wt% PVDF 60
Figure 129: Thickness for different concentrations of 20 layers PVDF 60
Figure 130: CA for different concentrations of 20 layers PVDF 61
Figure 131: Nanoparticles stacking layer 61
Figure 132: Visual distribution of NP on different heights 62
Figure 133: Traditional sessile drop technique 62
Figure 134: Used method for CA measurements 63
Figure 135: CA for different flowrates of 10 - 20 nm SiO_2 hydrophobic 64

Figure 136: CA for different concentrations of 10 - 20 nm SiO_2 hydrophobic ... 64
Figure 137: CA for different layers NP ... 65
Figure 138: 10 - 20 nm SiO_2 250x ... 67
Figure 139: 10 - 20 nm SiO_2 1kx ... 67
Figure 140: 10 - 20 nm SiO_2 5kx ... 67
Figure 141: 10 - 20 nm SiO_2 10kx ... 67
Figure 142: 10 - 20 nm SiO_2 50kx ... 67
Figure 143: 500 nm SiO_2 250x ... 67
Figure 144: 500 nm SiO_2 1kx ... 67
Figure 145: 500 nm SiO_2 5kx ... 67
Figure 146: 500 nm SiO_2 10kx ... 67
Figure 147: 500 nm SiO_2 50kx ... 67
Figure 148: 20 - 30 nm hydrolyse 250x ... 67
Figure 149: 20 - 30 nm hydrolyse 1kx ... 67
Figure 150: 20 - 30 nm hydrolyse 5kx ... 67
Figure 151: 20 - 30 nm hydrolyse 10kx ... 67
Figure 152: 20 - 30 nm hydrolyse 50kx ... 67
Figure 153: 300 nm hydrolyse 250x ... 68
Figure 154: 300 nm hydrolyse 1kx ... 68
Figure 155: 300 nm hydrolyse 5kx ... 68
Figure 156: 300 nm hydrolyse 10kx ... 68
Figure 157: 300 nm hydrolyse 50kx ... 68
Figure 158: 10 - 20 nm hydrophobic 250x ... 68
Figure 159: 10 - 20 nm hydrophobic 1kx ... 68
Figure 160: 10 - 20 nm hydrophobic 5kx ... 68
Figure 161: 10 - 20 nm hydrophobic 10kx ... 68
Figure 162: 10 - 20 nm hydrophobic 50kx ... 68
Figure 163: Droplet 250x ... 68
Figure 164: Droplet 1kx ... 68
Figure 165: Droplet 5kx ... 68
Figure 166: Droplet 10kx ... 68
Figure 167: Droplet 50kx ... 68
Figure 168: PVDF & hydrophobic NP stacking layer ... 69
Figure 169: CA with different layers 1 g/l NP on top of PVDF ... 70
Figure 170: CA for different concentrations of nanoparticles ... 70
Figure 171: CA with different layers 5 g/l NP on top of PVDF ... 71
Figure 172: PVDF mixed hydrophobic NP stacking layer ... 71
Figure 173: CA for different mixed layers of 1 g/l NP and 2.5 wt% PVDF ... 72
Figure 174: CA for increasing concentration NP with 2.5 wt% PVDF ... 72
Figure 175: CA for different mixed layers of 25 g/l NP and 2.5 wt% PVDF ... 73
Figure 176: PVDF & PVDF mixed NP stacking layer ... 73
Figure 177: CA for depositing mixed PVDF & NP on optimised PVDF ... 74
Figure 178: PVDF & NP & acetone ... 75
Figure 179: PVDF & NP & heating ... 75
Figure 180: Purified glass before cleaning ... 77
Figure 181: PVDF before cleaning ... 77

Figure 182: NP before cleaning 77
Figure 183: PVDF & NP before cleaning 77
Figure 184: PVDF mixed NP before cleaning 77
Figure 185: PVDF & PVDF mixed NP before cleaning 77
Figure 186: Post-treatment acetone before cleaning 77
Figure 187: Post-treatment heating before cleaning 77
Figure 188: Purified glass after cleaning 77
Figure 189: PVDF after cleaning 77
Figure 190: NP after cleaning 77
Figure 191: PVDF & NP after cleaning 77
Figure 192: PVDF mixed NP after cleaning 77
Figure 193: PVDF & PVDF mixed NP after cleaning 77
Figure 194: Post-treatment acetone after cleaning 77
Figure 195: Post-treatment heating after cleaning 77
Figure 196: Graphite reduction 78
Figure 197: Sliding angle for different coatings 79
Figure 198: Scratch on NP 80
Figure 199: Scratch on PVDF mixed NP 80
Figure 200: Nanoparticles 1kx 81
Figure 201: Nanoparticles 20kx 81
Figure 202: Nanoparticles 100kx 81
Figure 203: PVDF & NP 1kx 81
Figure 204: PVDF & NP 20kx 81
Figure 205: PVDF & NP 100kx 81
Figure 206: PVDF mixed NP 1kx 81
Figure 207: PVDF mixed NP 20kx 81
Figure 208: PVDF mixed NP 100kx 81
Figure 209: PVDF & PVDF mixed NP 1kx 81
Figure 210: PVDF & PVDF mixed NP 20kx 81
Figure 211: PVDF & PVDF mixed NP 100kx 81
Figure 212: Post-treatment acetone after cleaning 1kx 81
Figure 213: Post-treatment acetone after cleaning 20kx 81
Figure 214: Post-treatment acetone after cleaning 100kx 81
Figure 215: Post-treatment heating after cleaning 1kx 82
Figure 216: Post-treatment heating after cleaning 20kx 82
Figure 217: Post-treatment heating after cleaning 100kx 82
Figure 218: Nanoparticles 300x 82
Figure 219: Post-treatment acetone after cleaning 35x 82

Glossary

Å	Angstrom (1.0 x 10^{-10}m)
CA	Contact angle
d	Diameter
DLS	Dynamic light scattering
f	Frequency
FME	Functional Material Engineering
frac	The degree of contact between the droplet and the rough surface
NP	Nanoparticles
PLA	Polyactide
PVDF	Polyvinylidene fluoride
PVP	Polyvinylpyrrolidone
SEM	Scanning electron microscopy
USSC	Ultrasonic spray coating
γ	Surface energy
θ	Contact angle of the droplet on a flat surface
θ^*	Contact angle of the droplet on a rough surface
ρ	Density
Σ	Surface tension

Abstract

Typically, air spray systems are utilized for the application of coatings. However, a significant amount of ink is being wasted due to inefficiency of this technique. The excessive speed at which the ink is dispensed makes it much of it recoil off the substrate. In contrast, an ultrasonic spray system minimizes material wastage due to its ability to deliver the ink at a lower speed. The main objective of this study is to formulate a superhydrophobic coating while minimizing material loss during the application process. This is pursued through the exploration and implementation of various stacking methods.

The composition consists of PVDF and/or SiO_2 nanoparticles (10-20 nm, 500 nm, 10-20 nm made hydrophobic, 20-30 nm hydrolysis formed, 300 nm hydrolysis formed). The glass substrates are provided with various stacks and combinations of coatings, after which an evaluation is conducted to assess their hydrophobicity based on contact angle measurements, adhesion properties using a tape test, and self-cleaning efficacy using graphite powder. Additionally, microscopic imaging is employed to analyse the coating visually.

The study indicates that the highest contact angle is achieved through the utilization of solely nanoparticles as coating. Here, a contact angle of 160° was attained. However, this coating exhibits low adhesion properties. If these nanoparticles are combined with PVDF, the adhesion strength increases sharply while still maintaining a contact angle of 150°. However, this requires a high concentration of nanoparticles.

Abstract in Dutch

Vaak worden luchtspray-systemen gebruikt voor het aanbrengen van coatings. Er wordt echter een grote hoeveelheid inkt verspild. De hoge snelheid waarmee de inkt wordt aangebracht, zorgt ervoor dat een groot deel van het substraat afspringt. Een ultrasoon sproeisysteem daarentegen minimaliseert deze verspilling doordat de inkt met een lage snelheid kan afgeven. Het hoofddoel van deze studie is het formuleren van een superhydrofobe coating terwijl het materiaalverlies wordt geminimaliseerd. Dit wordt nagestreefd door middel van het implementeren van verschillende stapelmethoden.

De samenstelling bestaat uit PVDF en/of SiO_2-nanopartikels (10-20 nm, 500 nm, 10-20 nm hydrofoob, 20-30 nm door hydrolyse gevormd, 300 nm door hydrolyse gevormd). De glazen substraten worden voorzien van verschillende stapels van coatings, waarna een evaluatie wordt uitgevoerd om hydrofobiciteit te beoordelen op basis van contacthoekmetingen, adhesie-eigenschappen met behulp van een tape-test, en zelfreinigende eigenschappen met behulp van grafietpoeder. Daarnaast wordt microscopische beeldvorming gebruikt om de coating visueel te analyseren.

Het onderzoek geeft aan dat de hoogste contacthoek wordt bereikt door enkel nanopartikels als coating te gebruiken. Hierbij werd een contacthoek van 160° bereikt. Echter, deze coating vertoont lage adhesie-eigenschappen. Als deze nanopartikels worden gecombineerd met PVDF, neemt de adhesie sterk toe, terwijl een contacthoek van 150° behouden blijft. Dit vereist echter een hoge concentratie van nanopartikels.

1. Introduction

1.1 Context

In industry, manufactured products are typically furnished with coatings that confer positive attributes upon the product. The most widely recognized and prevalent type is the anti-corrosion coating for metals, while an equally significant but lesser-known coating is the anti-ice coating for aircraft. Each coating is distinctive and can be tailored to manifest particular properties or combinations thereof. As an illustration, solar panels are endowed with a transparent and self-cleaning layer [1].

This study aims to develop coatings that possess superhydrophobic properties, good adhesion and self-cleaning capabilities. The research is being conducted in collaboration with the Functional Material Engineering (FME) research group located at Imo-imomec, UHasselt, which is also investigating coatings for additive manufacturing.

Typically, an air spray system, such as an air spray gun, is employed to administer a coating, which can manifest in various forms but generally operates on a comparable principle. The procedure entails subjecting the liquid coating to a gas of high pressure, generally ranging between 15 and 50 psi. This results in the coating being expelled from the apparatus at a high velocity. Subsequently, upon exiting the device, the coating experiences deceleration due to air resistance, leading to the formation of small droplets that eventually lead to a mist before settling on the substrate (Figure 1) [2]–[5].

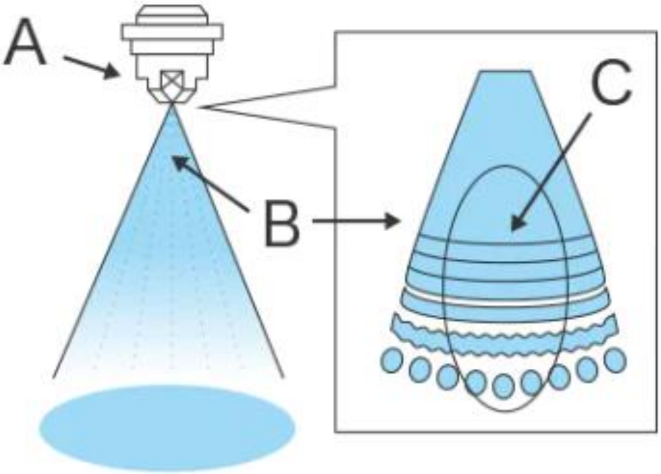

Figure 1: Air spray system A. nozzle B. Coating liquid C. atomization due to air resistance [5]

1.2 Problem statement/research question

The use of an air spray system results in a suboptimal outcome, as only 25-50% of the dispersed coating liquid effectively reaches the intended substrate, leading to an unwanted increase in material cost. This inefficiency is primarily due to the imprecise direction of the coating onto the substrate and the occurrence of bounce-back. The latter happens when droplets land on the substrate too quickly, bouncing off the surface and generating environmental waste. Furthermore, this method generates droplets of varying sizes, ranging from 0 to 130 μm [5]–[7].

A coating comprised solely of PVDF (polyvinylidene fluoride) exhibits a maximum water contact angle of 100°, indicating its hydrophobic nature. However, it falls short of achieving superhydrophobic properties (>150°). Consequently, the absence of a self-cleaning effect on the surface layer leads to the accumulation of impurities. Additionally, it is essential to enhance the contact angle while minimizing any significant reduction in substrate adhesion. This will ensure that the coating's durability aligns with that of the underlying substrate [8].

1.3 Research objectives

The objective of this research is to achieve a fully uniform coating that fulfils the criteria for superhydrophobicity, characterized by a minimum contact angle of 150° with water. The investigation focuses on enhancing this contact angle through the incorporation of silica nanoparticles into the coating. Various types of silica nanoparticles are being considered for this study.

Furthermore, it is imperative for the final coating to exhibit long-term durability in tape tests. This assessment is crucial to ascertain that the hydrophobic properties endure over the substrate's lifespan. Additionally, the coating should effectively prevent impurity accumulation when subjected to rinsing with demineralized water.

2. Literature study

2.1 Coating techniques

2.1.1 Dip coating

Dip coating is a process in which a substrate is immersed at a constant speed in ink for a predetermined amount of time, and then withdrawn from the liquid at a constant speed to create a wet coating on the submerged part. The solvent is subsequently dried to form a thin coating on the substrate (Figure 2). The ink used in this process is typically low in viscosity, allowing for excess ink to be removed from the substrate when it is withdrawn. However, the success of this process depends on various factors such as immersion time, withdrawal speed, number of dipping cycles, solution composition, concentration, temperature, and environmental humidity [9]–[12].

Dip coating offers several advantages, including simultaneous coating of both sides, uniform coating across surfaces of different sizes, and compatibility with complex shapes. However, a notable drawback arises in the final step, where gravity causes the ink to accumulate on the underside of the material, resulting in a thicker layer upon drying [13].

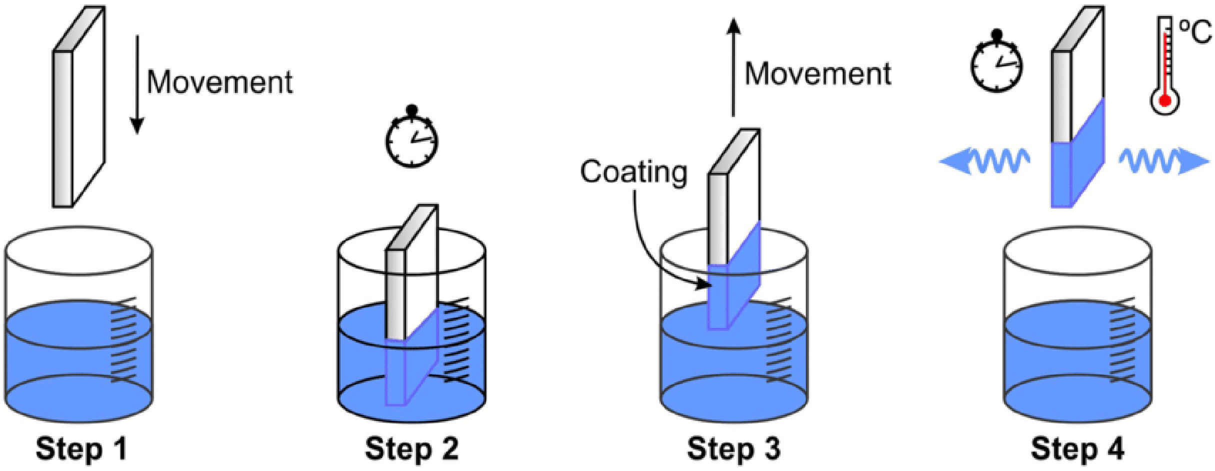

Figure 2: Working mechanism of dip coating [14, p. 16]

2.1.2 Spin coating

Spin coating is a deposition technique whereby a coating material is applied onto a substrate placed on a rotary table, followed by rotation of the table at a specified speed, resulting in uniform spreading of the material due to centrifugal force (Figure 3). The excess material is expelled from the substrate due to the high rotational speed. Subsequently, an evaporation step is performed to remove the remaining solvents. The final thickness of the coating is mainly determined by the viscosity and rotation speed; higher rotation speeds lead to thinner layers. The thickness of the coating typically ranges from micro- to nanometres. However, spin coating has limitations such as low efficiency, with approximately 95-98% of the applied coating lost during rotation, and it is not suitable for large substrates due to practical challenges associated with their rotation. Additionally, this technique can only be applied to flat surfaces [9], [10], [15]–[18].

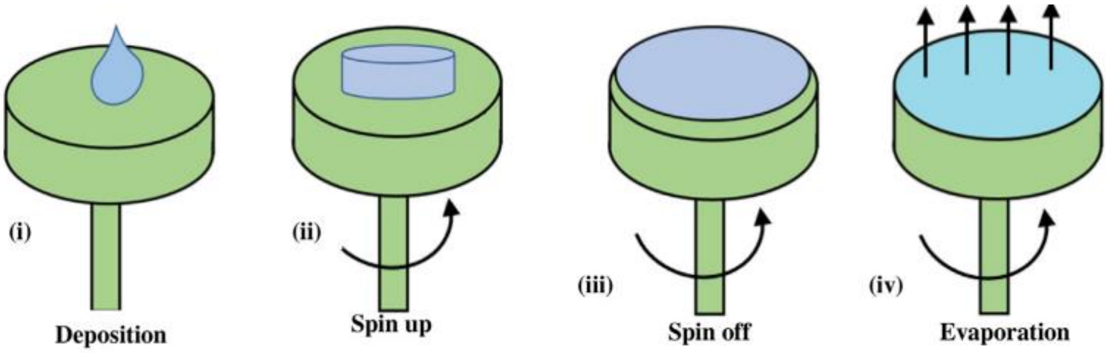

Figure 3: Working mechanism of spin coating [17, p. 51]

2.1.3 Pressurised spray coating

Pressurised spray coating entails subjecting the liquid coating to a gas of high pressure, generally ranging between 15 and 50 psi. This results in the coating being expelled from the apparatus at a high velocity. Subsequently, upon exiting the device, the coating experiences deceleration due to air resistance, leading to the formation of small droplets that eventually lead to a mist before settling on the substrate [2]–[5].

The use of an air spray system results in a suboptimal outcome, as only 25-50% of the dispersed coating liquid effectively reaches the intended substrate, leading to an unwanted increase in material cost. This inefficiency is primarily due to the imprecise direction of the coating onto the substrate and the occurrence of bounce-back. The latter happens when droplets land on the substrate too quickly, bouncing off the surface and generating environmental waste. Moreover, this method generates droplets of varying sizes, ranging from 0 to 130 µm [5]–[7].

2.1.4 Ultrasonic spray coating

In ultrasonic spray coating (USSC) a liquid feed is transported to a nozzle (Figure 4). This nozzle is capable of vibrating with a frequency of 20 kHz - 2 MHz (Figure 5). This causes the thin liquid layer on top off the nozzle to form a standing wave. When the tops of the waves are big enough, a droplet will be released. The kinetic energy these droplets contain is almost equal to zero. Due to this low speed a shroud gas is blown over the nozzle that guides the droplets to the substrate for depositing the coating [6], [8].

The droplets produced by USSC exhibit uniformity in both size and distribution, as illustrated in Figure 6. This phenomenon can be attributed to the low kinetic energy and carrier gas present during deposition, resulting in reduced impact on the substrate. As a result, the droplets can make contact with the substrate in a wetter state, enabling them to effectively fill the substrate's pores. This increased contact area between the droplets and the substrate ultimately leads to improved adhesion [6], [8], [19].

USSC also provides greater control over the deposited layer due to the ability to adjust several parameters. This results in the possibility of achieving the desired coating properties while using minimal amounts of material on a three dimensional object. Consequently, USSC holds significant promise as a technique for producing high-quality coatings while minimizing material consumption and costs [6], [19], [20].

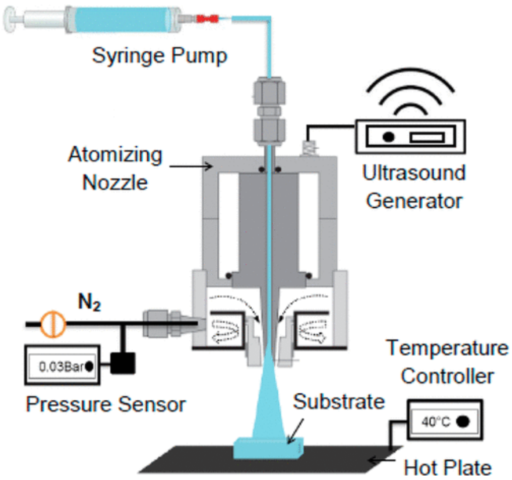

Figure 4: Schematic representation of USSC [20, p. 6]

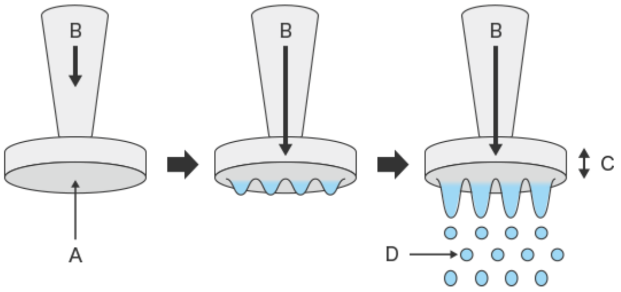

Figure 5: Ultrasonic nozzle with A. Atomization surface B. Coating liquid C. Ultrasonic vibration D. Small, uniform drops [5]

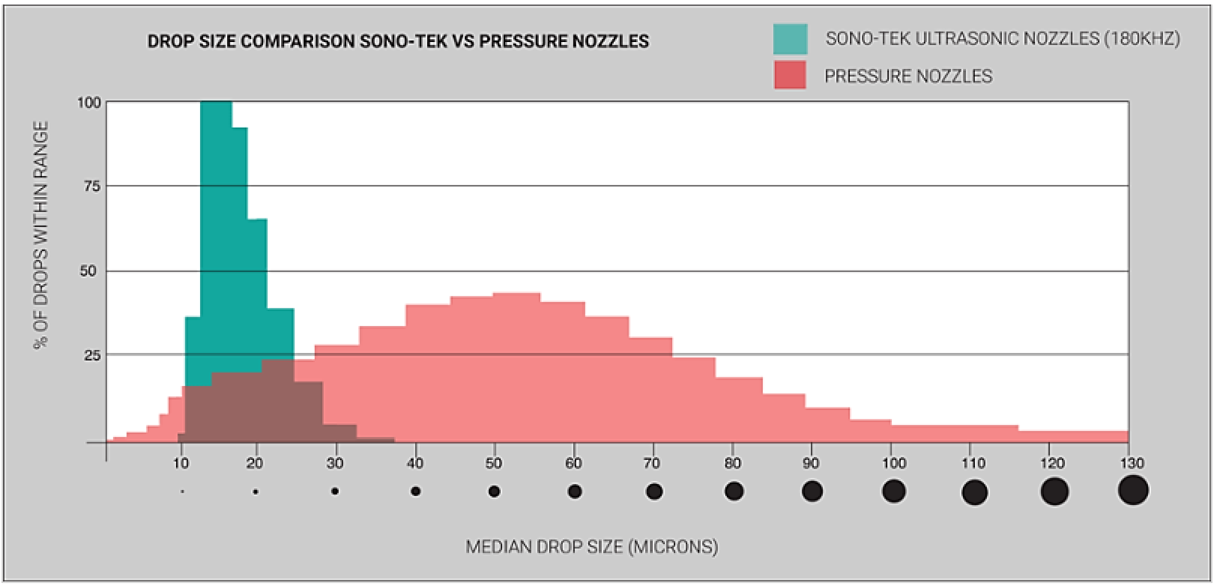

Figure 6: Comparison of drop distribution pressure and ultrasonic nozzles [6]

2.1.5 Influence parameters USSC

The investigation conducted by [20], as depicted in Figure 7, has demonstrated that the temperature and distance between the substrate and nozzle are crucial determinants for the formation of edge peaks. The study has utilized 0.5 wt% polyvinylpyrrolidone (PVP) in water to investigate this phenomenon. The variables mentioned above dictate whether the deposited coating is in the non-peak or peak area. When the coating dries slowly, the accumulation of polymer particles at the edges occurs due to the coffee ring effect. The phenomenon is responsible for the formation of edge peaks and is a result of applying the coating in a too wet state. The deposition of the coating in a dry state prevents this effect, hence eliminating the formation of edge peaks. Spraying at a large distance and/or at high temperature prevents the coffee ring effect. Increasing the nozzle height facilitates the deposition of droplets in a drier state by allowing them to travel a longer distance. Likewise, increasing the temperature leads to faster drying of the arriving droplets, which prevents the coffee ring effect from taking place. It is also noteworthy that the speed at which the nozzle travels does not affect the formation of edge peaks [20].

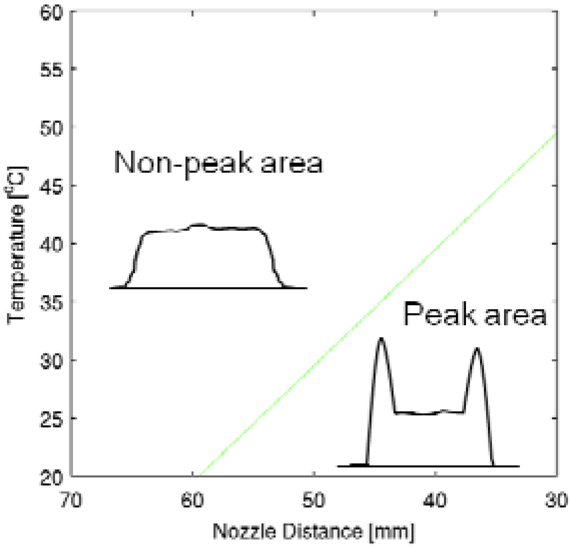

Figure 7: Influence of nozzle distance and substrate temperature on peak edge formation [20, p. 11]

The aforementioned source [20] has investigated the correlation between nozzle speed and coating thickness (Figure 8). The findings indicate that a lower nozzle speed results in an increased thickness, which is a logical consequence of the same flowrate being utilized, resulting in a higher quantity of chemicals being deposited. Furthermore, the research indicates that elevated temperature is also associated with a greater coating thickness, as evidenced in Figure 9 at a spray speed of 10 mm/s. Although the same quantity of material is deposited at each temperature, the profile of the deposited layer indicates that higher temperatures lead to a rough surface with a Gaussian distribution, whereas lower temperatures result in a smoother, more uniform layer (Figure 9). The reason for this uniformity is that the deposited droplets are more wet, which enhances their mobility and allows for coalescence to form a uniform layer on the substrate [20].

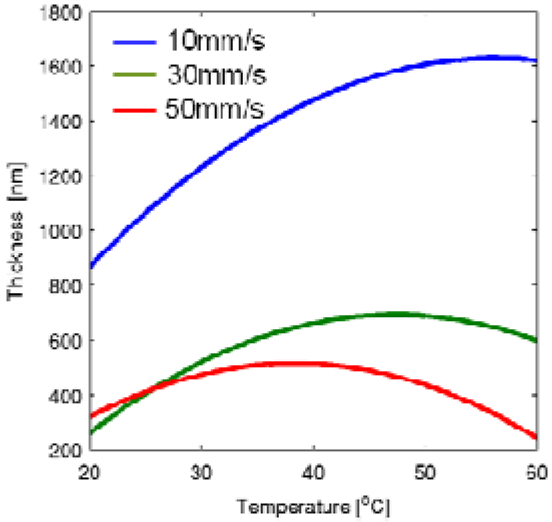

Figure 8: Thickness as a function of substrate temperature and nozzle speed for 10 spray passes with 0.5 wt% PVP in water [20, p. 13]

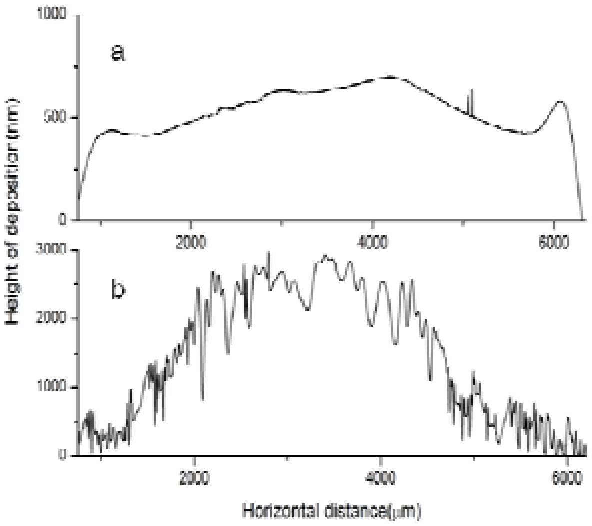

Figure 9: Profile scan of 10 spray passes with 0.5 wt% PVP in water for 10 mm/s at (a) 20°C and (b) 40°C [20, p. 14]

The observed phenomenon of roughness increasing with elevated temperature is also discernible through microscopic examination of the treated surface (Figure 10). Specifically, it is evident that at a temperature of 20°C, the surface appears notably smoother, whereas at higher temperatures, the prevalence of localized dark spots increases. These dark spots are attributed to the application of the coating in a dry state, resulting in the deposition of numerous droplets without sufficient moisture. As a result, at higher temperatures, more droplets are likely to be deposited in a dry state, exacerbating the issue of roughness. Therefore, the optimal temperature for depositing 0.5 wt% PVP in water is determined to be 20°C [20].

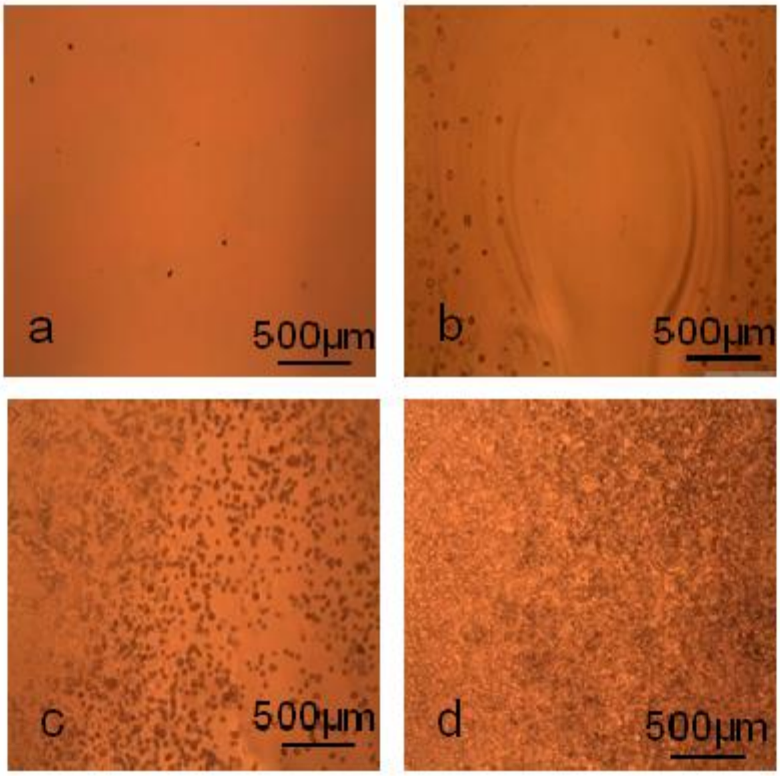

Figure 10: 10 spray passes with 0.5 wt% PVP in water at different temperatures [20, p. 17]

Upon comparing the coverage area of nozzles operating at different speeds, it becomes evident that a speed of 50 mm/s does not provide complete coverage across the entire surface (Figure 11). Conversely, speeds of 10 and 30 mm/s appear to offer adequate coverage. Thus, it is advisable to avoid nozzle speeds exceeding 50 mm/s to achieve a comprehensive layer across the entire surface [20].

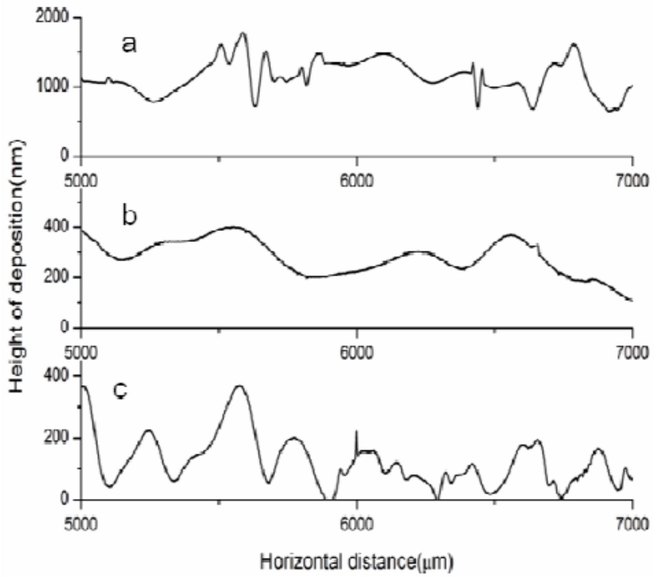

Figure 11: 10 spray passes with 0.5 wt% PVP in water at different nozzle speeds [20, p. 18]

If the nozzle height is adjusted exclusively (Figure 12), it may result in an uneven coating surface when applied at long distances as the droplets can reach the substrate in a relatively dry state. On the other hand, if the distance is too short, the droplets will be excessively wet, resulting in undesirable peaks at the edges. Thus, the optimal height for applying 0.5 wt% PVP in water is a critical factor in achieving a smooth and uniform surface without any peaks at the edges. The ideal height for this specific coating on microscopy glasses is 65 mm, which was determined at a constant temperature of 20°C and a coating speed of 10 mm/s [20].

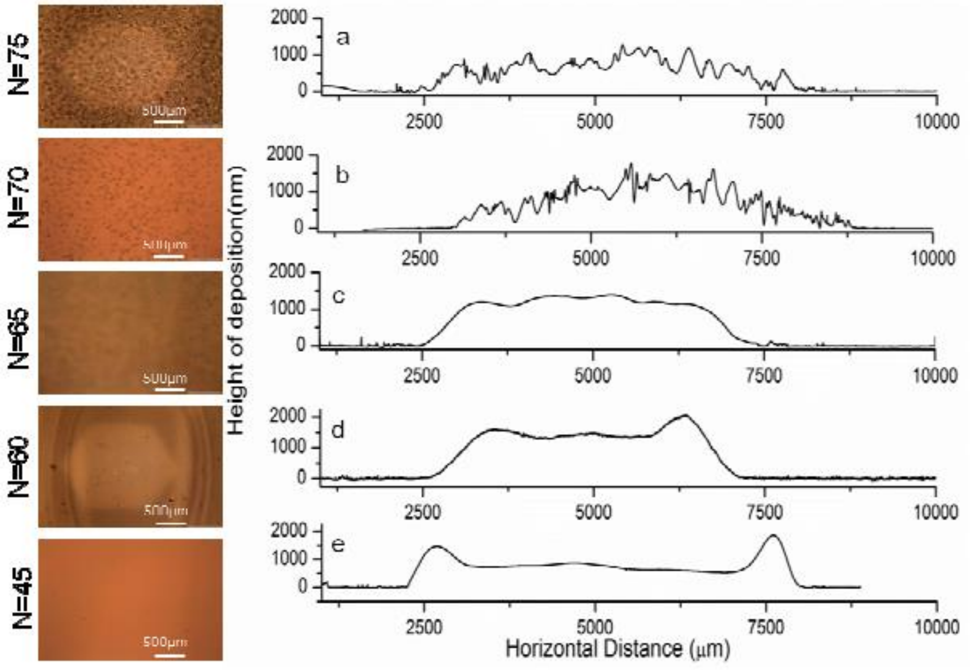

Figure 12: 10 spray passes with 0.5 wt% PVP in water at different heights (N) in mm [20, p. 19]

The size of droplets generated by the USSC is influenced by several parameters. Lang developed an equation that establishes a correlation between these variables and droplet size. The equation is as follows:

$$d_p = 0.34(\frac{8\pi\sigma}{\rho f^2})^{1/3} \tag{1}$$

Where σ represents the surface tension measured in dyne/cm, ρ represents the density of the liquid in g/ml, f corresponds to the frequency of the nozzle in Hz, and d_p represents the diameter of the droplet formed in cm (Figure 13). Despite this equation, it is important to note that the resulting droplets may still vary in size due to potential collisions and agglomeration after formation. Therefore, uniformity among all droplets cannot be guaranteed [19], [21].

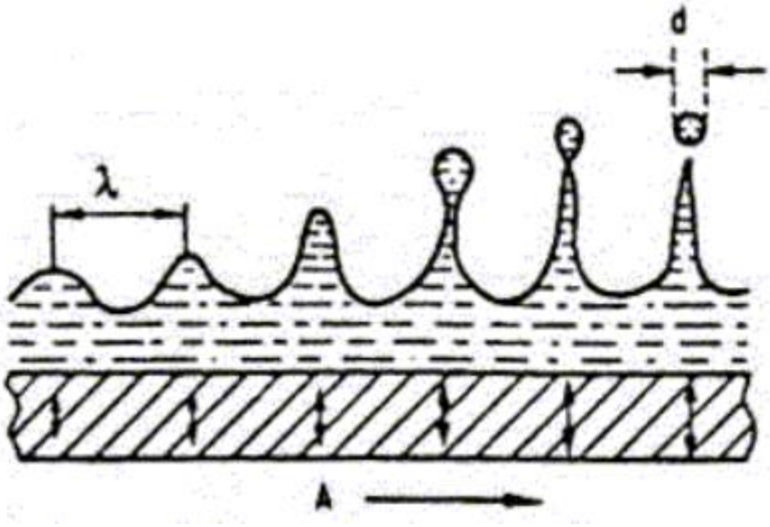

Figure 13: Formation of droplets [22]

2.2 Polymers

2.2.1 PVP

Polyvinylpyrrolidone (PVP) is a water-soluble polymer recognized as a Generally Recognized as Safe (GRAS) substance. It is soluble in methanol and ethanol, and exhibits hygroscopic properties, allowing it to absorb up to 40% of its weight in atmospheric moisture. When used as a coating, PVP demonstrates hydrophilic properties and has poor adhesion. It forms a transparent layer on the surface and has a glass transition temperature of 161.0°C. The chemical structure of PVP is depicted in Figure 14 [23]–[27].

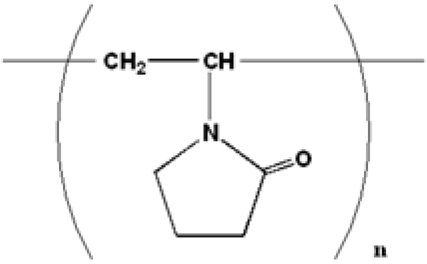

Figure 14: Chemical structure PVP [25]

2.2.2 PLA

Polyactide (PLA) is a thermoplastic polymer renowned for its biodegradability and biocompatibility. Derived from renewable plant resources, PLA serves as a sustainable alternative to conventional plastics, effectively reducing its carbon footprint. It finds valuable applications in 3D printing and food packaging materials. Notably, PLA exhibits a glass transition temperature of 61°C, ensuring its stability under various conditions.

PLA possesses exceptional barrier properties against water, air, and oil, making it an ideal choice for maintaining product integrity. Its film-forming capabilities contribute to the creation of a smooth and uniform surface that is non-porous, providing effective protection against corrosion. In terms of solubility, PLA readily dissolves in dioxane, acetonitrile, chloroform, methylene chloride, 1,1,2-trichloroethane, and dichloroacetic acid. It also exhibits partial solubility in ethylbenzene, toluene, acetone, and tetrahydrofuran. The surface tension of PLA measures at 38 mJ/m^2. Furthermore, PLA is non-toxic, making it a safe choice for various applications. The chemical structure of PLA is depicted in Figure 15 [28]–[35].

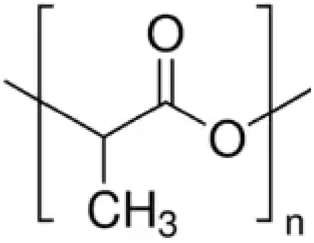

Figure 15: Chemical structure PLA [29]

2.2.3 PVDF

Polyvinylidene fluoride (PVDF) is a thermoplastic polymer known for its exceptional thermal stability (-40°C to 140°C), making it highly suitable for a wide range of industrial applications. It is commonly utilized in the production of micro and ultrafiltration technologies. PVDF offers advantageous characteristics such as wear resistance, corrosion resistance, impact resistance, film forming ability, chemical stability, and high mechanical strength. With a glass transition temperature of -37°C, PVDF exhibits a rubbery state at room temperature and has a melting point of approximately 175°C. Its chemical structure consists of a recurring monomer unit of CH2-CF2.

PVDF is inherently hydrophobic due to its low surface energy, which is demonstrated by a water contact angle of approximately 100° (Figure 16). This hydrophobic nature arises from its surface tension of 15.26 mJ/m^2. In addition to its water-repellent characteristics, PVDF exhibits strong adhesion to aluminium and readily dissolves in acetone. Moreover, PVDF is known for its non-toxic properties [8], [36]–[46].

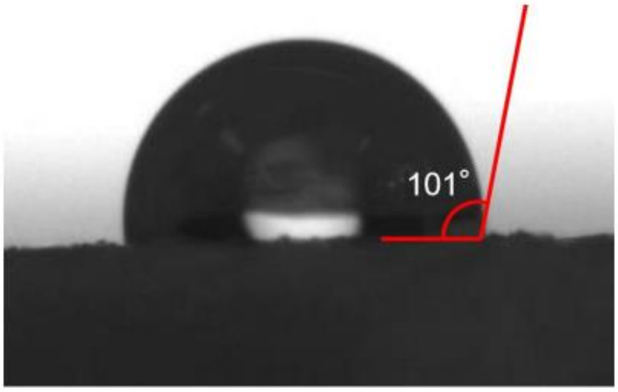

Figure 16: Contact angle PVDF [8, p. 8]

PVDF is the preferred polymer due to its film-forming ability, chemical stability, thermal stability, wear resistance, and hydrophobic properties. Consequently, PVDF is more suitable for this research compared to PVP and PLA mentioned earlier.

2.3 Nanoparticles

Nanoparticles are materials with at least one dimension in the range of 1-100 nm, and can be observed in various forms such as nanoparticles, nanofilms, nanotubes and bulk nanomaterials like dendritic structures. An alternative definition proposes that nanomaterials exhibit a specific surface area to volume ratio equal to or greater than 60 m^2/cm^3. These particles differentiate them from their bulk equivalents and individual ions composing the material. These exceptional characteristics are demonstrated through novel behaviour in areas such as electrical conductivity, reactivity, mechanical strength, and magnetic properties [47]–[49].

2.3.1 SiO_2

Silica nanoparticles under consideration possess a chemical structure of SiO_2 and exhibit the capability of inducing a transition from hydrophobic to superhydrophobic contact angles in a coating. This effect is attributed to their specific roughness, which creates air pockets between the substrate and water droplets. Achieving superhydrophobicity requires that the nanoparticles cover a significant portion (>70%) of the surface area. Moreover, it is feasible to incorporate functional groups onto silica nanoparticles, thereby enhancing their hydrophobic characteristics [50]–[54].

2.3.2 TiO_2

Titanium dioxide nanoparticles exhibit a diameter below 100 nm, rendering them suitable for various applications. In everyday life, these particles are commonly found in sunscreen formulations, contributing to effective UV protection. Notably, titanium dioxide nanoparticles offer the advantage of being chemically and biologically inert, making them a safe and cost-effective choice. Furthermore, they are employed as light catalysts in the conversion of solar energy, leveraging their non-toxic nature and transparent characteristics for efficient energy conversion processes [55]–[58].

The primary role of the nanoparticles in this study is to enhance the contact angle through their unique morphology, which creates small air pockets beneath the deposited droplet. Therefore, the specific type of nanoparticle utilized becomes less critical. Considering the cost-effectiveness and the possibility of surface chemical modification, SiO_2 nanoparticles prove more advantageous compared to TiO_2 nanoparticles, making them a more compelling choice for this research [59].

2.3.3 Hydrolysis

Hydrolysis is a chemical process whereby a molecule undergoes a reaction with a water molecule, resulting in the formation of two distinct molecules. This reaction stands in contrast to a condensation reaction. In a general representation, the hydrolysis reaction can be expressed as follows [76], [77]:

$$AB + HOH \leftrightarrow AH + BOH \tag{2}$$

The hydrolysis SiO_2 nanoparticles utilized in this study originated from Iran. The production process involved the deposition of a methyltrimethoxysilane solution, acting as the precursor, into a water-ethanol mixture containing a small quantity of ammonium. This deposition was accomplished using a nebulizing spray hydrolysis technique. Subsequently, these particles were dispatched to our research group for examination utilizing the USSC. For visual reference, please refer to Figure 17 and Figure 18, which depict the apparatus and the ascending reaction, respectively [78], [79].

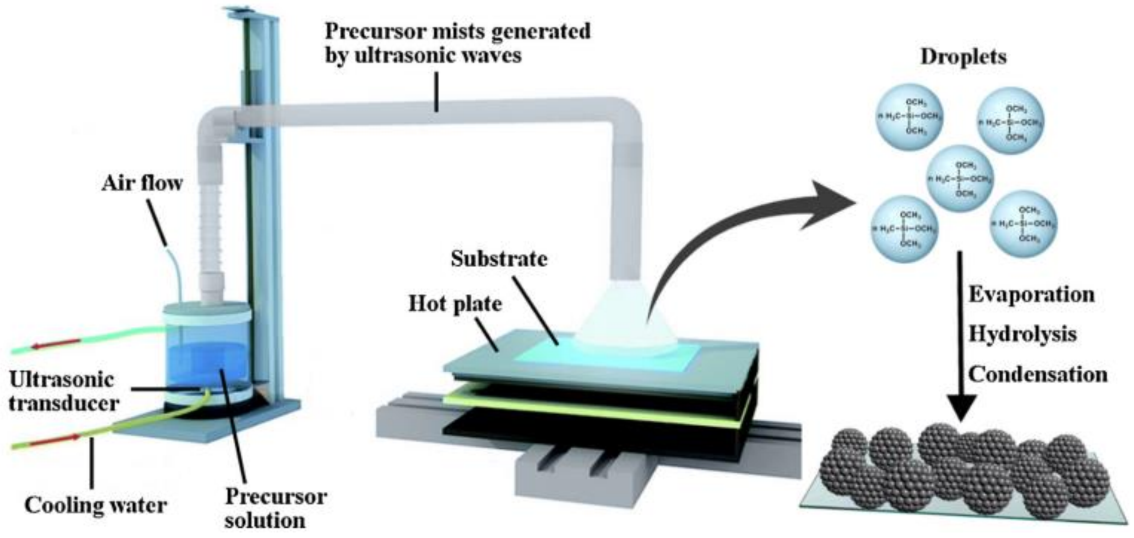

Figure 17: Nebulizing spray hydrolysis technique [79, p. 250]

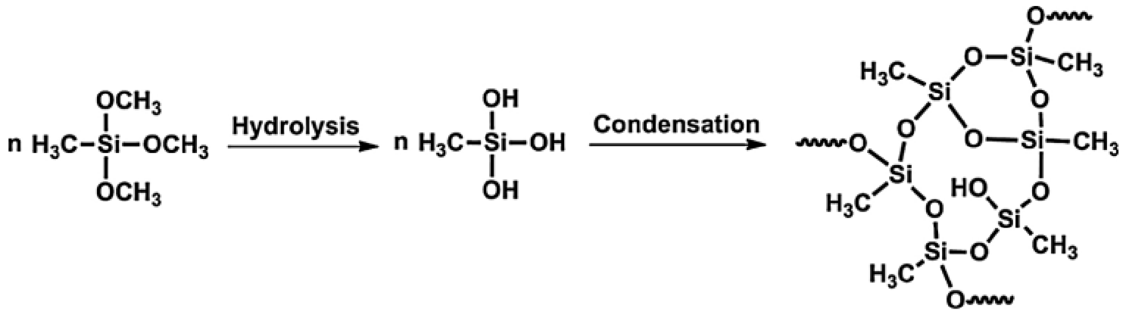

Figure 18: Reaction of methyltrimethoxysilane [79, p. 250]

The silane groups, visible after condensation (Figure 18), provide strong hydrophobic properties to the silica [80].

2.4 Solvents

The selection of a suitable solvent can significantly impact the quality of a coating (Figure 19). A study was conducted to investigate the effect of solvents on coating properties by manipulating the solvent alone for PVP. The solvents under scrutiny were cyclohexane, toluene, and dichloromethane, with varying rates of evaporation [20].

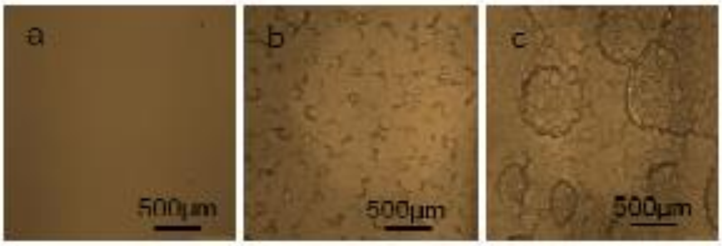

Figure 19: Influence of different solvents (a) cyclohexanone (b) toluene (c) dichloromethane [20, p. 22]

The results indicated that each solvent influenced the coating morphology differently. Rapidly evaporating solvents resulted in rough surfaces, while excessively slow evaporation led to peak formation at the edges. Therefore, selecting an appropriate solvent is critical to achieve the desired coating properties [20].

2.4.1 Acetone

Acetone is a transparent organic compound that exists in a liquid state at room temperature. It is commonly present in nail polish removers. With a boiling point of 56 °C, this flammable liquid falls into the category of volatile organic compounds (VOCs). Inhalation of acetone vapours can potentially lead to Organo Psycho Syndrome, making it crucial to handle the substance with caution. Adequate ventilation, such as a fume hood, should be employed when working with acetone. Furthermore, it is worth noting that acetone is capable of dissolving PVDF. The chemical structure of acetone can be observed in Figure 20 [60]–[62].

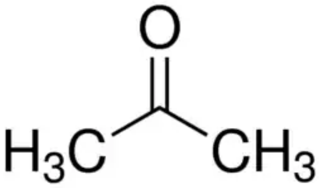

Figure 20: Chemical structure acetone [63]

2.4.2 Chloroform

Chloroform (Trichloromethane) is a colourless liquid compound that remains in a liquid state at room temperature. It possesses a boiling point of 61°C. In the past, chloroform had been utilized as an anaesthetic agent. However, due to the significant risks associated with high doses, including the potential for fatality, chloroform is no longer employed as an anaesthetic in current medical practices. The chemical structure of acetone can be observed in Figure 21 [64], [65].

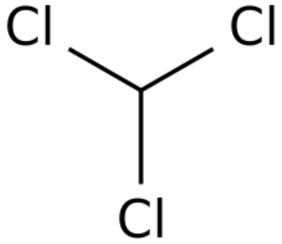

Figure 21: Chemical structure chloroform [65]

2.4.3 Ethanol

Ethanol (Figure 22) is an alcohol compound characterized by its colourless appearance. It is commonly encountered in alcoholic beverages. Ethanol exists as a liquid at room temperature, with a boiling point of 78°C. It is important to note that both the gaseous and liquid forms of ethanol are flammable.

PVDF exhibits solubility in ethanol, although its dissolution is not as effective as in acetone. While PVDF can partially dissolve in ethanol, acetone is generally preferred for achieving better solubility [66], [67].

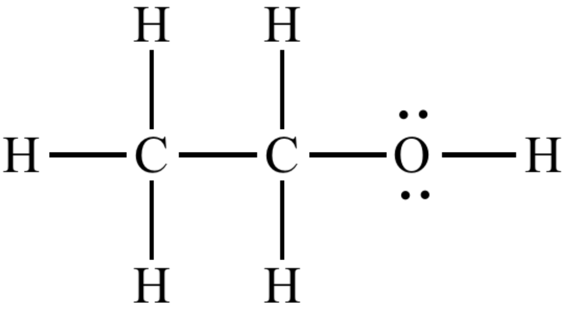

Figure 22: Chemical structure ethanol [68]

Acetone is the preferred solvent for dissolving PVDF due to its superior solubility properties. Although acetone emits harmful fumes, it is crucial to ensure complete and homogeneous dissolution of PVDF in the solvent. This selection is made considering the optimal compatibility and effectiveness of acetone as a solvent for PVDF, outweighing the associated risks associated with its fumes. Careful handling and appropriate safety measures should be implemented to mitigate any potential hazards during the dissolution process.

2.5 Substrates

The quality of a coating is influenced by the nature of the substrate it is applied to, which is determined by the surface tension of each material. Specifically, uniform films are readily formed on surfaces composed of glass and silicon dioxide (Figure 23 a,b). In contrast, the coatings applied to substrates such as SU-8 and HF-etched hydrophobic silicon tend to exhibit non-uniformity (Figure 23 c,d) [20].

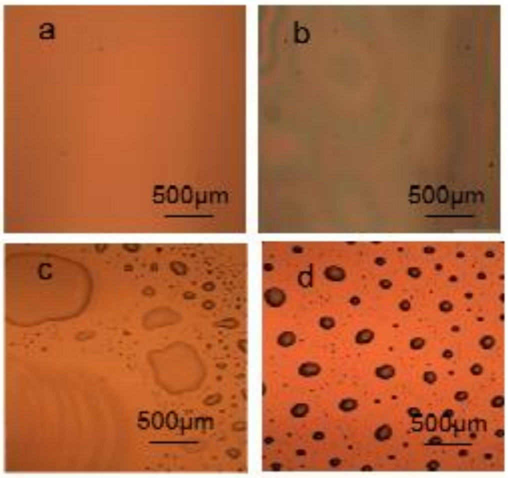

Figure 23: PVP on different substrates (a) glass (b) Silicon dioxide (c) SU-8 (d) HF etched silicon [20, p. 20]

The uniform coverage of the glass surface is readily apparent (Figure 18 a), highlighting one of the notable advantages of utilizing glass substrates. Additionally, glass substrates offer the convenience of facile analysis using optical microscopes, while their inherent surface roughness remains negligible, further enhancing their suitability for examination and characterization purposes.

2.6 Hydrophobicity

Hydrophobicity refers to the inherent property of a substance to resist or repel water. The extent of hydrophobicity is typically quantified by the contact angle that the substance makes with water (Table 1).

Table 1: Classification of hydrophobicity

Hydrophobicity	CA (°)
Min.	0°
Superhydrophilic	< 5°
Hydrophilic	< 90°
Hydrophobic	> 90°
Superhydrophobic	> 150°
Max.	180°

The magnitude of the contact angle and, consequently, the degree of hydrophobicity are contingent on two primary factors, namely, surface energy and surface roughness [69]–[71].

2.6.1 Surface energy

Surface energy, also referred to as surface tension, is a measure of the tensile or contractive force expressed in units of N/m or J/m^2. This tension arises from the cohesive forces that prevail at the interface between two different phases, such as a liquid and a gas.

Within a liquid, the water molecules located in the centre are completely surrounded by other water molecules, resulting in a balance of cohesive forces in all directions, and a net force of zero. As a result, the water droplet assumes a low-energy state, which is favourable. However, at the edge of the liquid, the water molecules experience an unbalanced cohesive force, resulting in a net force directed towards the centre. This leads to an increased energetic state of the water droplets at the edge.

The cohesive force is also the reason why water assumes a spherical shape in the absence of gravity, as the droplet attempts to minimize its surface area and reduce its surface energy.

Surface tension is an inherent property of every surface, which arises from the interface between two different phases, such as a liquid, solid, or gas. In this context, a surface can be defined as the boundary or interphase between two different phases [72].

When the forces acting on the interface between two phases (Figure 24) are expressed in terms of the X-direction, it results in the well-known Young's relation, given by $\gamma_{LG} \cos \theta = \gamma_{SG} - \gamma_{SL}$. This relation demonstrates that the contact angle formed by a droplet on a surface is dependent on all three surface energies [72].

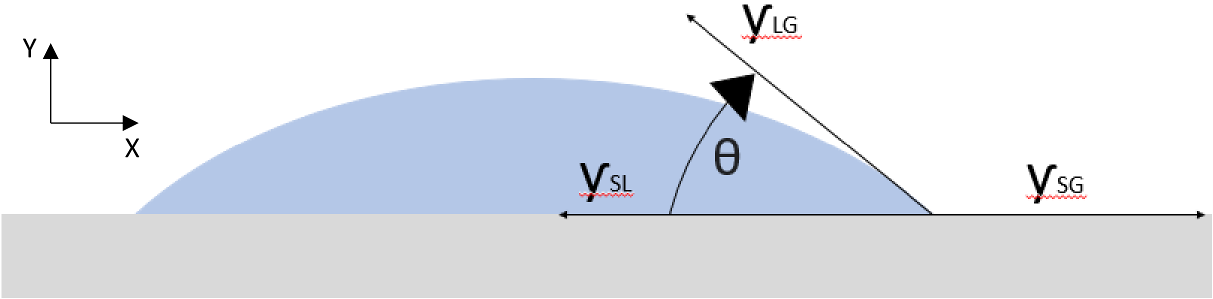

Figure 24: Water droplet on a hydrophilic substrate

2.6.2 Surface roughness

When a droplet of water lands on a rough surface, there are typically two ways in which it can make contact. As a result of this interaction, the contact angle of the droplet on the rough surface, denoted as θ*, may differ from that on a flat surface, denoted as θ.

In the Wenzel model (Figure 25), the droplet of water makes intimate contact with the rough surface, with no air pockets present between the droplet and the surface.

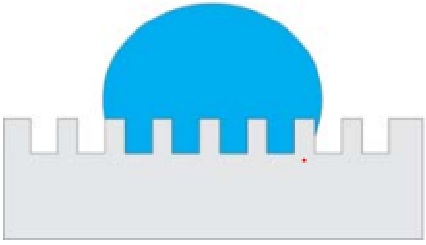

Figure 25: Wenzel model [69, p. 1351]

The degree of surface roughness is quantified by the roughness factor, R, which is defined as the ratio of the actual surface area of the solid to its projected surface area. Since no surface is perfectly smooth at the molecular level, R is always greater than one.

$$\cos \theta^* = R \cos \theta \tag{3}$$

Due to the roughness factor R being greater than one, the contact angle formed by a droplet on a rough surface will be lower than that on a flat surface for contact angles below 90°. Conversely, for contact angles above 90°, the contact angle will increase with increasing surface roughness [73], [74].

In the Cassie-Baxter model (Figure 26), air pockets are present between the droplet of water and the rough surface.

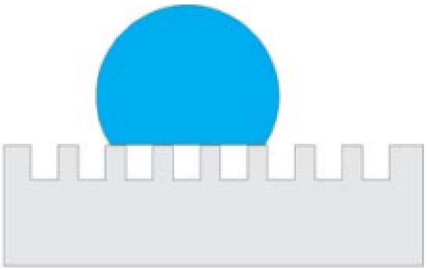

Figure 26: Cassie-Baxter model [69, p. 1351]

These pockets prevent full contact and result in a reduced effective contact area. The degree of contact between the droplet and the rough surface is quantified by the parameter frac, which represents the fraction of the droplet's surface area that is in contact with the solid surface.

$$\cos \theta^* = \mathrm{frac}\,(1 + \cos \theta) - 1 \tag{4}$$

As the fraction of contact area frac approaches zero, indicating that the droplet is primarily in contact with air pockets rather than the solid surface, the contact angle approaches 180°. The Cassie-Baxter model is particularly suitable for describing water-repellent and self-cleaning surfaces, where the presence of air pockets prevents the formation of a continuous liquid film and allows for easy removal of contaminants from the surface [73], [75].

2.8 Effects

2.8.1 Contact line pinning

When a droplet falls on a horizontal solid substrate it will stay in its position and cover a certain area on the substrate. If the temperature is high enough the droplet starts evaporating. While it is evaporating the covered surface area will stay the same, until its fully evaporated (Figure 27). The outer edge of the droplet remains stationary, while the height/volume ratio will decrease during the evaporation [81].

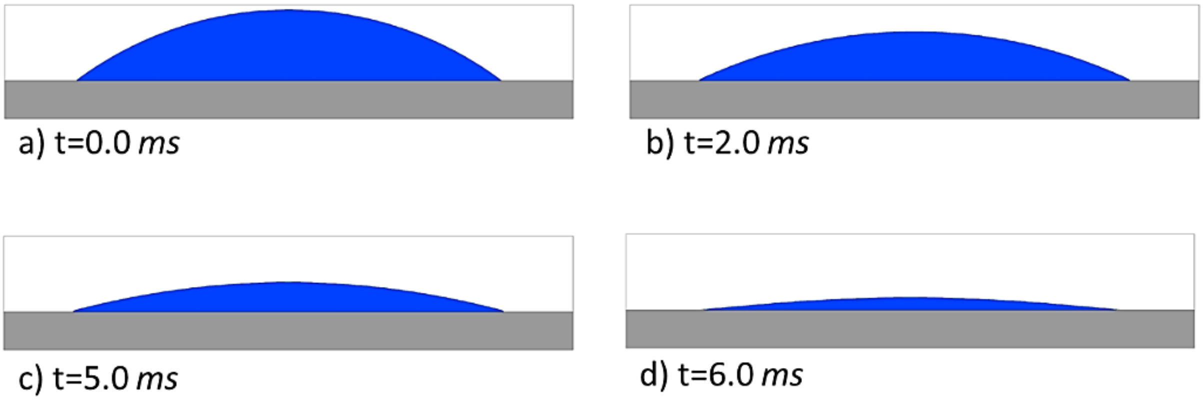

a) t=0.0 *ms*
b) t=2.0 *ms*
c) t=5.0 *ms*
d) t=6.0 *ms*

Figure 27: Contact line pinning [81]

The evaporation is fastest on the edge of the drop. The reason for this is that the angle on the edge is higher than the centre. Because the surface area must stay the same, a flow from the centre of the drop will be transported to the outer edges. If the droplet contains solid particles (ink, coffee,…), a solid ring will be left behind after evaporation due this transport. This is the reason in our everyday life that coffee stains are darker on the edge [81], [82].

2.8.2 Aggregation of nanoparticles

When two nanoparticles collide, they may either attract or repel each other. The primary attractive force is the Van der Waals force, which relies on the size of the particles and the distance between them. The repulsive forces originate from the electrical double layer surrounding the particles, which can overlap and result in repulsion when the particles come too close to each other. The zeta potential, which represents the charge at the shear plane rather than on the particle surface, provides an estimation of the electrical potential and its charge. The DLVO theory combines these forces to predict the overall force between particles, and the energy barrier heights determine whether the collision energy can exceed it and promote aggregation [47], [83].

2.9 Analysis equipment

2.9.1 Contact angle measurement system

To determine the hydrophobicity of a surface, a contact angle measurement system was essential. Specifically, the OCA 15plus system from Data Physics (USA) was utilized for the analyses in this study (Figure 28). This system is composed of several components, including a dosing device that is capable of precisely dispensing volumes from a Hamilton syringe. The Hamilton syringe has a maximum volume of 500µl and is equipped with a 0.25-mm inner diameter exchangeable needle. The substrate upon which the droplet is placed for contact angle measurement is supported by a movable sample table. This sample table can be manually adjusted in the xyz direction using turning screws as required. Positioned behind the sample table is an LED that emits monochromatic light, and the intensity of this light source can also be adjusted with a manual turning screw. The video camera (uEye) is situated in front of the sample table and is fitted with a lens that permits manual control of the zoom (0.7-4) and sharpness. All of these components are supported by an aluminium frame, which can be levelled using adjustable support feet. The software essential for measuring contact angles is SCA 20, which enables the user to control the dosing volume, make video recordings, or calculate the contact angle (CA) on live images using a connected computer [84]–[88].

Figure 28: OCA 15 system from DataPhysics (USA) [84]

2.9.2 Sliding angle measurement system

The surface's sliding angle is determined using a fully-automated contact angle measuring system (Figure 29). This system incorporates a contact angle measurement apparatus integrated with a lathe. The lathe enables precise adjustment of the system to a desired angle, while maintaining a continuously variable speed. As the lathe rotates, the camera also rotates synchronously, facilitating contact angle measurements during the analysis process [89], [90].

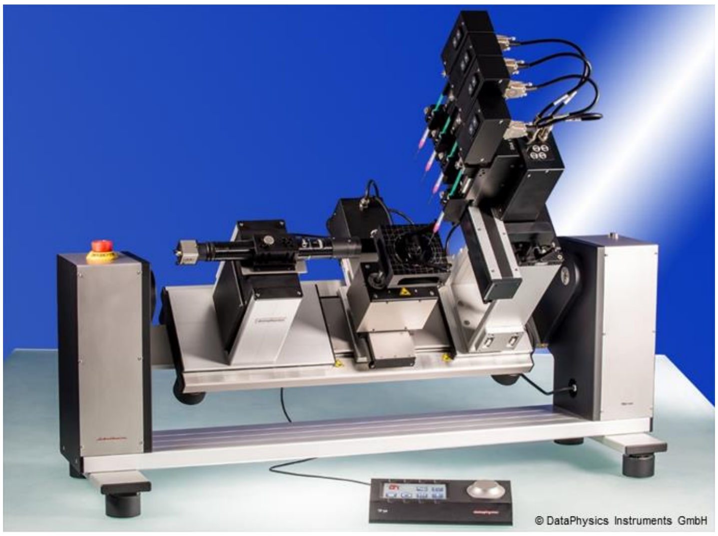

© DataPhysics Instruments GmbH

Figure 29: OCA 100 from DataPhysics (Germany) [90]

2.9.3 Profilometer

To determine the roughness of a surface, there is a need for a profilometer. There are two models of profilometers contact and optical. In optical, the profile is measured with reflections of different types of light. The profile analysis of this study was performed via the contact method with a Dektak XT (USA) equipped with a 2µm tip (Figure 31). In this process, a stylus moves across the surface of the sample. When the height of the stylus changes as it moves across the substrate, this will be recorded (Figure 30). Styluses look like an inverted cone with a sphere at the tip and are made of a wear resistant material such as diamond or sapphire. The precision of this device depends on the size of the stylus. A narrower stylus can better detect uneven surfaces. This device possesses a reproducibility of 4 Å (10^{-10} meter). The advantage of using a contact profilometer is that they are less sensitive to contamination from oils or dust compared to the optical profilometers. Beyond this,

this type is also cheaper. The disadvantage of this technique is that soft samples get scratched during analysis, especially if this has to be done several times. The stylus when used often will give different results compared to when it is new. The device's software visually displays the profile and can calculate the roughness based on this info. To prevent unwanted vibrations caused by, for example, passing traffic, the contact profilometer has been placed on a weighted table [91]–[94].

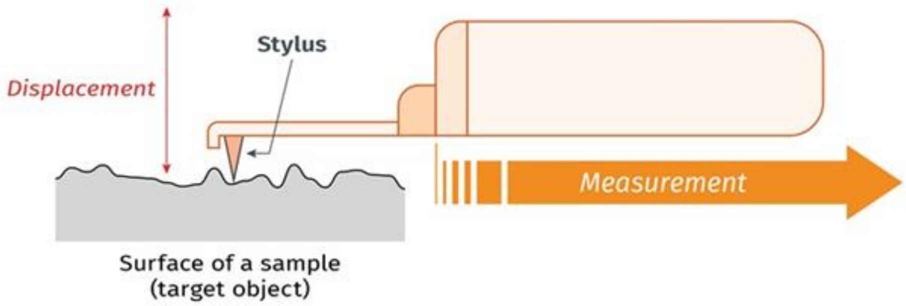

Figure 30: Working mechanism contact profilometer [93]

Figure 31: Dektak XT [91, p. 4]

2.9.4 Optical microscope

An optical microscope is utilized to magnify a sample so that it becomes more visible to the naked eye. A selection of lenses, each providing a specific magnification, can be chosen for this purpose. A controllable light source is mounted beneath the substrate to ensure adequate illumination of the sample. Coloured filters can be placed over this light source to produce the desired results. With appropriate software, the microscope can be equipped with a camera, enabling the capture of images that can be analysed on a computer with the correct scaling. In this study, an Axiovert 40 MAT microscope from Zeiss was utilized (Figure 32) [95], [96].

Figure 32: Axiovert 40 MAT (Zeiss) [97]

2.9.5 Scanning electron microscopy

Scanning electron microscopy (SEM) is a form of microscopy that uses electrons instead of visible light to obtain high-resolution images. The wavelength of light limits the resolution of the image, whereas electrons have a much smaller wavelength, which allows for a higher resolution. The electrons are directed onto the sample using an electron gun (Figure 33). Electromagnetic lenses ensure that the electron beam remains focused. When the sample is reached various types of electrons will be created. The most important electrons for SEM are the secondary and backscattered electrons. Secondary electrons provide surface information that can be used to create a three-dimensional image, whereas backscattered electrons produce a flat image. The contrast with backscattered images comes from differences in atomic number, with brighter spots indicating higher average atomic numbers. Many SEMs can produce both types of images because both are useful. The analysis takes place under vacuum to prevent the electrons from reacting with air particles, allowing only dry samples to be analysed with SEM [98]–[100].

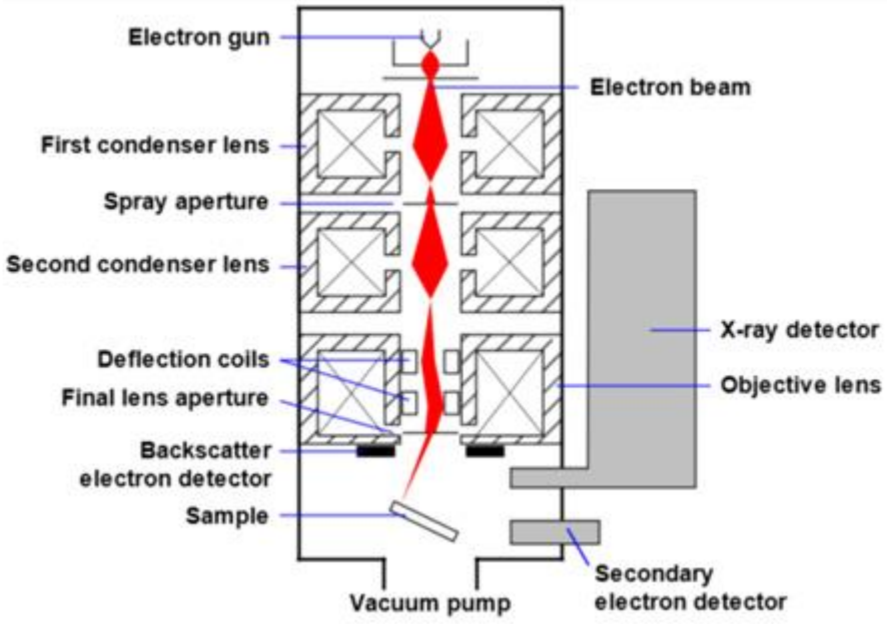

Figure 33: Schematic SEM [99]

3. Materials and methods

The substrate, microscope slides, are cleaned before coating by lying in a solution of respectively soap water (12.5 V% Branson Purpose Cleaner in demineralised water), demineralised water, acetone (Chemical Acetone AR., Fisher Chemical) and isopropanol (Extra Pure, SLR, Fisher Chemical) for 15 minutes each in an ultrasonic bath. After treatment with isopropanol, the slides are blown dry with nitrogen gas. The inks are self-assembled and homogeneously dissolved in acetone (Chemical Acetone, Fisher Chemical) as solvent. The chemicals used in the inks can contain polyvinylideenfluoride (Dyneon Fluoroplastic PVDF, 3M), 10-20 nm SiO_2 (99.5%, Non-Porous, SkySpringNanomaterials), 500 nm SiO_2 (99.0%, SkySpringNanomaterials); 10-20 nm SiO_2 made hydrophobic (99.8%, surface modified, Super-hydrophobic & Oleophilic, dispersible, SkySpringNanomaterials), 20-30 nm SiO_2 hydrolysis formed ([78], [79], Iran) and 300 nm SiO_2 hydrolysis formed ([78], [79], Iran). Before the inks are used, they spend 15 minutes in an ultrasonic bath to minimise the clustering of nanoparticles. The USSC used is an Exactacoat Ultrasonic Coating System from Sono-Tek (USA) with an Impact EDGE ultrasonic spraying nozzle. The ink is applied at a frequency of 120 kHz at a nozzle speed of 50 mm/sec. The generator provides a power of 4 W. The way of different stacking modes is shown in Figure 34. Hereby, it is worth noting that in the diagram, the blue colour corresponds to the PVDF component, while the red colour signifies the presence of nanoparticles.

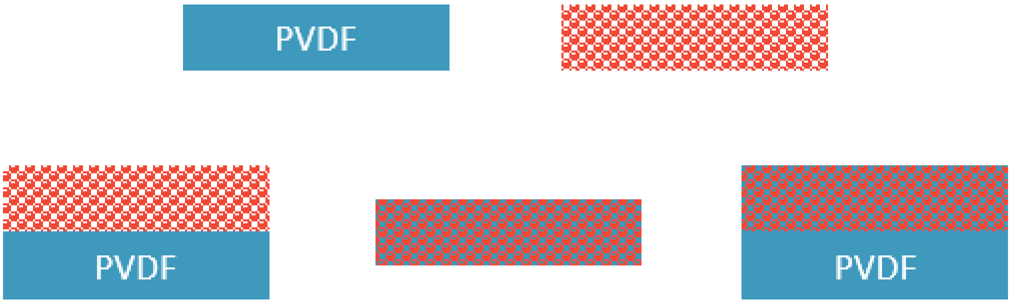

Figure 34: Different stacking layers

The different stacking modes are visually inspected by Zeiss Axiovert 40 MAT (Belgium). The hydrophobicity is measured with Data Physics OCA 15 (USA). The surface profile is measured by Bruker Dektak XT (USA). SEM images are taken by Zeiss GeminiSEM 450 (Belgium).

As part of the self-cleaning assessment, a controlled deposition of synthetic graphite powder (<20 µm, thermal scientific grade) is carried out using an air spray system. The procedure involves positioning multiple samples within a sealed enclosure, leaving one side open. The samples are evenly spaced from the opening. An appropriate quantity of graphite powder is applied to a surface positioned 10 cm above the base of the enclosure. By directing compressed air towards the powder, it is evenly distributed over the samples, ensuring a homogeneous coverage (Figure 35).

Figure 35: Uniform deposition of graphite

The purging process of the graphite-layered surface is efficiently executed by employing the USSC technique with the implementation of an AccuMist nozzle. In this process, the soiled surface is strategically positioned at a precise angle of 10° using a meticulously designed and fabricated 3D-printed object (Figure 36). To carry out the purging effectively, demineralized water is utilized as the purging agent. The nozzle performs a single sweeping motion at a controlled speed of 1 mm/sec, maintaining a consistent height of 1 cm above the raised surface. The flowrate during this purging operation is set at 5.00 ml/min. It is noteworthy that in this purging procedure, neither the shroud gas nor the hotplate is activated, as they are not required for the specific purging stage.

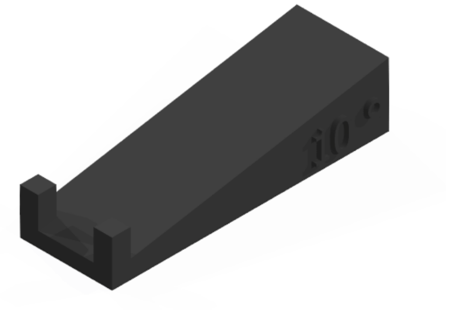

Figure 36: 3D printed 10° angle

To highlight the disparity in surface purity, photographic documentation will be conducted both before and after the purification process. This will be achieved by utilizing the image processing software known as ImageJ. The initial image will serve as a baseline reference, capturing the surface in its initial state. Following the purification procedure, a subsequent image will be taken to showcase the discernible improvements in cleanliness. The implementation of ImageJ software greatly facilitates the analysis and quantification of discrepancies in surface purity between the two images, thereby enabling a comprehensive evaluation of purification efficiency. This analysis entails converting the image to an 8-bit format and subsequently transforming it into a binary representation. The region of interest is then designated, and the particles are meticulously scrutinized using the predefined parameters outlined in Figure 37.

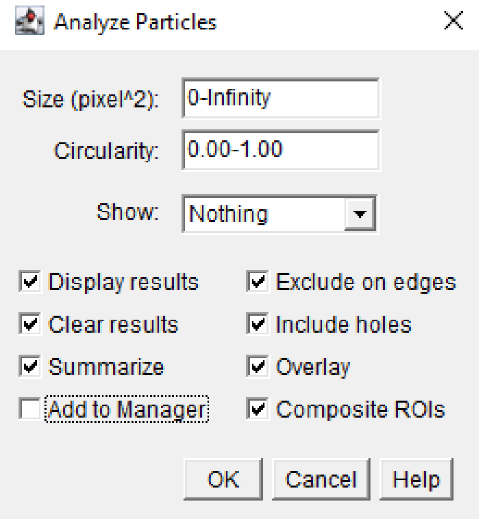

Size (pixel^2): 0-Infinity
Circularity: 0.00-1.00
Show: Nothing
☑ Display results
☑ Clear results
☑ Summarize
☐ Add to Manager
☑ Exclude on edges
☑ Include holes
☑ Overlay
☑ Composite ROIs

Figure 37: Settings analysis particles

To assess the sliding angle, a precise 9µl droplet is carefully deposited onto the surface with the OCA 100 (Figure 38). Subsequently, the system is focused, and a video recording of the droplet's behaviour is initiated. The lathe is precisely configured to rotate at a controlled speed of 1° per second (Figure 39 - Figure 41). The recording ceases when the droplet is entirely displaced from the field of view. From this recorded footage, the specific frame capturing the onset of droplet movement is manually selected. The corresponding angle depicted in this frame serves as the sliding angle of the analysed surface.

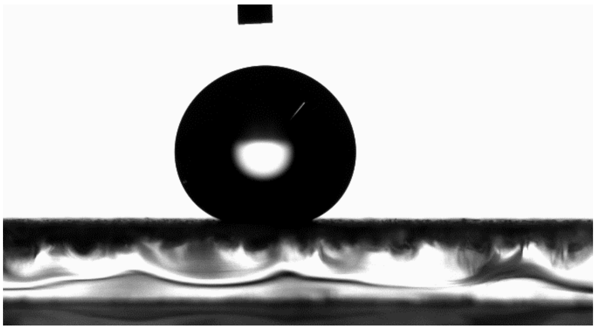

Figure 38: Initial 9µl droplet

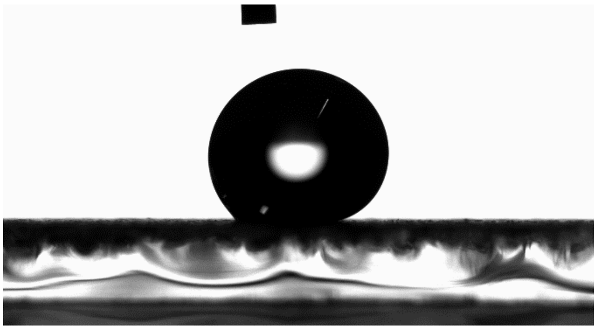

Figure 39: 9µl droplet before rolling

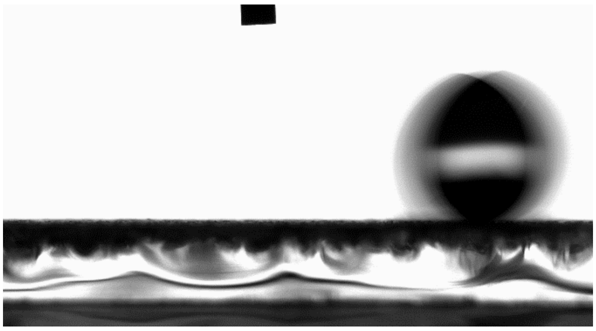

Figure 40: 9µl droplet rolling

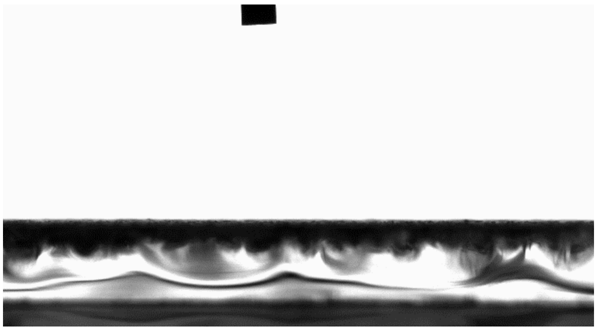

Figure 41: 9µl droplet after rolling

4. Results and discussion

4.1 Optimisation USSC

Optimisation of the USSC is performed with 2.5 wt% PVDF. This involves looking at the influence of height, pressure shroud gas, flowrate and subsequently temperature hotplate. The number of layers is adjusted according to the flowrate so that the quantity of chemicals deposited remains the same. The parameters are varied as shown in Table 2. These parameters will be observed by the optical microscope and the profilometer (Figure 42 - Figure 125). Here Ra represents the average roughness, Wa average waviness and Rt the vertical distance between the largest peak and lowest valley.

While investigating roughness may not be directly relevant to the specific objectives of this study, it is important to consider its potential impact on the final application of the research, particularly in relation to 3D printed materials. Therefore, it would be prudent to take roughness into account from the outset to ensure that the final product meets the necessary requirements for its intended use.

Table 2: Parameters of global optimisation

Height (cm)	Flowrate (ml/min)	Layers	Pressure shroud (psi)
3.5	0.50	80	2.0
4.5	0.50	80	2.0
5.5	0.50	80	2.0
6.5	0.50	80	2.0
7.5	0.50	80	2.0
8.5	0.50	80	2.0
6.5	0.50	80	0.5
6.5	0.50	80	1.0
6.5	0.50	80	1.5
6.5	0.50	80	2.0
6.5	0.50	80	2.5
6.5	0.50	80	3.0
6.5	0.50	80	3.5
6.5	0.10	400	2.0
6.5	0.25	160	2.0
6.5	0.50	80	2.0
6.5	1.00	40	2.0
6.5	1.50	26	2.0
6.5	2.00	20	2.0
6.5	2.50	16	2.0

4.1.1 Distance nozzle-substrate

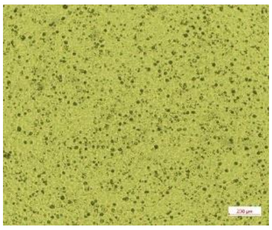
Figure 42: 3.5 cm (5x zoom)

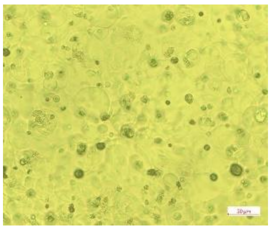
Figure 43: 3.5 cm (20x zoom)

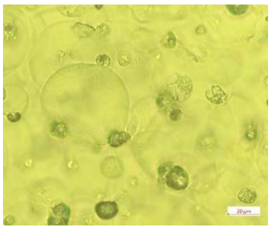
Figure 44: 3.5 cm (50x zoom)

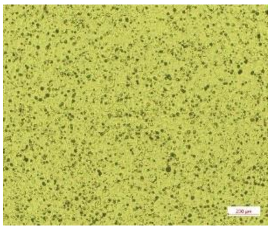
Figure 45: 4.5 cm (5x zoom)

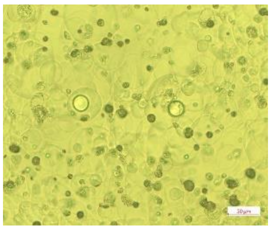
Figure 46: 4.5 cm (20x zoom)

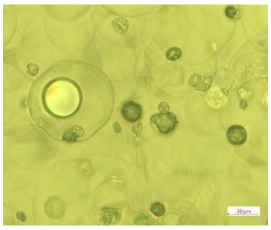
Figure 47: 4.5 cm (50x zoom)

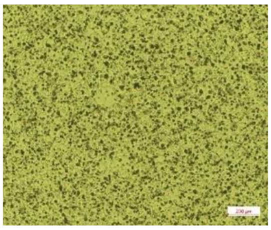
Figure 48: 5.5 cm (5x zoom)

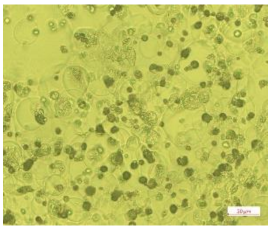
Figure 49: 5.5 cm (20x zoom)

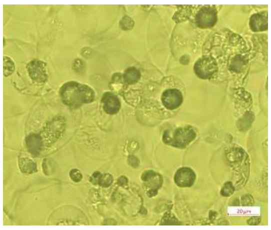
Figure 50: 5.5 cm (50x zoom)

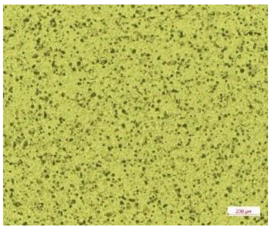
Figure 51: 6.5 cm (5x zoom)

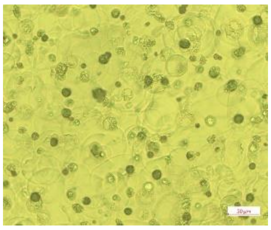
Figure 52: 6.5 cm (20x zoom)

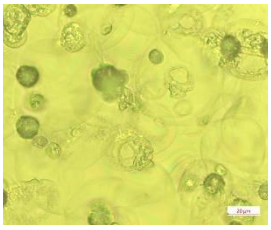
Figure 53: 6.5 cm (50x zoom)

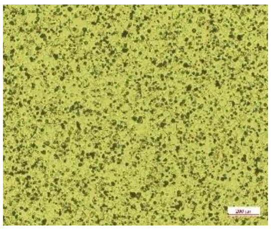
Figure 54: 7.5 cm (5x zoom)

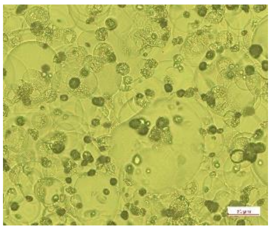
Figure 55: 7.5 cm (20x zoom)

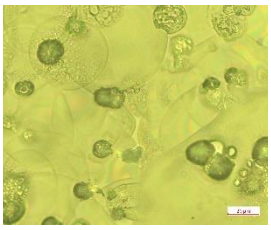
Figure 56: 7.5 cm (50x zoom)

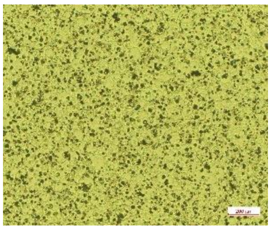
Figure 57: 8.5 cm (5x zoom)

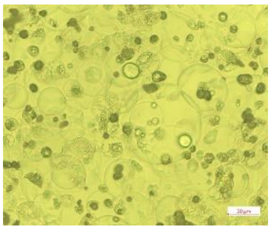
Figure 58: 8.5 cm (20x zoom)

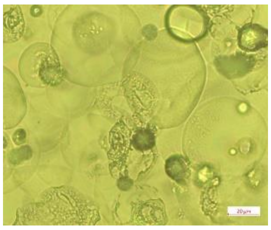
Figure 59: 8.5 cm (50x zoom)

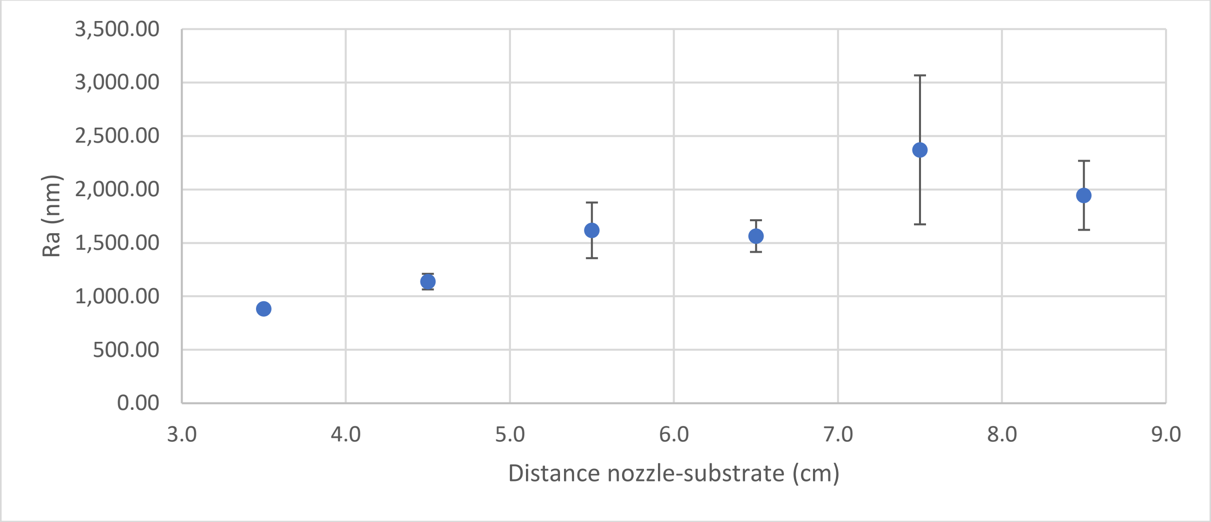

Figure 60: Ra value for different distances

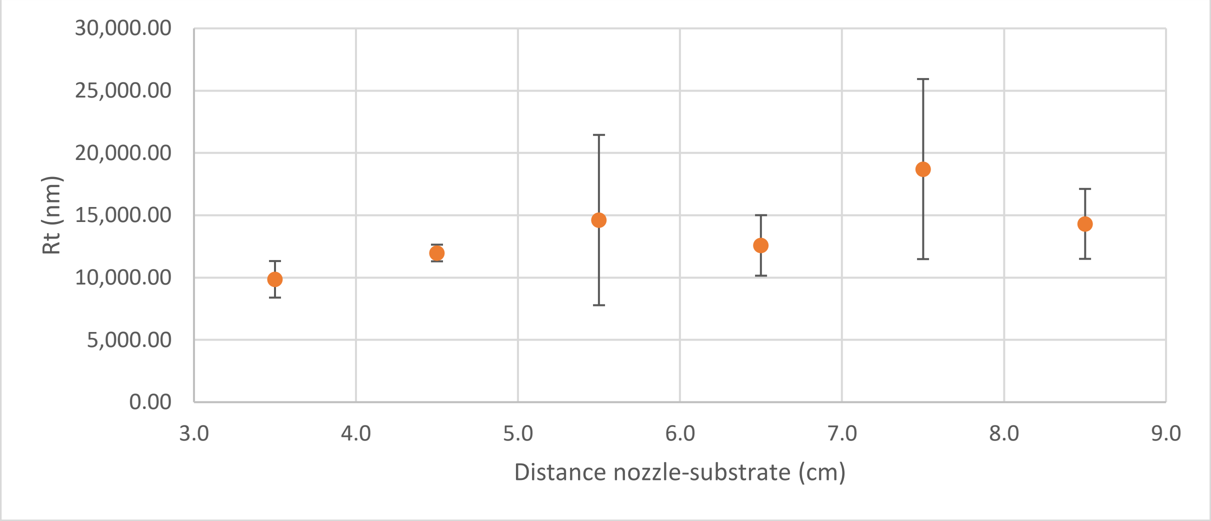

Figure 61: Rt value for different distances

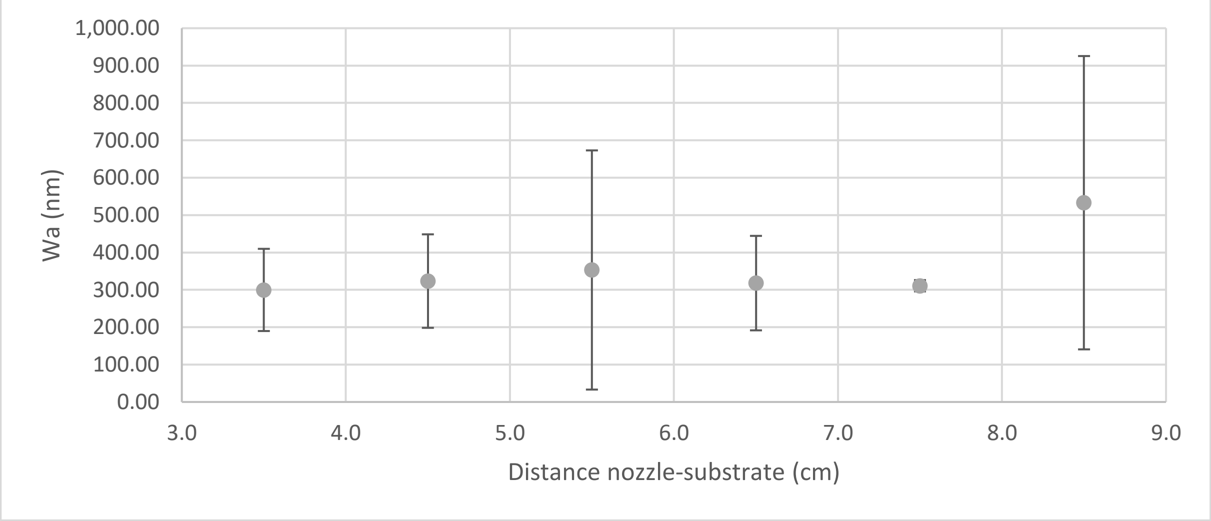

Figure 62: Wa value for different distances

Based on the graphical representations (Figure 60 - Figure 62), it can be observed that the minimum Ra and Rt values are achieved at a distance of 3.5 cm. In terms of the Wa value, there appears to be negligible variance across the different heights tested. It was practically not possible to spray at an even lower distance, because otherwise there would be contact between the movable nozzle and substrate. This also reduces the width of the surface being coated. Microscopic analysis (Figure 42 - Figure 59) revealed that weaker coffee rings were visible at lower distances due to the dissolving of previously deposited layers using acetone as a solvent, thereby enabling over-deposited droplets to merge with those already present on the surface. Based on the results of our tests, the ideal distance for applying 2.5 wt% PVDF was determined to be 3.5 cm. Dark spots observed in the images were attributed to PVDF and will be further investigated as part of this study to determine a solution for their removal.

4.1.2 Pressure shroud gas

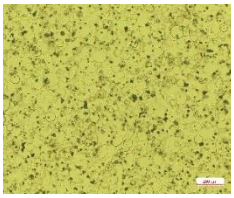
Figure 63: 0.5 psi (5x zoom)

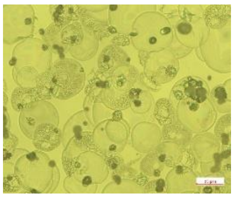
Figure 64: 0.5 psi (20x zoom)

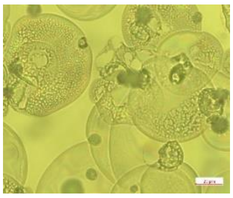
Figure 65: 0.5 psi (50x zoom)

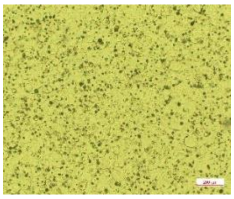
Figure 66: 1.0 psi (5x zoom)

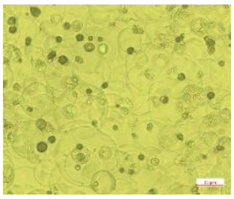
Figure 67: 1.0 psi (20x zoom)

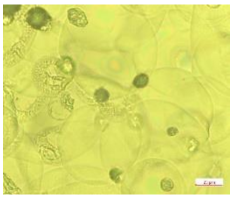
Figure 68: 1.0 psi (50x zoom)

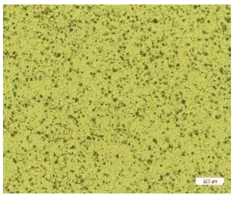
Figure 69: 1.5 psi (5x zoom)

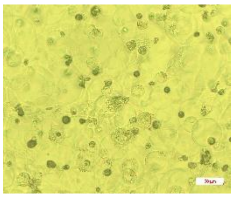
Figure 70: 1.5 psi (20x zoom)

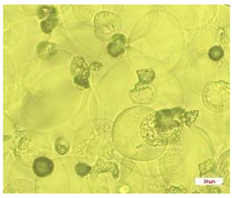
Figure 71: 1.5 psi (50x zoom)

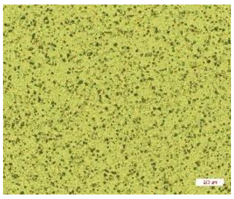
Figure 72: 2.0 psi (5x zoom)

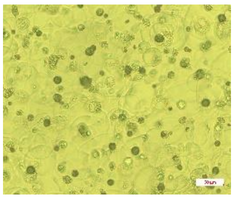
Figure 73: 2.0 psi (20x zoom)

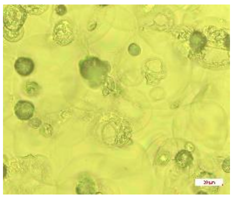
Figure 74: 2.0 psi (50x zoom)

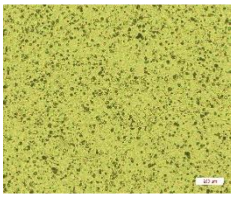
Figure 75: 2.5 psi (5x zoom)

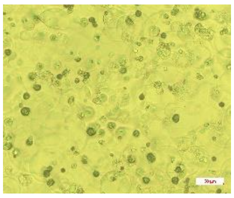
Figure 76: 2.5 psi (20x zoom)

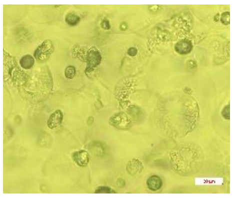
Figure 77: 2.5 psi (50x zoom)

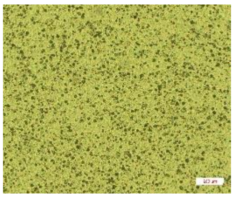
Figure 78: 3.0 psi (5x zoom)

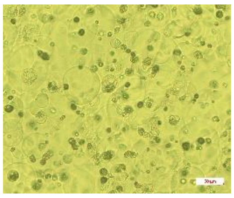
Figure 79: 3.0 psi (20x zoom)

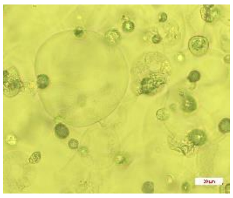
Figure 80: 3.0 psi (50x zoom)

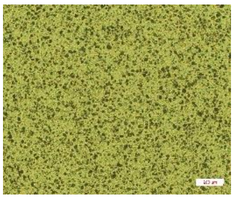
Figure 81: 3.5 psi (5x zoom)

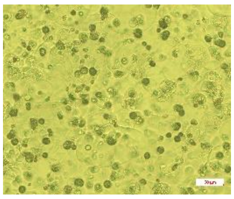
Figure 82: 3.5 psi (20x zoom)

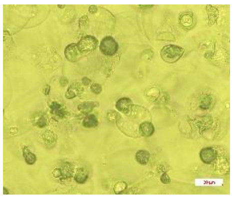
Figure 83: 3.5 psi (50x zoom)

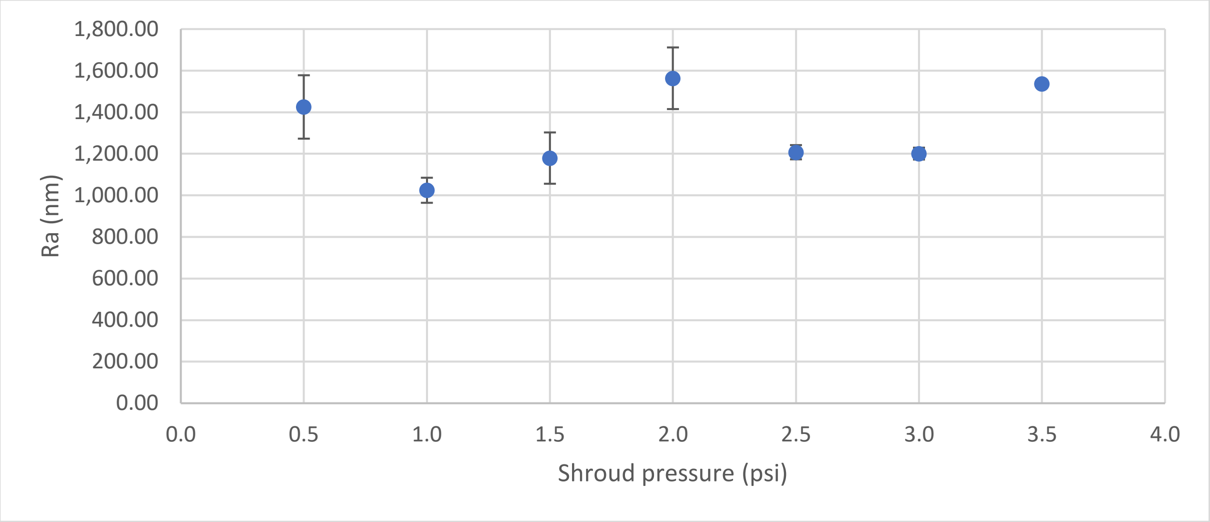

Figure 84: Ra value for different shroud pressures

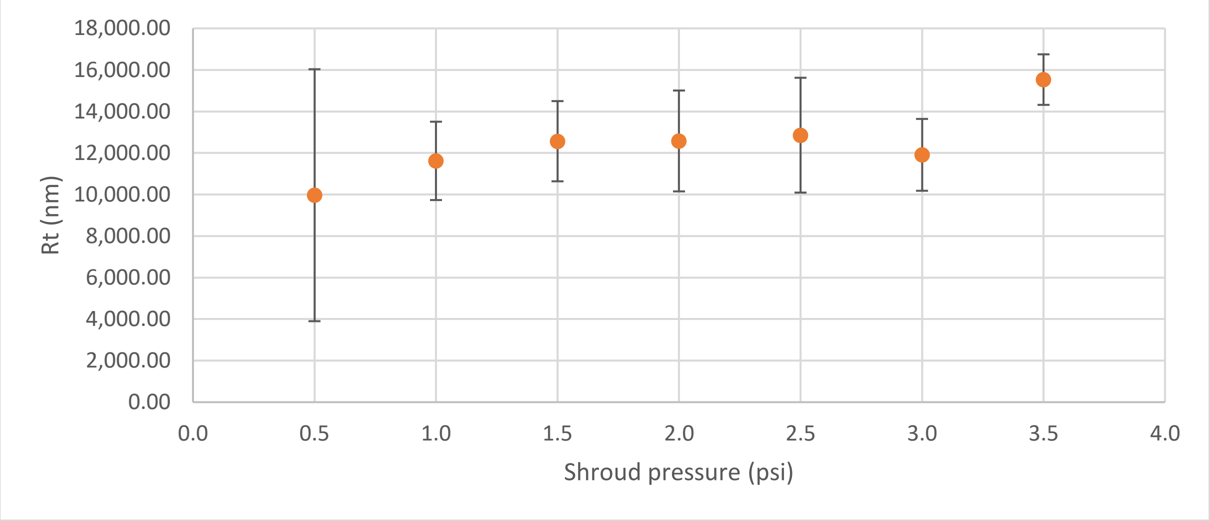

Figure 85: Rt value for different shroud pressures

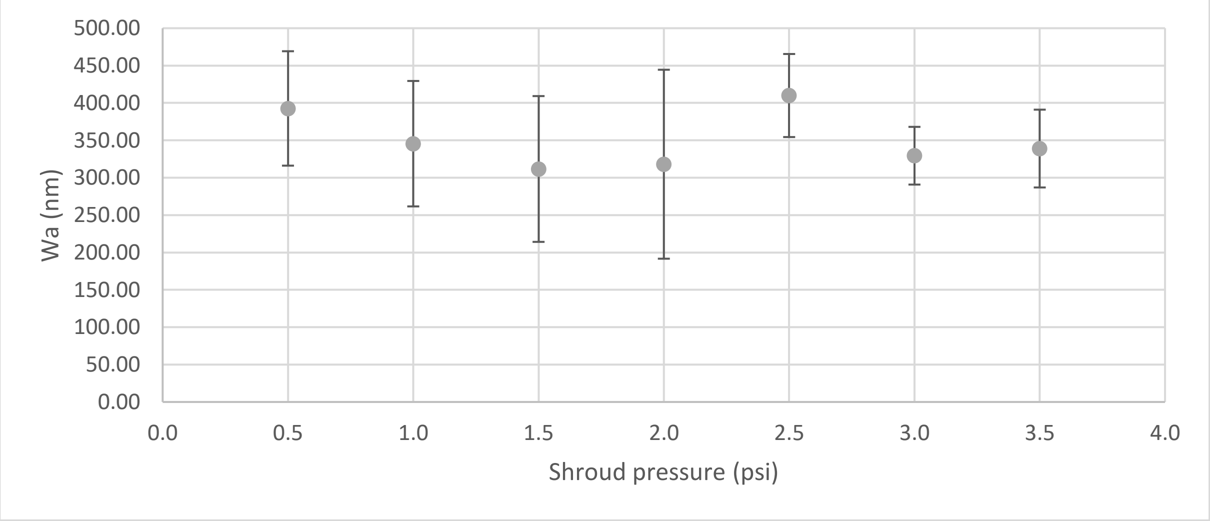

Figure 86: Wa value for different shroud pressures

The graphical data (Figure 84 - Figure 86) demonstrates that variations in shroud pressure have a comparatively minimal impact on the profile in contrast to alterations in the nozzle-substrate distance. The profile measurements (Figure 84 - Figure 86) do not indicate any definitive trends, rendering them insufficient for decision-making. In contrast, the optical microscope images reveal that coffee rings are more prominently visible at the extremities of the parameters tested (Figure 63 - Figure 83). Accordingly, it was determined that subsequent analyses would employ one of the middle parameters, specifically 2.0 psi.

4.1.3 Flowrate

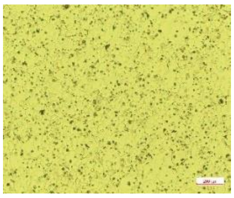
Figure 87: 0.10 ml/min (5x zoom)

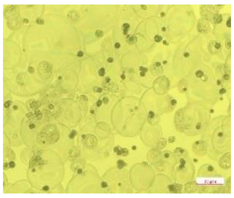
Figure 88: 0.10 ml/min (20x zoom)

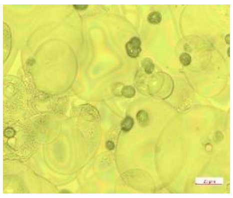
Figure 89: 0.10 ml/min (50x zoom)

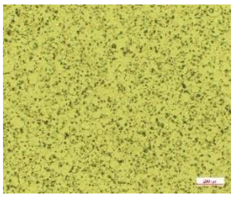
Figure 90: 0.25 ml/min (5x zoom)

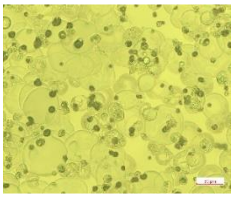
Figure 91: 0.25 ml/min (20x zoom)

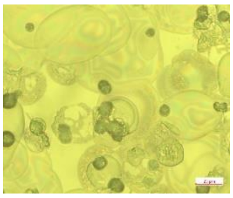
Figure 92: 0.25 ml/min (50x zoom)

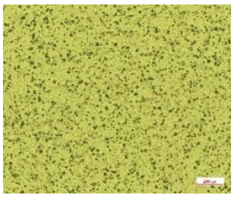
Figure 93: 0.50 ml/min (5x zoom)

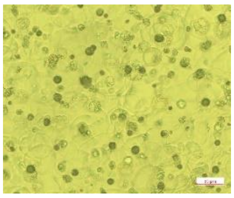
Figure 94: 0.50 ml/min (20x zoom)

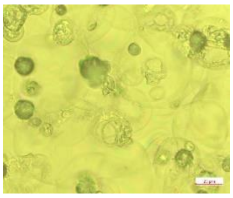
Figure 95: 0.50 ml/min (50x zoom)

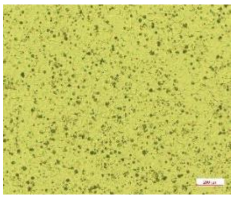
Figure 96: 1.00 ml/min (5x zoom)

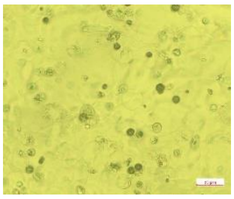
Figure 97: 1.00 ml/min (20x zoom)

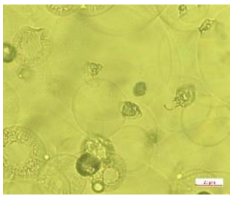
Figure 98: 1.00 ml/min (50x zoom)

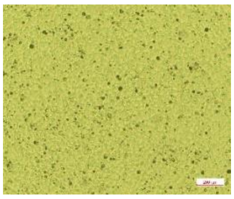
Figure 99: 1.50 ml/min (5x zoom)

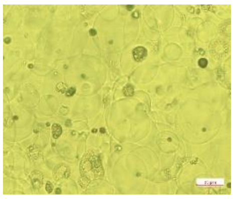
Figure 100: 1.50 ml/min (20x zoom)

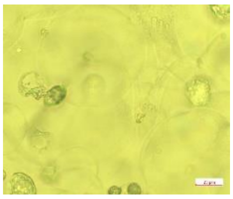
Figure 101: 1.50 ml/min (50x zoom)

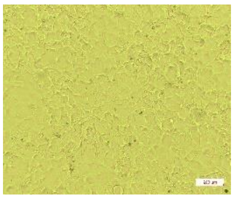
Figure 102: 2.00 ml/min (5x zoom)

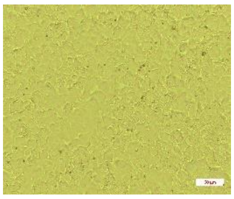
Figure 103: 2.00 ml/min (20x zoom)


Figure 104: 2.00 ml/min (50x zoom)

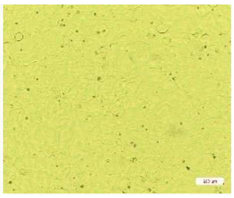
Figure 105: 2.50 ml/min (5x zoom)

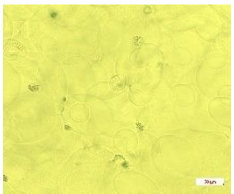
Figure 106: 2.50 ml/min (20x zoom)

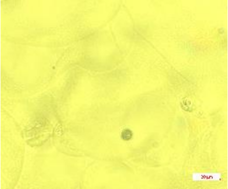
Figure 107: 2.50 ml/min (50x zoom)

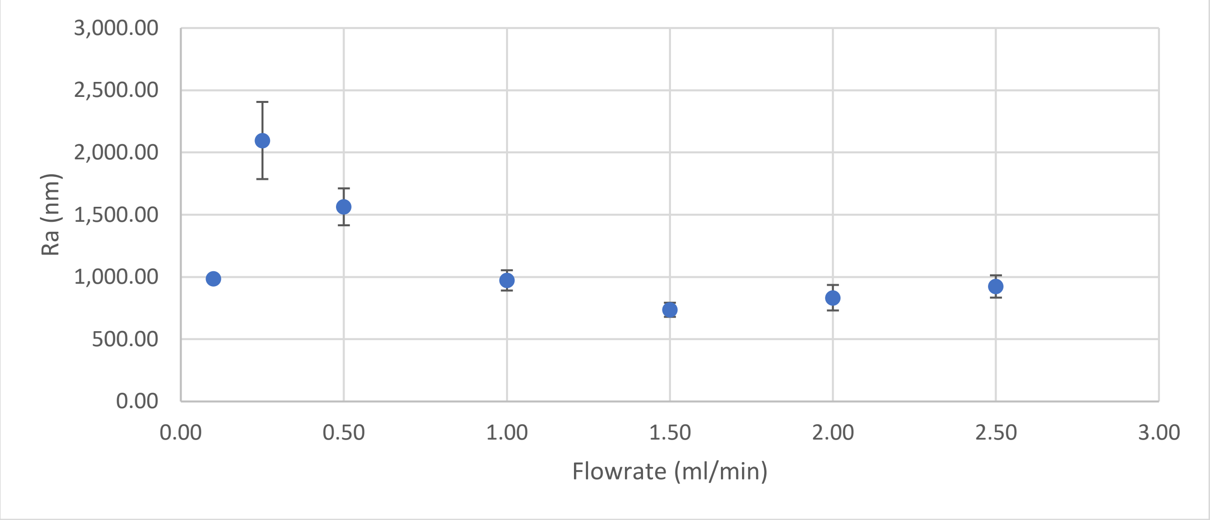

Figure 108: Ra value for different flowrates

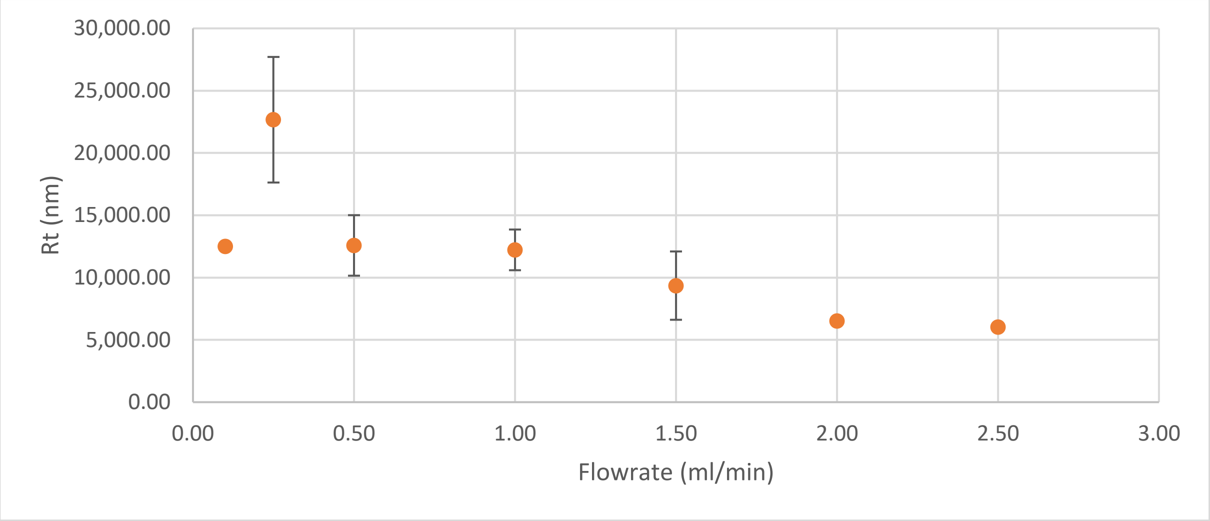

Figure 109: Rt value for different flowrates

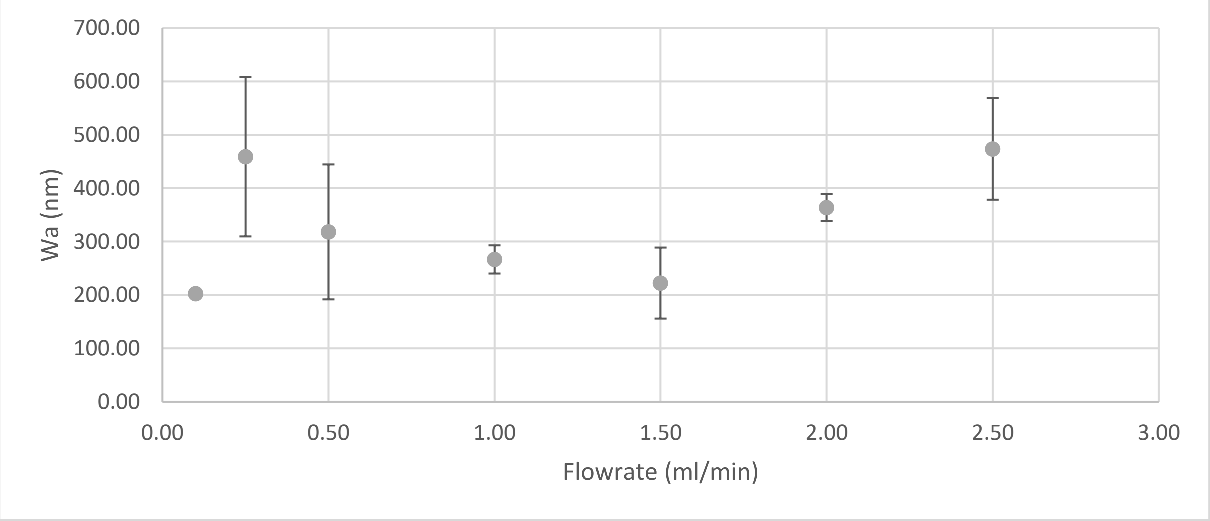

Figure 110: Wa value for different flowrates

At lower flowrates, the appearance of coffee rings is more pronounced compared to higher flowrates. Additionally, these lower flowrates require a longer duration for ink deposition onto the substrate.

Consequently, they can be excluded as viable options. Upon examining the graphs (Figure 108 - Figure 110), it is apparent that a flowrate of 1.50 ml/min yields the minimum values for both Ra and Wa, if disregarding the lower flowrates. Regarding the Rt value, due to the larger uncertainty at 1.50 ml/min, it too is situated near the minimum point. Therefore, a flowrate of 1.50 ml/min is deemed optimal.

4.1.4 Temperature hotplate

The final parameter under investigation is the temperature of the hotplate. In this regard, the profilometer is employed to measure the roughness of the surface at different settings of Table 3. The results are shown in Figure 111 - Figure 113.

Table 3: Optimisation of hotplate temperature

Hotplate temperature (°C)	Height (cm)	Flowrate (ml/min)	Layers	Pressure shroud (psi)
20	3.5	1.50	26	2.0
40	3.5	1.50	26	2.0
60	3.5	1.50	26	2.0
80	3.5	1.50	26	2.0
100	3.5	1.50	26	2.0

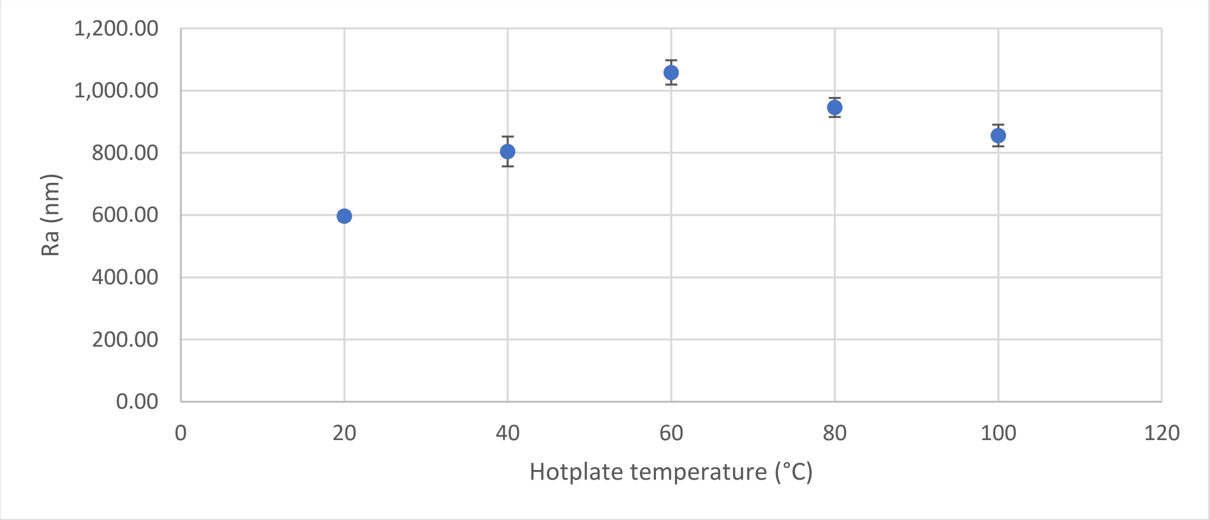

Figure 111: Ra value for different hotplate temperatures

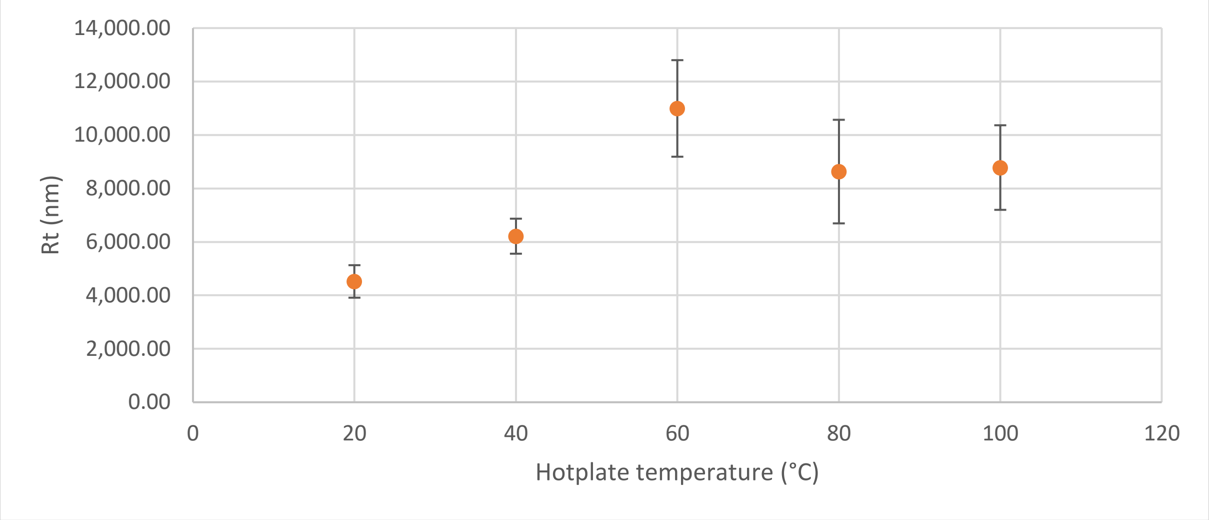

Figure 112: Rt value for different hotplate temperatures

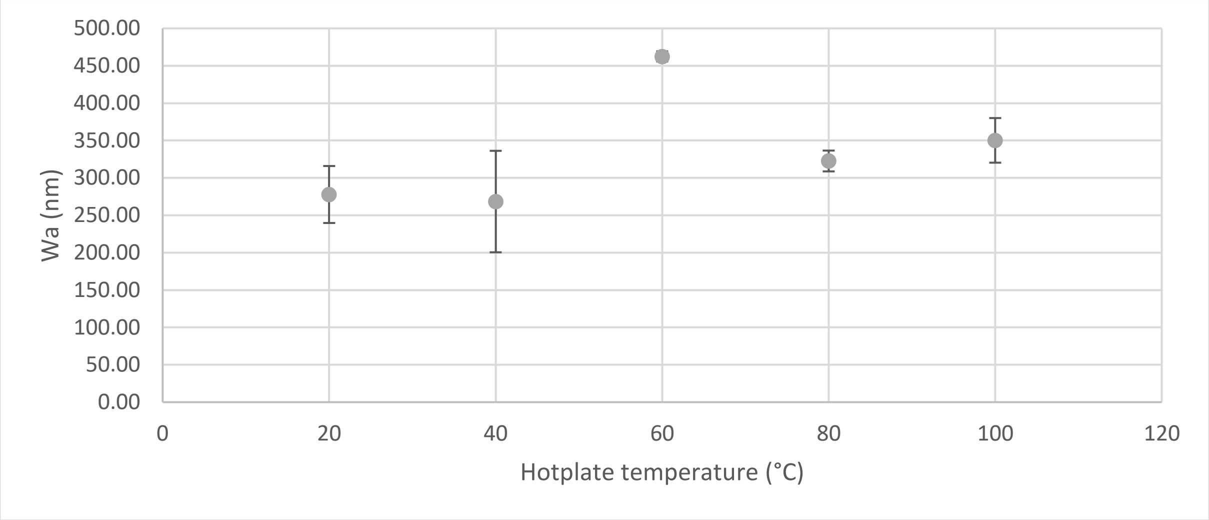

Figure 113: Wa value for different hotplate temperatures

In relation to the three measured parameters (Figure 111 - Figure 113), it was consistently observed that a peak occurred at 60°C. Interestingly, the lowest values were observed at lower temperatures. In order to ensure the solvent evaporation transpires at an optimal rate without necessitating excessively high temperatures, a decision was made to maintain a constant temperature of 40° throughout this research.

4.1.5 Removing dark spots

During the optimization of the USSC with 2.5 wt% PVDF, the presence of dark spots within the coating was revealed through optical microscopy. These spots will probably have an impact on the roughness of the surface. A systematic investigation was conducted by eliminating each parameter to identify the source of the dark spots, which were traced back to the PVDF material. Prior to conducting a comprehensive review of the relevant literature, several techniques were attempted to remove these granules, including pre-treatment with membrane filtration (Figure 118 & Figure 119), post-curing of deposited coatings (Figure 120 - Figure 125), and acetone post-spraying as a post-treatment (Figure 116 & Figure 117). The effectiveness of these techniques was compared with a control sample (Figure 114 & Figure 115).


Figure 114: Control sample (5x zoom)

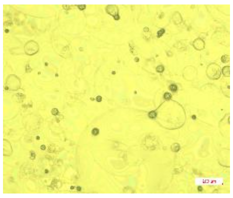
Figure 115: Control sample (20x zoom)

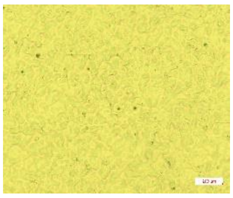
Figure 116: Post-spraying acetone (5x zoom)

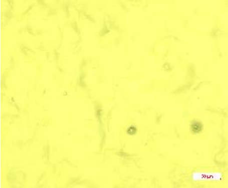
Figure 117: Post-spraying acetone (20x zoom)

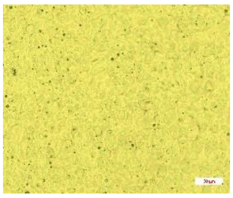
Figure 118: Filtered 450 nm (5x zoom)

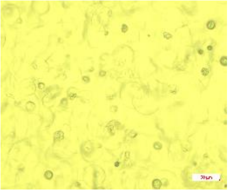
Figure 119: Filtered 450 nm (20x zoom)

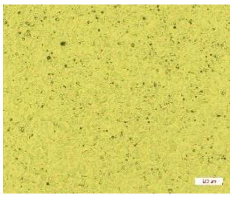
Figure 120: Curing 150°C 15' (5x zoom)

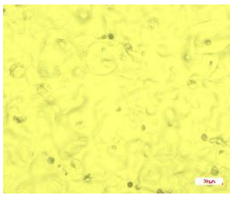
Figure 121: Curing 150°C 15' (20x zoom)

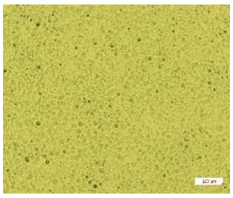
Figure 122: Curing 160°C 15' (5x zoom)

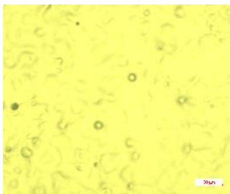
Figure 123: Curing 160°C 15' (20x zoom)

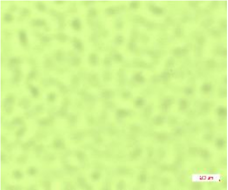
Figure 124: Curing 170°C 15' (5x zoom)


Figure 125: Curing 170°C 15' (20x zoom)

Although the image of the 170°C curing process could not be focused, the results from all tests suggest that post-spraying with acetone is the most effective technique. This post-treatment step promotes the uniform dissolution and spreading of PVDF granules across the surface. As such, it is recommended that this post-treatment step be included in future research to enhance the quality of the final coatings.

4.1.6 Optimal USSC parameters (2.5 wt% PVDF)

For the deposition of 2.5 wt% PVDF, it is recommended to use optimal settings that include a deposition height of 3.5 cm, a flowrate of 1.50 ml/min, a shroud pressure of 2.0 psi, and a hotplate temperature of 40°C (Table 4). These settings are the most effective for achieving the desired result.

Table 4: Optimal USSC parameters 2.5 wt% PVDF

Hotplate temperature (°C)	Height (cm)	Flowrate (ml/min)	Pressure shroud (psi)
40	3.5	0.50	2.0

4.2 Optimisation of hydrophobic properties

4.2.1 PVDF

Figure 126: PVDF stacking layer

To optimise the PVDF layer, the concentration of PVDF and the number of layers applied are varied.

First, the influence of the number of layers is examined with 2.5 wt% PVDF with the optimal parameters (Table 4). The results are shown in Figure 127 & Figure 128.

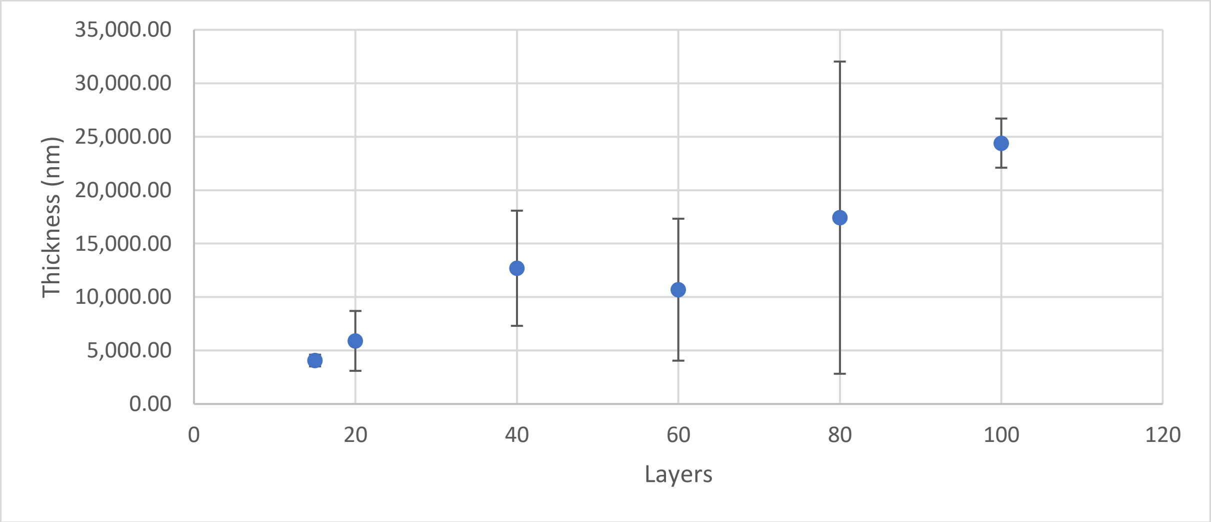

Figure 127: Thickness for different layers with 2.5 wt% PVDF

A linear correlation can be observed in the thickness measurements, whereby the thickness of the PVDF coating increases proportionally with the deposition of additional layers. This relationship became apparent after the deposition of 15 layers. The thickness measurements for 1, 5, and 10 layers are omitted from this presentation as these measurements are incomplete due to the incomplete coating of the entire surface, rendering them unreliable for analysis.

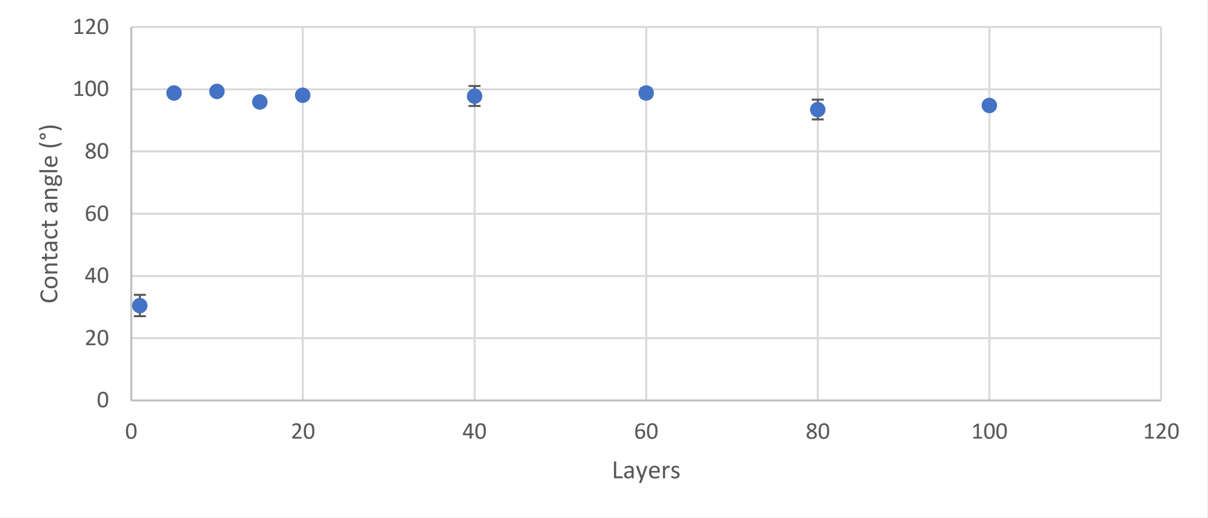

Figure 128: CA for different layers with 2.5 wt% PVDF

Upon spraying a single layer of 2.5 wt% PVDF, no significant increase in contact angle is observed. However, with the application of five layers, a contact angle of ±100° can be achieved (Figure 128). It can be inferred that the entire surface of the glass substrate is coated after five layers of PVDF, and further coating will not result in a higher contact angle. Adding more layers will simply result in the additional PVDF being laid on top of the previously applied layers, and thus will not contribute to an increase in contact angle.

Furthermore, the influence of PVDF concentration is investigated at 20 layers in Figure 129 & Figure 130.

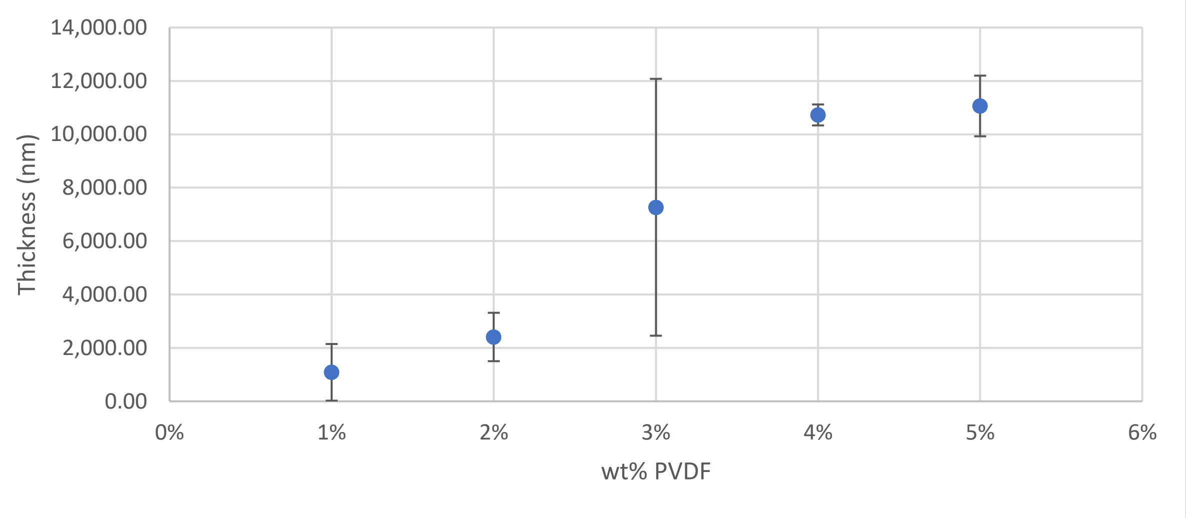

Figure 129: Thickness for different concentrations of 20 layers PVDF

A linear correlation can be observed in the thickness measurements, indicating that the thickness of the final PVDF coating increases in direct proportion to the concentration of PVDF deposited.

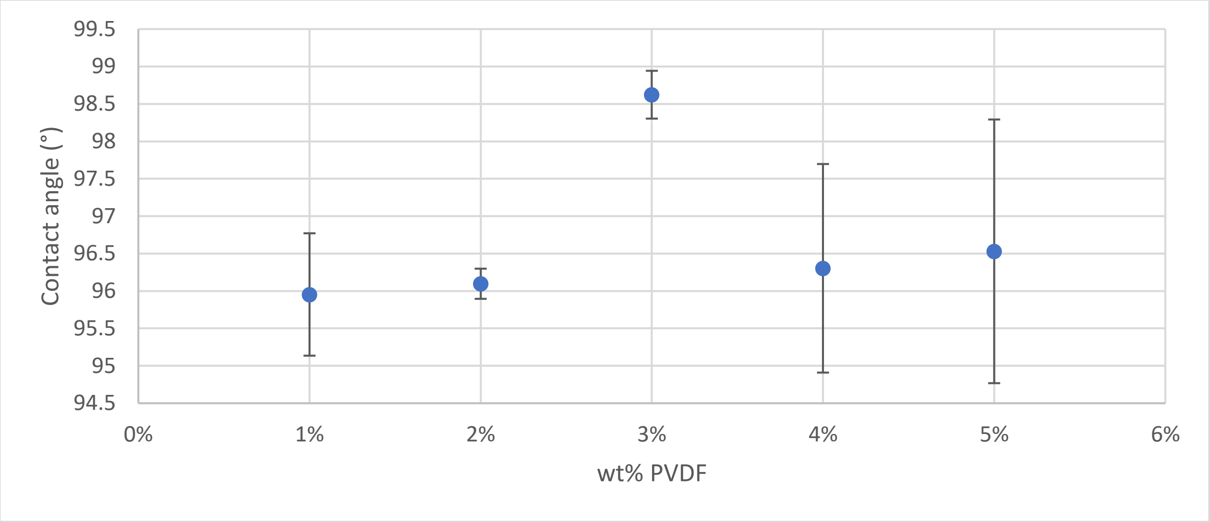

Figure 130: CA for different concentrations of 20 layers PVDF

According to the results depicted in Figure 130, there appears to be no significant impact of concentration on the contact angle. While a slight difference of 2° is observed at 3 wt%, this can be deemed negligible. Overall, contact angles approaching 100° are still achieved across the range of concentrations tested.

The optimum hydrophobicity that can be achieved with PVDF on a glass substrate is about 100°. This is achieved at a concentration of 2.5 wt% by depositing 10 layers.

4.2.2 SiO_2 nanoparticles

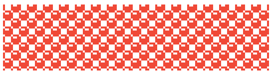

Figure 131: Nanoparticles stacking layer

During the deposition of nanoparticles using the same settings as PVDF, it is observed that only a limited area is coated with nanoparticles. This creates issues when measuring the contact angle, as the water droplet falls past this narrow area. To address this, the distance between the nozzle and substrate is adjusted until a uniform distribution for 10 - 20 nm SiO_2 made hydrophobic is achieved across the substrate (Table 5 & Figure 132). This ensures that contact angle measurements can be taken accurately and reliably.

Table 5: Distribution NP for different heights

Concentration (g/l)	Height (cm)	Flowrate (ml/min)	Layers	Shroud pressure (psi)	Uniform
1	3.5	1.50	20	2.0	No
1	4.5	1.50	20	2.0	No
1	5.5	1.50	20	2.0	No
1	6.5	1.50	20	2.0	Yes

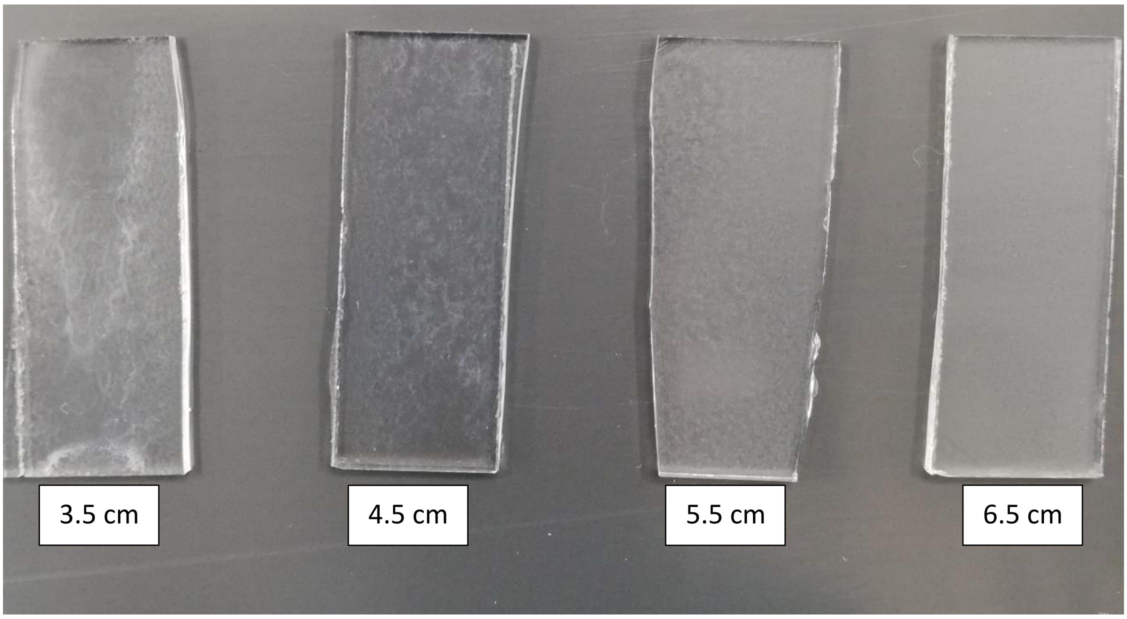

Figure 132: Visual distribution of NP on different heights

Based on the findings presented in Table 5 & Figure 132, it can be inferred that the nanoparticles are evenly distributed on the substrate when the nozzle is positioned at a distance of 6.5 cm from the substrate. As a result, the nanoparticles are excited at a distance of 6.5 cm.

During the contact angle measurement of the last sample from Table 5, it was discovered that the conventional approach could no longer be utilized.

In the conventional approach, a small volume of water is deposited using a syringe. During the deposition process, the water droplet adheres to the syringe tip. Subsequently, the substrate is lifted until contact is made with the droplet, at which point the droplet detaches from the needle tip and lands on the substrate. However, this method does not apply when working with a superhydrophobic substrate, as the substrate merely displaces the formed droplet without facilitating its release (Figure 133).

Figure 133: Traditional sessile drop technique

This necessitated the adoption of a new method for measuring the nanoparticles. Various approaches were attempted, but not all were successful. Reducing the inner diameter of the needle resulted in a capillary effect that caused water to continue dripping out of the needle, preventing the formation of a constant-volume droplet on the substrate. Another approach involved dispensing a larger volume of water to provide additional downward force due to gravity. However, this led to the deposition of a larger droplet on the surface. The influence of gravity causes the droplet to adopt an oval shape, leading to a reduced measured contact angle.

Subsequently, a methodology was devised to ensure the controlled deposition of a small volume of water (Figure 134). This approach drew inspiration from the droplet deposition technique employed by the USSC, which utilizes a gas. The modified procedure involved initiating the process with an empty syringe containing only air. Subsequently, the desired water volume was introduced for deposition. By orienting the syringe vertically, a significant volume of air was maintained above the water within the syringe. Upon depositing the droplet from the syringe, it adhered to the needle's tip. Further deposition compressed the residual air in the syringe, resulting in an increase in pressure. Eventually, the pressure reached a critical point, allowing the hanging droplet to be deposited onto the substrate at a low velocity. This ensured the precise deposition of the desired water volume that had been carefully absorbed beforehand.

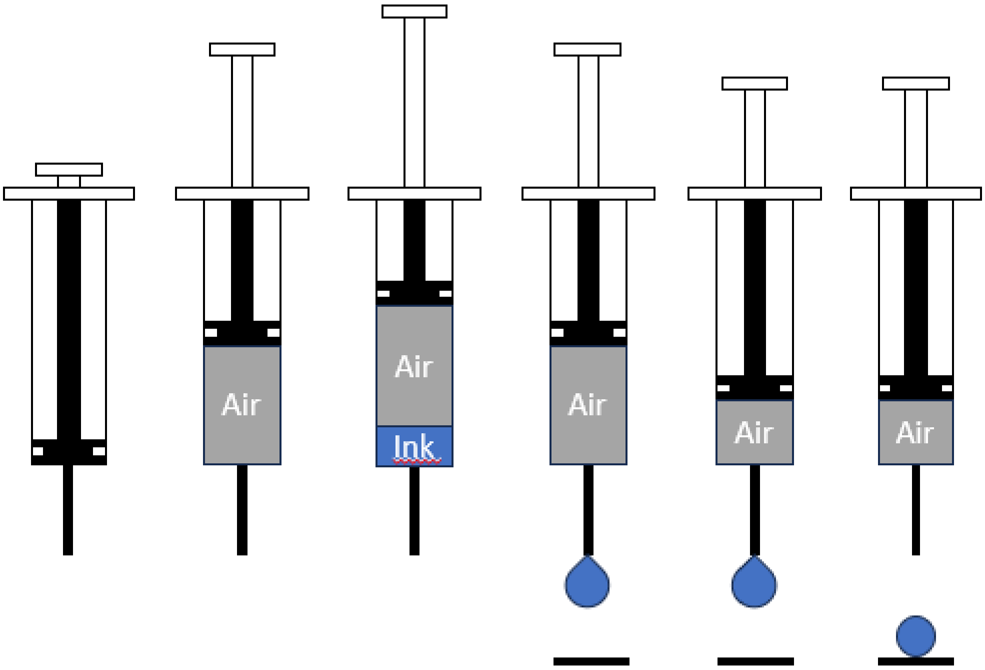

Figure 134: Used method for CA measurements

The influence of flowrate was explored with 1 g/l 10 - 20 nm SiO_2 made hydrophobic nanoparticles, the results are presented in Figure 135. To ensure that an equal amount of chemicals is deposited, the number of layers is adjusted with each application. The shroud pressure is 2.0 psi and the distance of 6.5 cm is maintained.

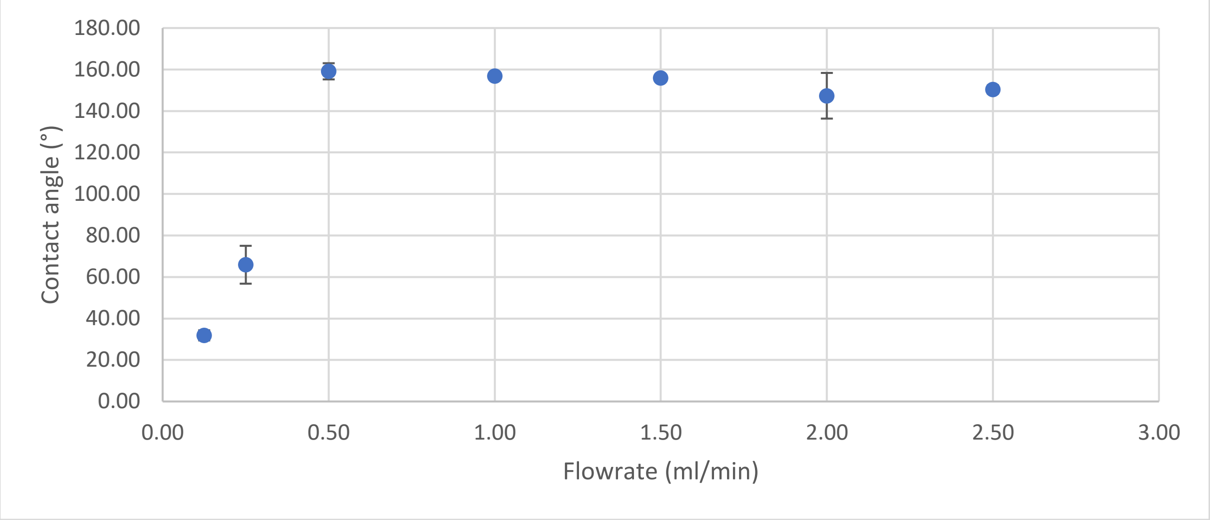

Figure 135: CA for different flowrates of 10 - 20 nm SiO_2 hydrophobic

Based on the data presented in (Figure 135), it can be observed that at low flowrates of 0.10 ml/min and 0.25 ml/min, the achieved contact angle is significantly lower compared to the contact angle at higher flowrates (above 0.50 ml/min). Notably, superhydrophobicity is achieved and maintained when working with the higher flowrates that were tested. To deposit these nanoparticles, a flowrate of at least 0.50 ml/min must be present to obtain the optimal contact angle.

The influence of nanoparticle concentration is checked with 10 - 20 nm SiO_2 made hydrophobic in Figure 136. The experiment was conducted at a flowrate of 1.00 ml/min to ensure optimal conditions, and 15 layers were deposited using a shroud pressure of 2.0 psi at a distance of 6.5 cm.

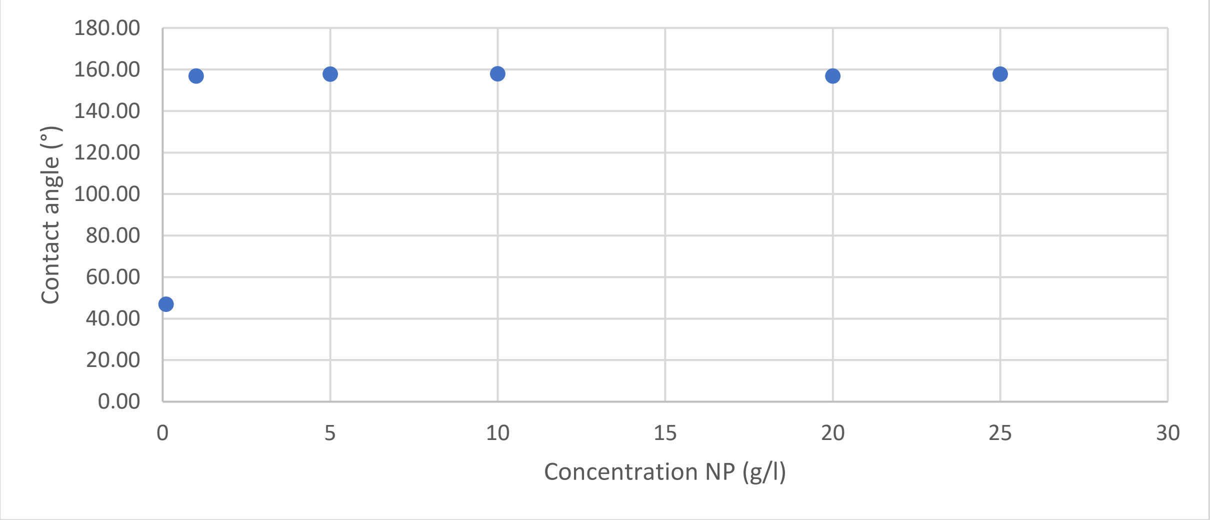

Figure 136: CA for different concentrations of 10 - 20 nm SiO_2 hydrophobic

At the lowest concentration of 0.1 g/l, minimal changes in contact angle were observed. However, increasing the concentration to 1 g/l resulted in a significant increase in the contact angle, reaching approximately 160°. Further increases in concentration had no significant impact on the contact angle (Figure 136). Therefore, to achieve the optimal contact angle, a minimum concentration of 1 g/l is recommended.

All nanoparticles were examined to assess the impact of the number of layers (Figure 137). This experiment was conducted at a concentration of 1 g/l with a shroud pressure of 2.0 psi. For non-hydrolysis particles, the flowrate was set at 1.50 ml/min, while for hydrolysis particles, it was set at 1.00 ml/min. The difference in flowrates is due to the separate days on which these analyses were performed. Notably, the difference in flowrate does not significantly impact the contact angle, as it has been previously established that a flowrate of at least 0.50 ml/min is necessary to achieve optimal results, and higher flowrates do not enhance the contact angle further.

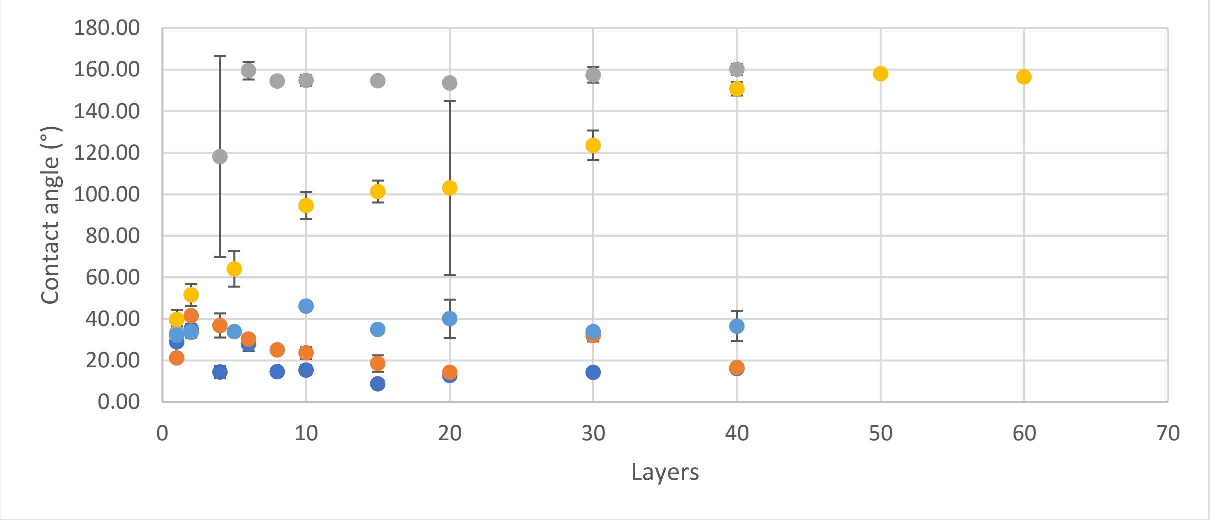

Figure 137: CA for different layers NP (dark blue) 10-20 nm SiO_2 (orange) 500 nm SiO_2 (grey) 10-20 nm SiO_2 made hydrophobic (yellow) 20-30 nm SiO_2 hydrolysis formed (light blue) 300 nm SiO_2 hydrolysis formed

Based on the results presented in Figure 137, it can be inferred that 10-20 nm SiO_2, 500 nm SiO_2, and 300 nm SiO_2 hydrolysis particles do not exhibit any noticeable hydrophobic properties, even after the application of 40 layers. This phenomenon may be attributed to the clustering of nanoparticles upon reaching the surface, leading to different properties compared to individual particles. Although declustering may potentially result in superhydrophobic properties, it was not within the scope of this study. On the other hand, 20-30 nm SiO_2 hydrolysis particles exhibited a gradual increase in hydrophobicity, eventually achieving superhydrophobic properties after the application of 40 layers. This gradual increase may offer advantages when targeting a specific contact angle. Conversely, hydrophobic particles made from 10-20 nm SiO_2 showed a significant increase in hydrophobicity after only 6 layers, reaching a contact angle of 160°. Therefore, fewer of these particles are required to achieve a superhydrophobic surface.

Considering the faster attainment of the desired result using 10-20 nm SiO_2 made hydrophobic particles, they will be used for subsequent analyses.

The optimal parameters for the deposition of 10-20 nm SiO_2 made hydrophobic particles involve placing 10 layers with a concentration of 1 g/l at a distance of 6.5 cm, using a minimum flowrate of 1.50 ml/min, with a shroud pressure of 2.0 psi which results in a contact angle of 160°. To reduce material consumption, it is advisable to conduct further investigations using concentrations ranging from 0.1 g/l to 1 g/l, with these parameters serving as a baseline.

In order to facilitate a comprehensive evaluation of the outcomes observed in Figure 137, SEM images were captured for each variant of nanoparticles across 10 layers. The corresponding results are illustrated in (Figure 138 - Figure 162). Furthermore, images were also obtained for the micropipette-deposited droplet containing hydrophobic particles in the size range of 10-20 nm (Figure 163 - Figure 167). These additional images serve the purpose of comparing the influence exerted by depositing them using the USSC.

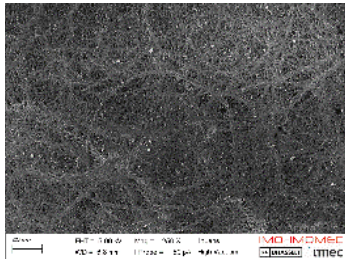

Figure 138: 10 - 20 nm SiO_2 250x

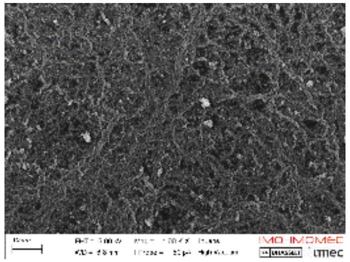

Figure 139: 10 - 20 nm SiO_2 1kx

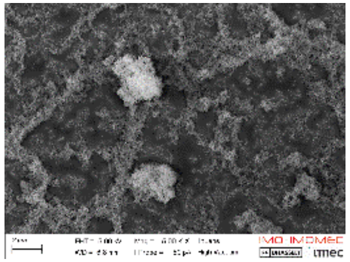

Figure 140: 10 - 20 nm SiO_2 5kx

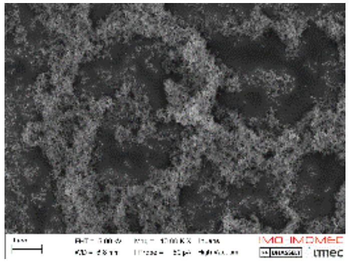

Figure 141: 10 - 20 nm SiO_2 10kx

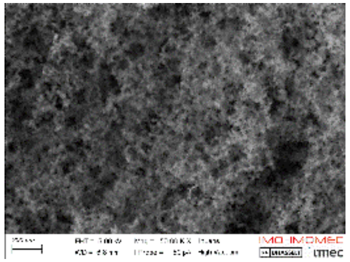

Figure 142: 10 - 20 nm SiO_2 50kx

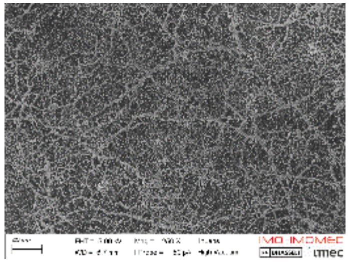

Figure 143: 500 nm SiO_2 250x

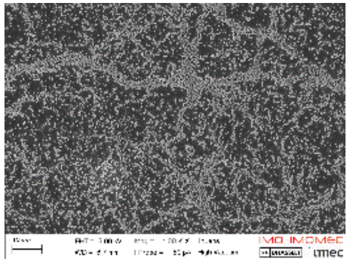

Figure 144: 500 nm SiO_2 1kx

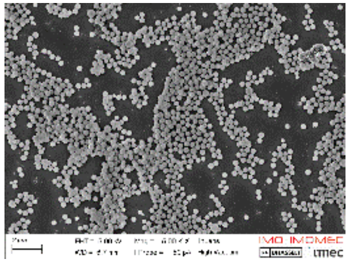

Figure 145: 500 nm SiO_2 5kx

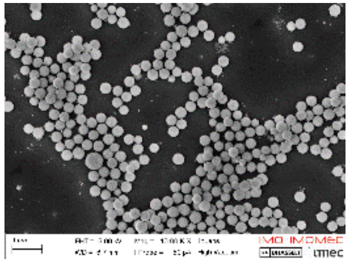

Figure 146: 500 nm SiO_2 10kx

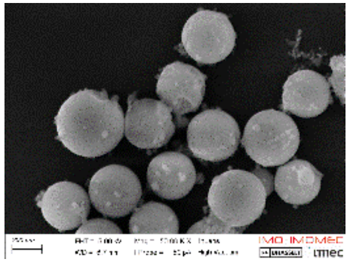

Figure 147: 500 nm SiO_2 50kx

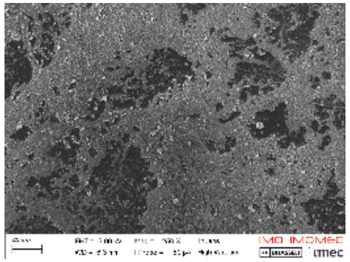

Figure 148: 20 - 30 nm hydrolyse 250x

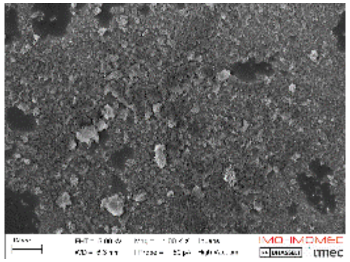

Figure 149: 20 - 30 nm hydrolyse 1kx

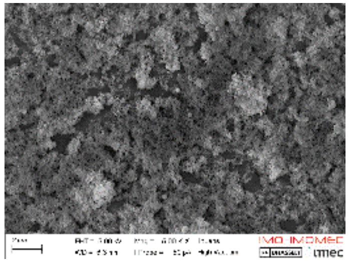

Figure 150: 20 - 30 nm hydrolyse 5kx

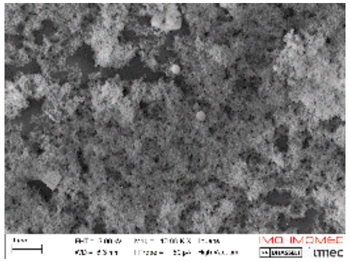

Figure 151: 20 - 30 nm hydrolyse 10kx

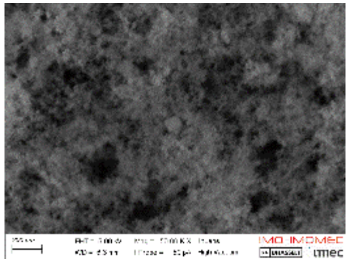

Figure 152: 20 - 30 nm hydrolyse 50kx

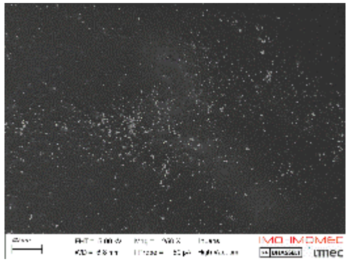
Figure 153: 300 nm hydrolyse 250x

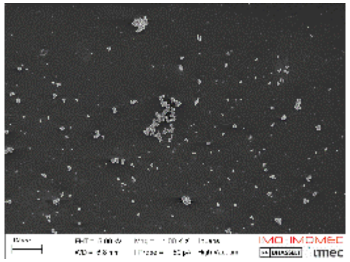
Figure 154: 300 nm hydrolyse 1kx

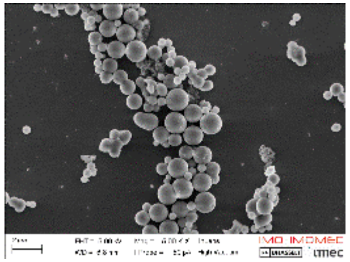
Figure 155: 300 nm hydrolyse 5kx

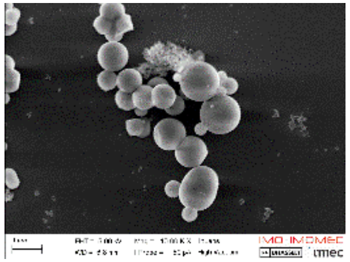
Figure 156: 300 nm hydrolyse 10kx

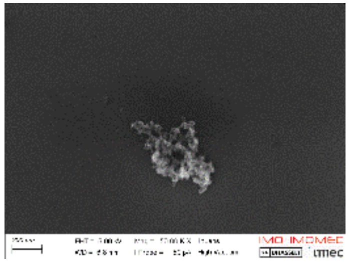
Figure 157: 300 nm hydrolyse 50kx

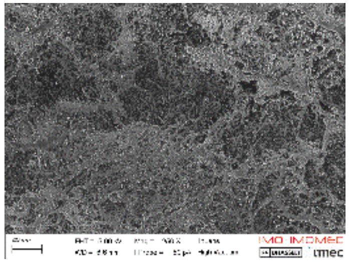
Figure 158: 10 - 20 nm hydrophobic 250x

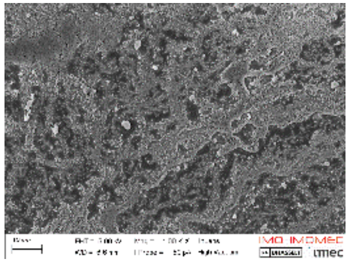
Figure 159: 10 - 20 nm hydrophobic 1kx

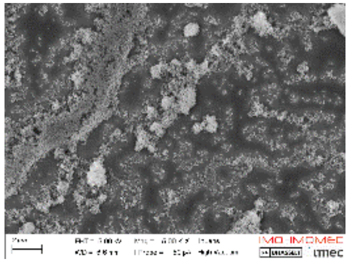
Figure 160: 10 - 20 nm hydrophobic 5kx

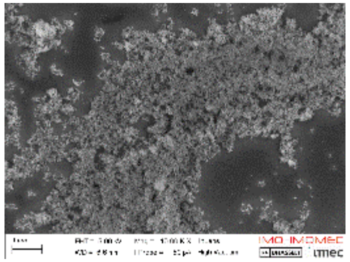
Figure 161: 10 - 20 nm hydrophobic 10kx

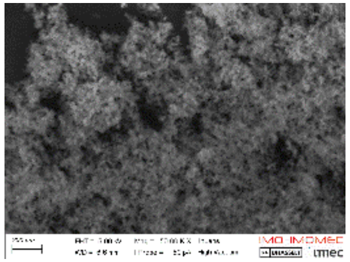
Figure 162: 10 - 20 nm hydrophobic 50kx

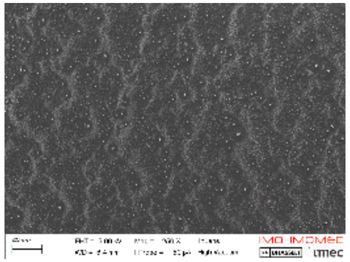
Figure 163: Droplet 250x

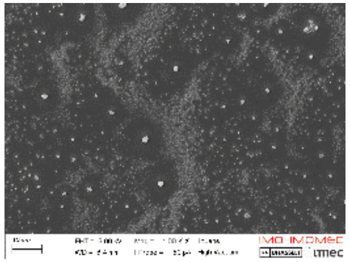
Figure 164: Droplet 1kx

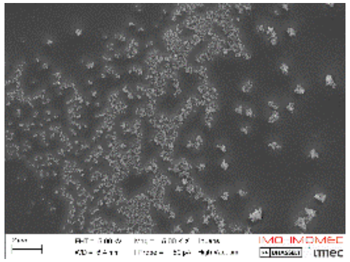
Figure 165: Droplet 5kx

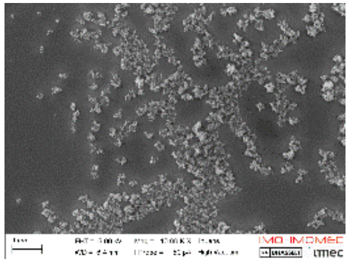
Figure 166: Droplet 10kx

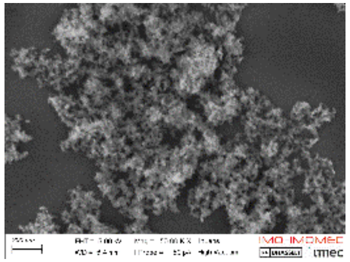
Figure 167: Droplet 50kx

Based on the aforementioned images, one particular sequence stands out prominently: the 300 nm hydrolysis-formed nanoparticles (Figure 153 - Figure 157). In this case, only a minimal number of nanoparticles are visible compared to the other images. This observation suggests that the substrate was not adequately coated with nanoparticles, leading to a lack of hydrophobic properties. Conversely, the hydrolysis-formed nanoparticles in the 20-30 nm size range exhibit extensive coverage across a significant area (Figure 148 - Figure 152). Considering that both types of particles share the same chemical composition, it is possible for the 300 nm nanoparticles to possess hydrophobic characteristics if multiple nanoparticles are present on the surface.

Regarding the non-hydrolysis particles, no apparent visual distinctions are apparent to explain why the hydrophobic particles demonstrate greater hydrophobicity than the others. This discrepancy may be attributed to the presence of functional groups on these particles, as the chemical composition among the three particle types can differ. The 10-20 nm hydrophobic particles are expected to contain a higher concentration of silane groups on the silica surface, which possess strong hydrophobic properties. Conversely, the 10-20 nm and 500 nm SiO_2 particles are likely to be more abundant in -OH groups, resulting in the opposite effect of hydrophilicity.

Regarding the deposited droplet, a wavy pattern is discernible (Figure 163), indicating that the distribution of nanoparticles was not as homogeneous as in the cases where the USSC technique was employed.

4.2.3 PVDF & SiO_2 hydrophobic nanoparticles

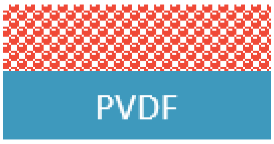

Figure 168: PVDF & hydrophobic NP stacking layer

When PVDF is optimally coated with the nanoparticles according to their optimal settings, a contact angle of only 107° is achieved. This value is only slightly higher than PVDF without nanoparticles. The root cause for this is that the PVDF layer provides a less even surface than glass, which necessitates the application of multiple layers of nanoparticles to cover the entire PVDF surface.

Figure 169 illustrates the impact of the number of nanoparticle layers on PVDF on the contact angle.

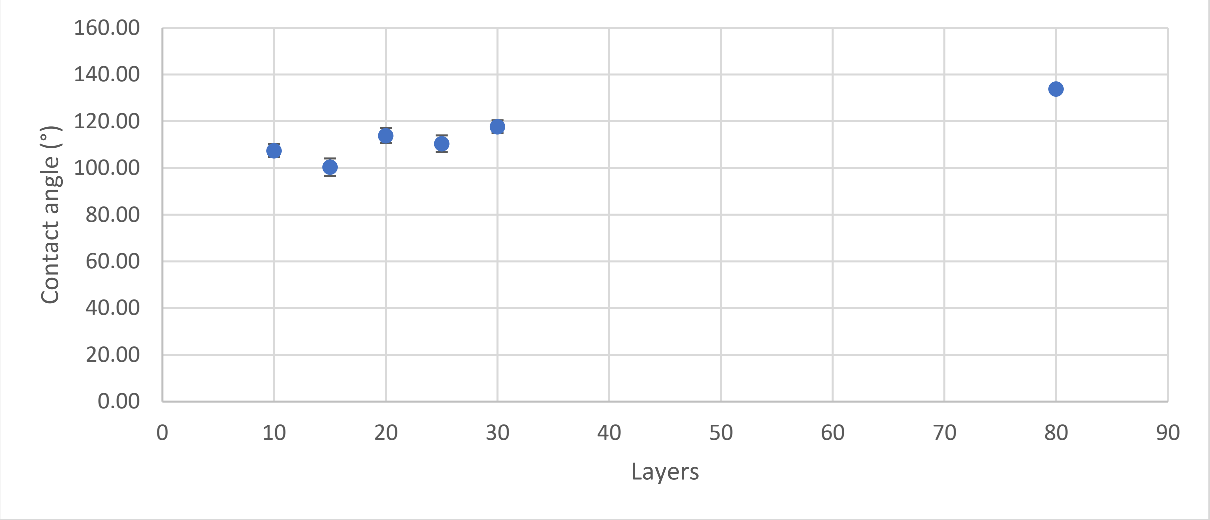

Figure 169: CA with different layers 1 g/l NP on top of PVDF

As depicted in Figure 169, an increase in the number of nanoparticle layers results in a corresponding increase in the contact angle. However, this trend is moderate in nature, as even with the deposition of 80 layers, the surface has not yet exhibited superhydrophobic behaviour.

To expedite the attainment of a higher contact angle on PVDF, the concentration of nanoparticles was increased, and the outcomes for 20 layers are demonstrated in Figure 170.

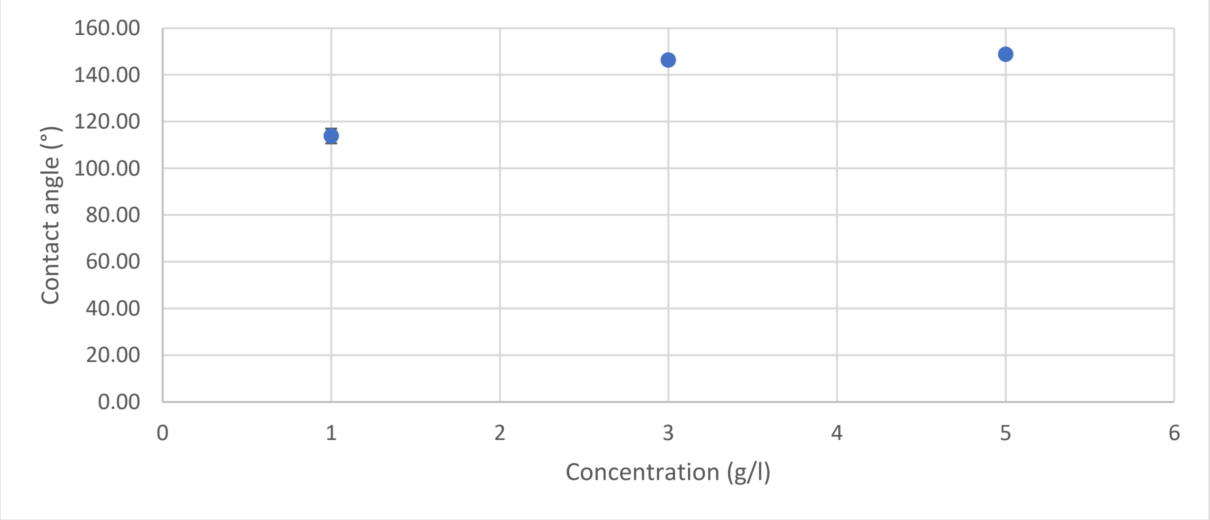

Figure 170: CA for different concentrations of nanoparticles

The impact of increasing the concentration of nanoparticles is significant, as demonstrated by the outcomes presented in Figure 170. Notably, at a concentration of 3 g/l, the contact angle begins to approach its maximum value. Further increasing the concentration to 5 g/l results in only a negligible increase in the contact angle.

The influence of the number of layers with higher concentrations of 5 g/l nanoparticles is checked in Figure 171.

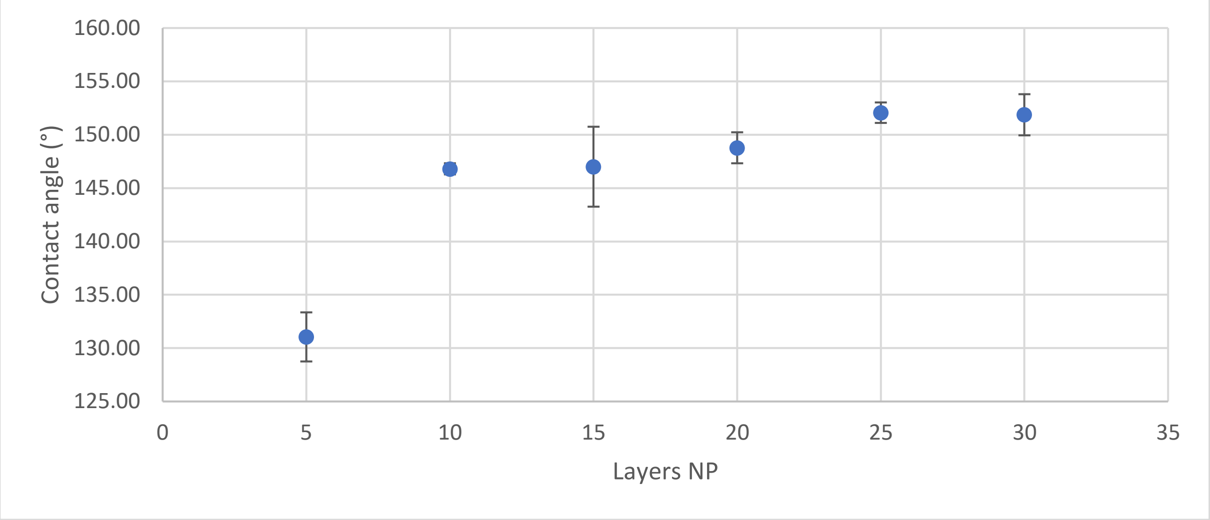

Figure 171: CA with different layers 5 g/l NP on top of PVDF

Working with a nanoparticle concentration of 5 g/l (Figure 171), a substantial increase in the contact angle is apparent compared to that observed with 1 g/l (Figure 169). After the application of 25 layers, the contact angle ceases to increase, signifying the attainment of the maximum value. This maximum contact angle measures 155°, which is 5° lower than the maximum contact angle achievable without PVDF.

In order to achieve the desired hydrophobicity on the optimized PVDF layer, a deposition process will be carried out using 30 layers of hydrophobic nanoparticles at a concentration of 5g/l. The deposition parameters, including the height, flow rate, and shroud pressure, will be set at 6.5 cm, 1.50 ml/min, and 2.0 psi, respectively. These parameters are consistent with the conditions used for depositing nanoparticles solely on the glass substrate.

4.2.4 PVDF mixed SiO_2 hydrophobic nanoparticles

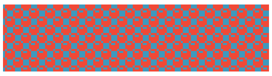

Figure 172: PVDF mixed hydrophobic NP stacking layer

This involves looking at how the contact angle is affected when PVDF and 10 - 20 nm SiO_2 hydrophobic nanoparticles are applied in the same layer by mixing them.

In the preliminary experiments, a concentration of 2.5 wt% PVDF and 1g/l nanoparticles were employed. The deposition was executed at a height of 6.5 cm with a flowrate of 1.50 ml/min and a shroud pressure of 2.0 psi. The number of layers was modified, and the resultant contact angles were recorded, as illustrated in Figure 173.

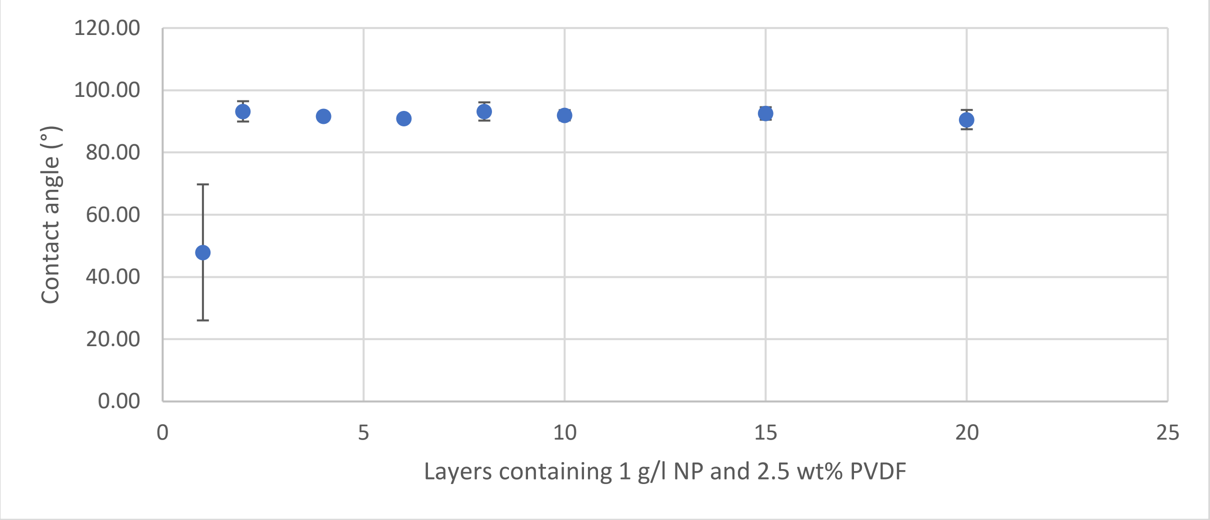

Figure 173: CA for different mixed layers of 1 g/l NP and 2.5 wt% PVDF

The maximum contact angle was achieved with the deposition of only 4 layers of the mixture, with a value of 90°, which is inferior to that observed with PVDF alone (Figure 173).

To increase the contact angle of the layer, the influence of the concentration of nanoparticles is considered. Here, 10 layers are deposited each time since in Figure 173 the maximum was already reached at barely 4 layers.

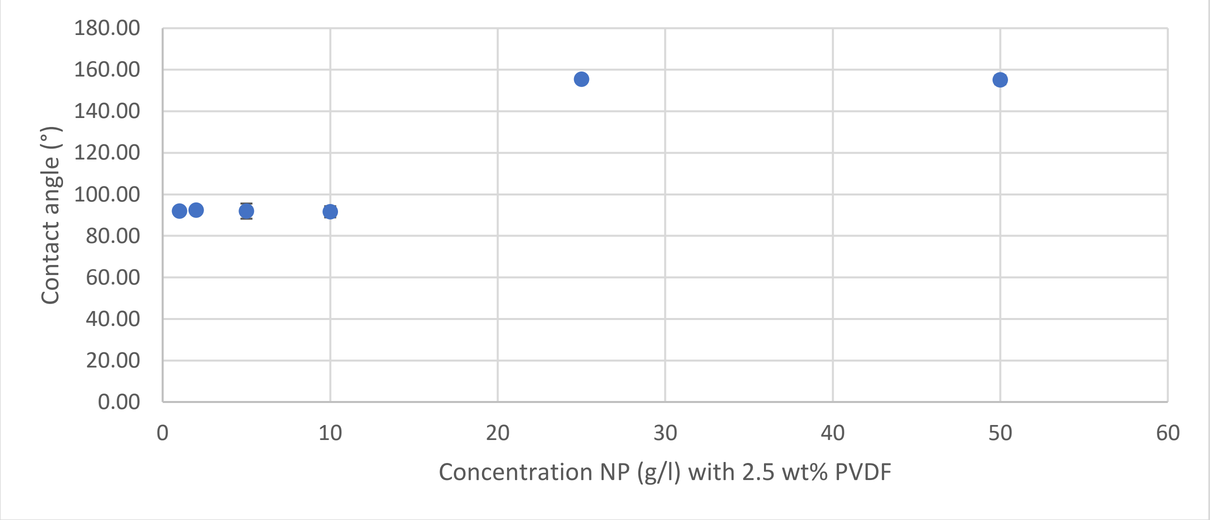

Figure 174: CA for increasing concentration NP with 2.5 wt% PVDF

Upon increasing the nanoparticle concentration to 10 g/l, no noticeable distinction in the contact angle is evident in comparison to that obtained with 1 g/l. However, elevating the concentration to 25 g/l results in a contact angle of 150°. Subsequently, further elevating the concentration to 50 g/l does not produce any increase in the contact angle. As such, the maximum is achieved with only 10 layers of 25 g/l nanoparticles.

Due to time constraints for this study, it was decided to deposit 25 g/l hydrophobic nanoparticles with 2.5 wt% PVDF. Alternatively, concentrations of 15 g/l and 20 g/l may be worth further analysis for achieving optimal hydrophobicity with a lower concentration. In such circumstances, it is likely that multiple layers would be required to achieve the desired level of hydrophobicity. The selected coating is applied in multiple layers, as depicted in Figure 175, to observe the point at which the entire surface achieves optimal hydrophobicity.

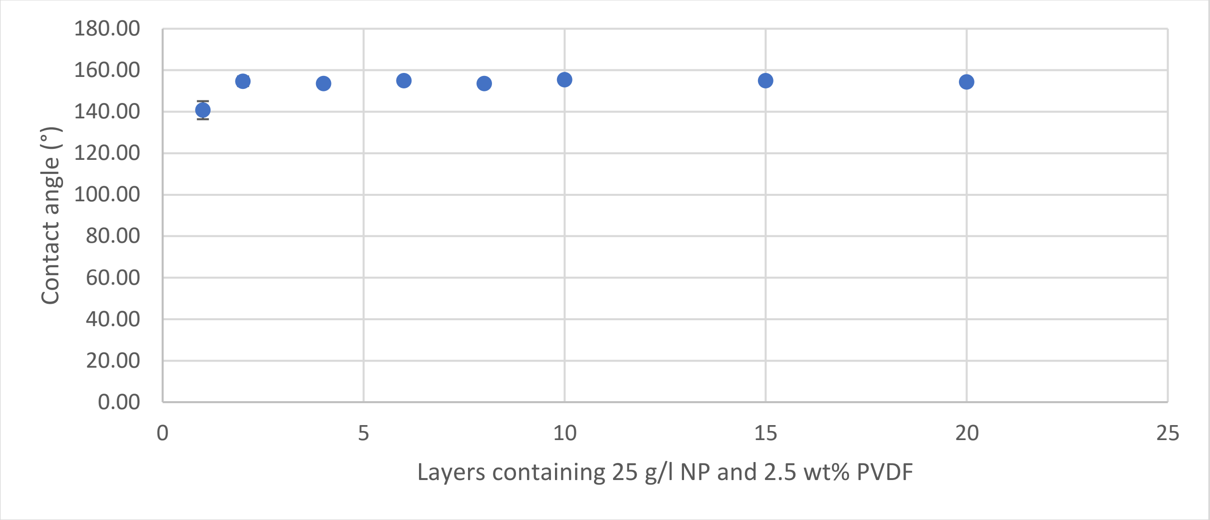

Figure 175: CA for different mixed layers of 25 g/l NP and 2.5 wt% PVDF

As illustrated in Figure 175, it has been observed that the highest contact angle, reaching a value of 155°, is attained upon the deposition of two layers of the coating. Subsequent additional layers do not contribute to an increase in the contact angle but rather serve to sustain it at this maximum level.

In order to achieve optimal level of hydrophobicity in the mixed layer, a carefully formulated mixture will be used, consisting of 2.5m% PVDF and 25 g/l hydrophobic nanoparticles. The deposition process will involve the application of 5 layers of this mixture. The deposition parameters, including the height, flow rate, and shroud pressure, will be maintained at 6.5 cm, 1.50 ml/min, and 2.0 psi, respectively, mirroring the conditions utilized for depositing nanoparticles solely on the glass substrate.

4.2.5 PVDF & PVDF mixed SiO_2 hydrophobic nanoparticles

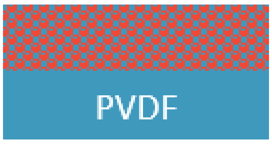

Figure 176: PVDF & PVDF mixed NP stacking layer

In this stage, a supplementary layer will be applied on top of the previously optimized PVDF layer. This additional layer will comprise 2.5 wt% PVDF and 25 g/l hydrophobic nanoparticles.

To determine the optimum number of layers to apply on top of the PVDF layer, contact angle measurements were conducted until the maximal contact angle for this layer stacking was achieved. The results of these measurements are presented in Figure 177.

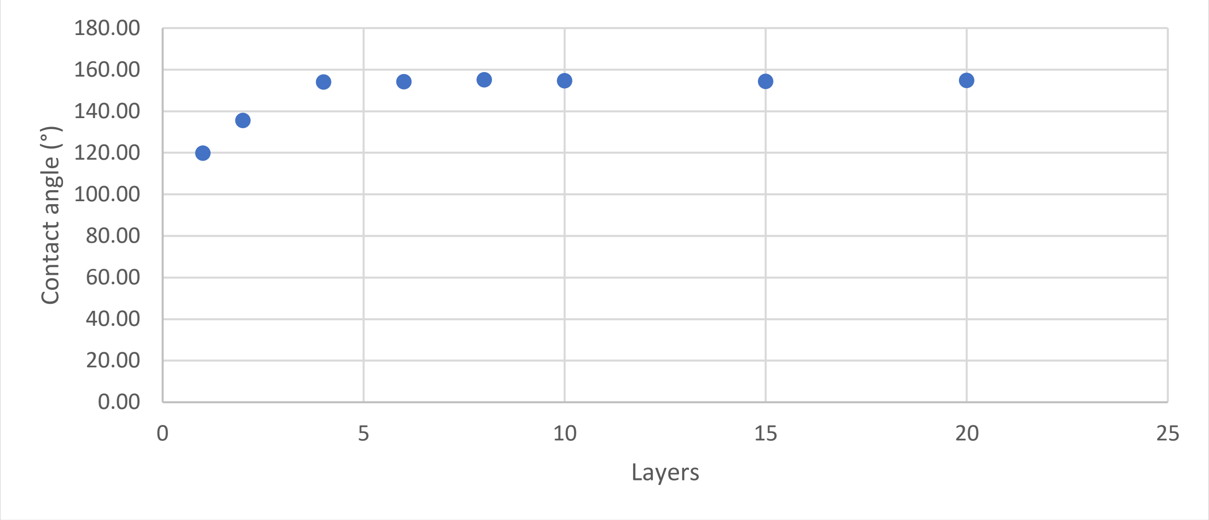

Figure 177: CA for depositing mixed PVDF & NP on optimised PVDF

The contact angle exhibits a value of 120° upon the application of a single layer. With successive layering, the contact angle progressively rises, reaching its pinnacle at 155° upon the application of four layers. It is worth noting that beyond this point, further augmentation of the layer count does not yield any significant increase in the contact angle.

To attain the desired level of hydrophobicity on the optimized PVDF layer, a meticulous deposition process will be conducted using 8 layers of a precisely formulated mixture consisting of 2.5m% PVDF and 25g/l hydrophobic nanoparticles. The deposition parameters, namely the height, flow rate, and shroud pressure, will be carefully maintained at 6.5 cm, 1.50 ml/min, and 2.0 psi, respectively. These specific parameters align with the conditions employed during the deposition of nanoparticles solely on the glass substrate.

4.3 Self-cleaning properties

The self-cleaning experiments are conducted on every stack variant depicted in Figure 34. The parameters are chosen to ensure the optimal hydrophobicity. These parameters, for every stack variant, are shown in Table 6 - Table 10. In order to facilitate a more comprehensive comparison, this parameter was also evaluated on the purified glass employed as the substrate.

PVDF (2.5 wt%)

Table 6: Parameters tested layers of PVDF

Height (cm)	Flowrate (ml/min)	Layers	Shroud (psi)
3.5	1.50	10	2.0

10-20 nm hydrophobic SiO_2 (1 g/l)

Table 7: Parameters tested layers of NP

Height (cm)	Flowrate (ml/min)	Layers	Shroud (psi)
6.5	1.50	10	2.0

PVDF (2.5 wt%) & 20-30 nm hydrophobic SiO_2 (5 g/l)

Table 8: Parameters tested layers of PVDF & NP

PVDF			
Height (cm)	**Flowrate (ml/min)**	**Layers**	**Shroud (psi)**
3.5	1.50	10	2.0
NP			
Height (cm)	**Flowrate (ml/min)**	**Layers**	**Shroud (psi)**
6.5	1.50	30	2.0

PVDF (2.5 wt%) mixed 20-30 nm hydrophobic SiO_2 (25 g/l)

Table 9: Parameters tested layers of PVDF mixed NP

Height (cm)	**Flowrate (ml/min)**	**Layers**	**Shroud (psi)**
6.5	1.50	5	2.0

PVDF (2.5 wt%) & PVDF (2.5 wt%) mixed 20-30 nm hydrophobic SiO_2 (25 g/l)

Table 10: Parameters tested layers of PVDF & PVDF mixed NP

PVDF			
Height (cm)	**Flowrate (ml/min)**	**Layers**	**Shroud (psi)**
3.5	1.50	10	2.0
PVDF mixed NP			
Height (cm)	**Flowrate (ml/min)**	**Layers**	**Shroud (psi)**
6.5	1.50	8	2.0

Additionally, two supplementary coatings are examined as post-treatments for the PVDF stack and the incorporation of hydrophobic nanoparticles. The first treatment involves the application of an additional layers of acetone on top of the existing coating (Figure 178). This is accomplished using the Ultrasonic Spray Coater (USSC) with a controlled flowrate of 1.00 ml/min for 10 layers, positioned at a height of 6.5 cm, and a nozzle speed of 50 mm/sec. Simultaneously, a hotplate is set to maintain a temperature of 40°C to facilitate the acetone's evaporation and coating consolidation. For the second treatment, the coated sample is placed in an oven at a temperature of 170°C for a duration of 30 minutes (Figure 179).

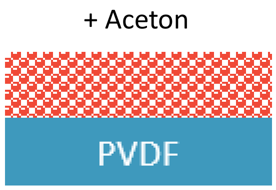

Figure 178: PVDF & NP & acetone

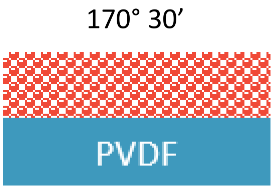

Figure 179: PVDF & NP & heating

An endeavour was undertaken to achieve a uniform application of graphite powder utilizing an ultrasonic spray coater. Acetone and demineralized water were selected as the solvents for this purpose. By utilizing acetone, the applied coating of graphite is transiently dissolved, allowing the graphite particles to infiltrate the coating rather than positioning on the surface. Consequently, the applied graphite becomes impervious to removal by water. On the other hand, the use of demineralized water causes water droplets to repel from the surface upon contact due to the superhydrophobic coatings. As a result, the distribution of the graphite powder was accomplished through the utilization of an air spray system. The distribution of this method can be observed on the tested coatings in (Figure 180 - Figure 187), along with the subsequently purified coatings (Figure 188 - Figure 195).


Figure 180: Purified glass before cleaning


Figure 181: PVDF before cleaning


Figure 182: NP before cleaning


Figure 183: PVDF & NP before cleaning


Figure 184: PVDF mixed NP before cleaning


Figure 185: PVDF & PVDF mixed NP before cleaning


Figure 186: Post-treatment acetone before cleaning


Figure 187: Post-treatment heating before cleaning


Figure 188: Purified glass after cleaning


Figure 189: PVDF after cleaning


Figure 190: NP after cleaning


Figure 191: PVDF & NP after cleaning

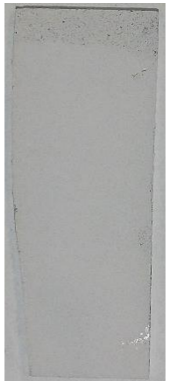
Figure 192: PVDF mixed NP after cleaning


Figure 193: PVDF & PVDF mixed NP after cleaning


Figure 194: Post-treatment acetone after cleaning


Figure 195: Post-treatment heating after cleaning

Despite the purging process, several glasses still exhibit residual dirt along the top edge. This occurrence can be attributed to water droplets not landing precisely at the top of the glass. Consequently, measurements are conducted below this line as no purification was carried out above it. In the case of the coating solely composed of hydrophobic nanoparticles, only a section has undergone purification. Thus, measurements will exclusively focus on this localized purification area.

Regarding PVDF & NP (Figure 191), another area of contamination is noticeable at the bottom right. This can be attributed to the absence of glass immediately above that spot due to uneven breakage. As a result, the water droplets, intended to clear this region, cascade alongside the glass instead. To optimize results, it is advisable to position the widest side of the glass upward when applying the drops. In Figure 188, the glass exhibits coffee rings, which formed due to water failing to slide off and instead accumulating in those regions.

The comparative analysis of the relative area of graphite before and after purification is depicted in Figure 196.

1	PVDF
2	NP
3	PVDF & NP
4	PVDF mixed NP
5	PVDF & PVDF mixed NP
6	3 with acetone
7	3 with heating
8	Glass

Figure 196: Graphite reduction

When PVDF is employed as the sole coating, the surface exhibits an increased level of hydrophobicity; however, there is no discernible enhancement in purification capabilities. This outcome can be attributed to the PVDF coating causing an increase in the roughness of the glass surface, resulting in crevices where small graphite particles can accumulate. The surfaces displaying the highest levels of purity are those that have been coated with a combination of PVDF and nanoparticles, followed by subsequent post-treatment procedures. Surprisingly, the uncoated glass substrate outperformed expectations. This can be attributed to the fact that the glass surface possesses the lowest degree of roughness, which facilitates the drainage of contaminants. It is important to note that if a substrate rougher than glass were utilized in a similar experiment, the self-purifying effect of these coatings would likely be more effective.

4.4 Sliding angle

The sliding angle is determined for the different coatings on Table 6 - Table 10, as well as 2 additional variants of Figure 178 & Figure 179. The results are shown in Figure 197.

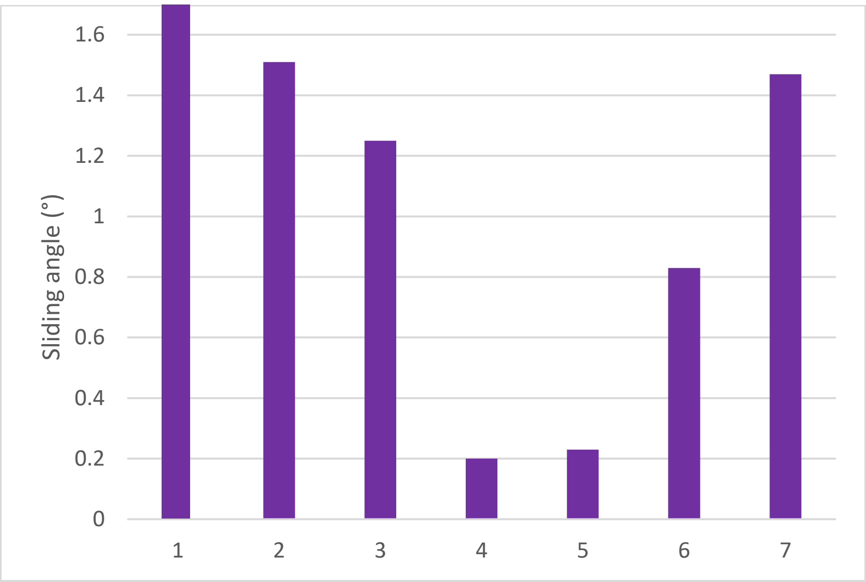

1	PVDF
2	NP
3	PVDF & NP
4	PVDF mixed NP
5	PVDF & PVDF mixed NP
6	3 with acetone
7	3 with heating

Figure 197: Sliding angle for different coatings

Based on the data obtained from the sliding angle experiments (Figure 197), there is a clear outlier that stands out. The sliding angle value for PVDF is significantly higher, rendering a meaningful comparison with the other coatings unfeasible. In the case of PVDF, the lathe was rotated up to an angle of 95° without the droplet leaving the field of view. This behaviour can be attributed to PVDF having the lowest hydrophobicity among the tested coatings, as well as possessing higher surface roughness. Conversely, the remaining coatings exhibited sliding angles below 2°. Notably, when the top layer of the coating consisted of a PVDF mixed nanoparticles, a significantly lower sliding angle value of approximately 0.2° was observed.

4.5 Adhesion properties

The demonstration of adhesion properties was not feasible within the given time constraints. Attempts have been made to display adhesion properties using manual and automatic tape tests. In both methods, complete detachment of the applied coating from the glass substrate was observed, or adhesive residues from the tape remained affixed to the substrate, posing challenges for their separation without causing damage to the coating itself. Nonetheless, empirical observations indicate that a coating solely composed of nanoparticles exhibits inadequate adherence to the substrate, as it can be easily removed with minor contact from tweezers (Figure 198). In contrast, when nanoparticles are doped in conjunction with PVDF, their removal from the substrate becomes more challenging (Figure 199). Optimal adhesion of the nanoparticles is achieved when they are applied concurrently with PVDF in a PVDF-nanoparticle mixture.

Figure 198: Scratch on NP

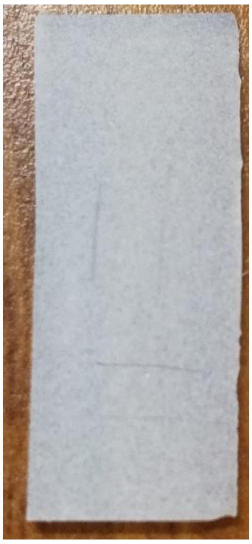

Figure 199: Scratch on PVDF mixed NP

In order to enhance the adhesion properties of nanoparticles on PVDF, a method was selected whereby the nanoparticles were embedded within the PVDF layer using a combination of acetone or heat treatment (Figure 178 & Figure 179).

In the future, a comprehensive scientific experiment will be conducted to assess the adhesion properties of the materials listed in Table 6 - Table 10, including the two additional coatings undergoing post-treatment (Figure 178 & Figure 179).

4.6 SEM

SEM images were captured for all optimal coatings incorporating nanoparticles (Table 7 - Table 10) and the two post-treatment methods (Figure 178 & Figure 179), encompassing both surface (Figure 200 - Figure 217) and cross-sectional views (Figure 218 & Figure 219).

4.6.1 Surface

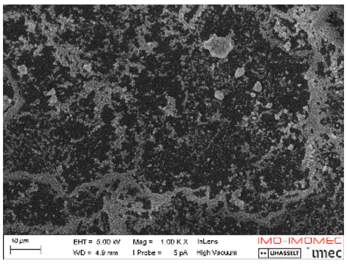
Figure 200: Nanoparticles 1kx

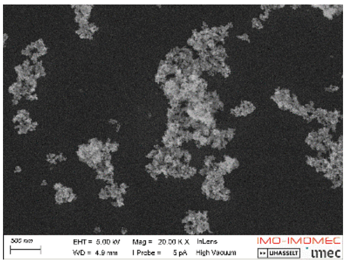
Figure 201: Nanoparticles 20kx

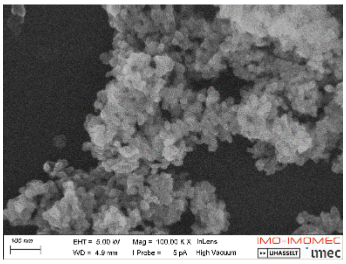
Figure 202: Nanoparticles 100kx

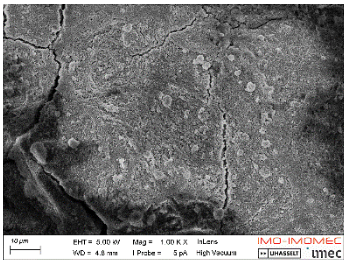
Figure 203: PVDF & NP 1kx

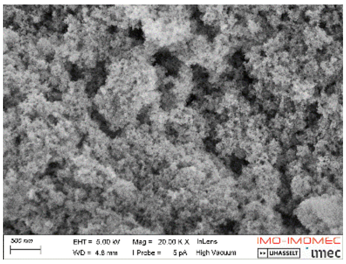
Figure 204: PVDF & NP 20kx

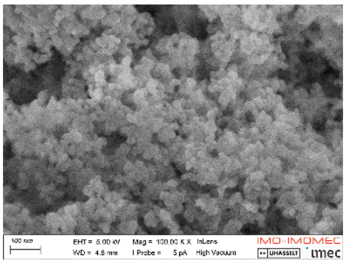
Figure 205: PVDF & NP 100kx

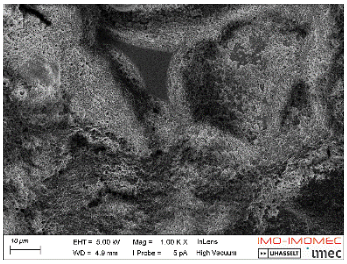
Figure 206: PVDF mixed NP 1kx

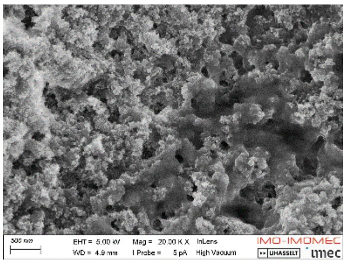
Figure 207: PVDF mixed NP 20kx

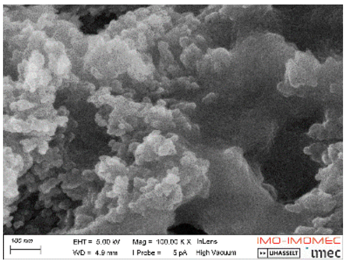
Figure 208: PVDF mixed NP 100kx

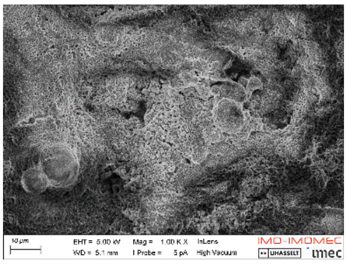
Figure 209: PVDF & PVDF mixed NP 1kx

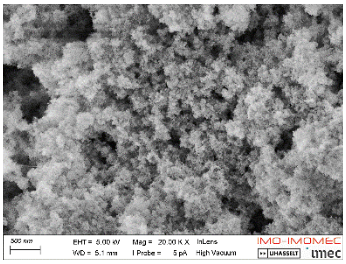
Figure 210: PVDF & PVDF mixed NP 20kx

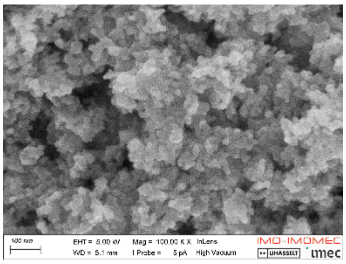
Figure 211: PVDF & PVDF mixed NP 100kx

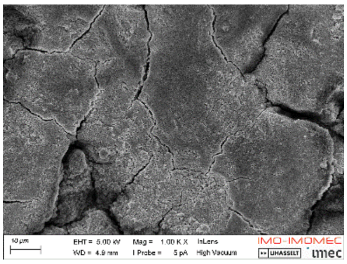
Figure 212: Post-treatment acetone after cleaning 1kx

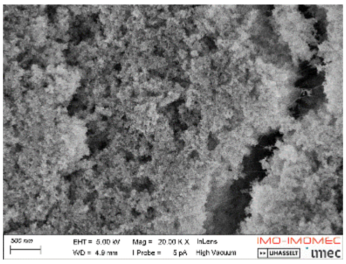
Figure 213: Post-treatment acetone after cleaning 20kx

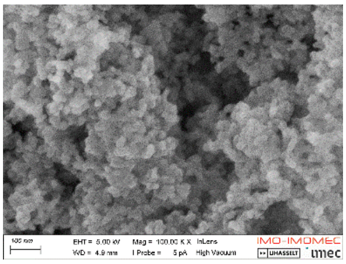
Figure 214: Post-treatment acetone after cleaning 100kx

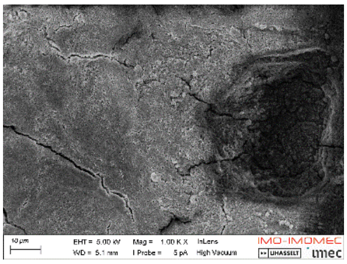

Figure 215: Post-treatment heating after cleaning 1kx

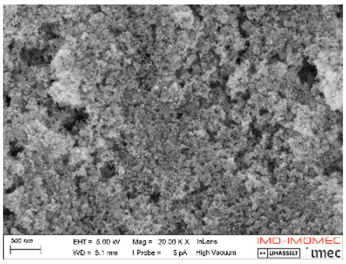

Figure 216: Post-treatment heating after cleaning 20kx

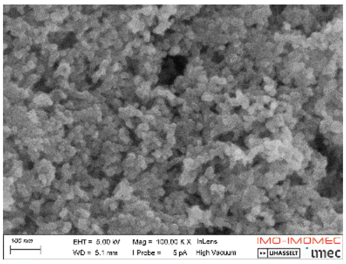

Figure 217: Post-treatment heating after cleaning 100kx

The SEM images obtained suffer from reduced quality due to sample charging. In cases where only nanoparticles are deposited, a significant portion of the glass substrate remains visible. However, when PVDF is utilized, the glass substrate becomes entirely obscured. In Figure 208, it is evident that the PVDF coating does not uniformly encapsulate the nanoparticles throughout. Conversely, no discernible variations are apparent in the remaining images.

4.6.2 Cross-section

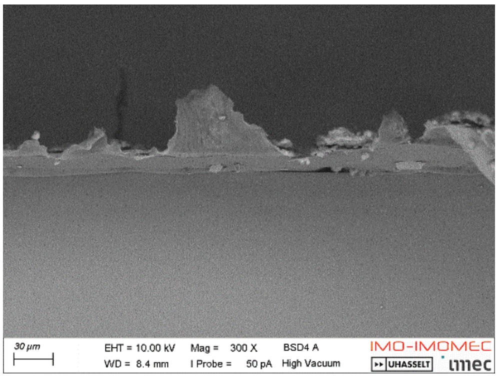

Figure 218: Nanoparticles 300x

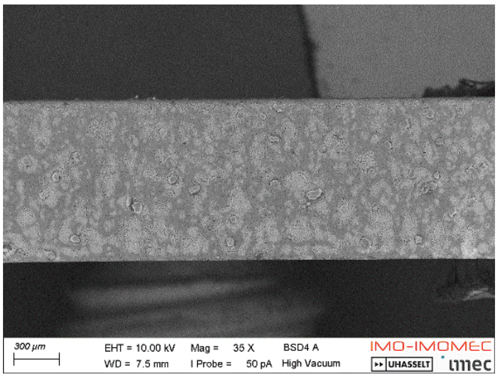

Figure 219: Post-treatment acetone after cleaning 35x

The cross-sectional analyses were conducted by fracturing the glass substrate on which the applied coating was placed, thereby revealing the positioning of the nanoparticles in the coating. This comparison is particularly notable when contrasting post-treated coatings with those lacking post-treatment (Figure 178 & Figure 179). However, this testing method yielded successful results only for the coating composed solely of nanoparticles. In Figure 218, the nanoparticles are visible on the glass substrate. Conversely, in the coatings containing PVDF, no discernible coating is detectable on the glass substrate (Figure 219). One plausible explanation for this observation is that PVDF causes the coating to stretch and subsequently detach from the breaking surface.

5. Conclusion

The use of nanoparticles has demonstrated the capability to significantly enhance the contact angle up to a maximum of 160°. However, it is important to note that nanoparticles alone exhibit poor adhesion properties. To overcome this limitation, the incorporation of nanoparticles with PVDF has shown promise in improving adhesion on glass. Nevertheless, this approach can be cost-prohibitive due to the higher concentration of nanoparticles needed.

Alternatively, it has been discovered that employing a layered approach, which involves incorporating a PVDF layer in combination with a layer comprised of mixed nanoparticles and PVDF, demonstrates comparable properties to the NP-PVDF mixture.

The self-cleaning tests revealed that PVDF exhibits the poorest self-cleaning performance, even worse than purified glass, primarily attributable to its surface roughness. On the other hand, all the other coatings subjected to testing demonstrated highly favourable characteristics, effectively eliminating at least 98% of the applied graphite.

The selection of the appropriate approach depends on the specific requirements of the application at hand, as well as the cost constraints involved. Careful consideration should be given to strike a balance between achieving desired properties and managing expenses effectively.

For future research, it is advisable to explore the adhesion properties of the coatings, followed by conducting tests on substrates characterized by rougher surfaces. This approach would provide valuable insights into the performance and suitability of the coatings under more challenging conditions.

Reference list

[1] A. Hooda, M. S. Goyat, J. K. Pandey, A. Kumar, and R. Gupta, "A review on fundamentals, constraints and fabrication techniques of superhydrophobic coatings," *Progress in Organic Coatings*, vol. 142. Elsevier B.V., May 01, 2020. doi: 10.1016/j.porgcoat.2020.105557.

[2] "Design and Function of Spray Gun." http://www.secondchancegarage.com/public/635.cfm (accessed Mar. 24, 2023).

[3] "Spray gun | pneumatic device | Britannica." https://www.britannica.com/technology/spray-gun (accessed Mar. 24, 2023).

[4] "Spray Guns: Getting Started - StewMac." https://www.stewmac.com/video-and-ideas/online-resources/learn-about-instrument-finishing-and-finish-repair/spray-guns-getting-started/ (accessed Mar. 24, 2023).

[5] "Spray Coating | Coating & Dispensing Methods | Coating & Dispensing Technology | KEYENCE America." https://www.keyence.com/ss/products/measure/sealing/coater-type/spray.jsp (accessed Mar. 19, 2023).

[6] "Ultrasonic Spray Benefits | Sono-Tek." https://www.sono-tek.com/ultrasonic-coating/ultrasonic-spray-benefits/ (accessed Nov. 11, 2022).

[7] "Conventional (Air) Spray Applications - KANSAI ALTAN." https://www.kansaialtan.com.tr/conventional-air-spray-applications (accessed Mar. 24, 2023).

[8] S. Slegers, M. Linzas, J. Drijkoningen, J. D'Haen, N. Reddy, and W. Deferme, "Surface Roughness Reduction of Additive Manufactured Products by Applying a Functional Coating Using Ultrasonic Spray Coating," *Coatings*, vol. 7, no. 12, p. 208, Nov. 2017, doi: 10.3390/coatings7120208.

[9] S. K. Sahoo, B. Manoharan, and N. Sivakumar, "Introduction: Why perovskite and perovskite solar cells?," in *Perovskite Photovoltaics: Basic to Advanced Concepts and Implementation*, Elsevier, 2018, pp. 1–24. doi: 10.1016/B978-0-12-812915-9.00001-0.

[10] D. Lončarević and Ž. Čupić, "The perspective of using nanocatalysts in the environmental requirements and energy needs of industry," *Industrial Applications of Nanomaterials*, pp. 91–122, Jan. 2019, doi: 10.1016/B978-0-12-815749-7.00004-9.

[11] J. E. ten Elshof, "Chemical solution deposition techniques for epitaxial growth of complex oxides," *Epitaxial Growth of Complex Metal Oxides*, pp. 69–93, May 2015, doi: 10.1016/B978-1-78242-245-7.00004-X.

[12] M. Joshi and B. S. Butola, "Application technologies for coating, lamination and finishing of technical textiles," *Advances in the Dyeing and Finishing of Technical Textiles*, pp. 355–411, 2013, doi: 10.1533/9780857097613.2.355.

[13] E. K. Hussmann, "Dip coatings: characteristics, properties, applications." [Online]. Available: http://spiedl.org/terms

[14] D. Frederichi, M. H. N. O. Scaliante, and R. Bergamasco, "Structured photocatalytic systems: photocatalytic coatings on low-cost structures for treatment of water contaminated with

micropollutants—a short review," *Environmental Science and Pollution Research*, vol. 28, no. 19, pp. 23610–23633, May 2021, doi: 10.1007/S11356-020-10022-9.

[15] J. X. J. Zhang and K. Hoshino, "Fundamentals of nano/microfabrication and scale effect," *Molecular Sensors and Nanodevices*, pp. 43–111, 2019, doi: 10.1016/B978-0-12-814862-4.00002-8.

[16] A. Mishra, N. Bhatt, and A. K. Bajpai, "Nanostructured superhydrophobic coatings for solar panel applications," *Nanomaterials-Based Coatings: Fundamentals and Applications*, pp. 397–42, Jan. 2019, doi: 10.1016/B978-0-12-815884-5.00012-0.

[17] B. S. Yilbas, A. Al-Sharafi, and H. Ali, "Surfaces for Self-Cleaning," *Self-Cleaning of Surfaces and Water Droplet Mobility*, pp. 45–98, 2019, doi: 10.1016/B978-0-12-814776-4.00003-3.

[18] F. Mammeri, "Nanostructured flexible PVDF and fluoropolymer-based hybrid films," *Frontiers of Nanoscience*, vol. 14, pp. 67–101, Jan. 2019, doi: 10.1016/B978-0-08-102572-7.00003-9.

[19] R. Rajan and A. B. Pandit, "Correlations to predict droplet size in ultrasonic atomisation." [Online]. Available: www.elsevier.nl/locate/ultras

[20] S. Bose, S. S. Keller, T. S. Alstrøm, A. Boisen, and K. Almdal, "Process Optimization of Ultrasonic Spray Coating of Polymer Films," *Langmuir*, vol. 29, no. 23, pp. 6911–6919, Jun. 2013, doi: 10.1021/la4010246.

[21] R. J. Lano, "Ultrasonic Atomization of Liquids," 1962. [Online]. Available: http://asadl.org/journals/doc/ASALIB-home/info/terms.jsp

[22] "Ultrasonic Vibration Atomization Powder Manufacturing Equipment - Hunan Skyline Smart Material&Technology Co., Ltd." http://www.skylinesmt.com/mobile/en-US/xjflblsczb/325.html (accessed Apr. 28, 2023).

[23] "BLENDS OF POLY(N-VINYL-2-PYRROLIDONE) AND DIHYDRIC PHENOLS: THERMAL AND INFRARED SPECTROSCOPIC STUDIES. PART IV." https://www.scielo.cl/scielo.php?script=sci_arttext&pid=S0717-97072013000400032 (accessed May 06, 2023).

[24] N. Gatica, L. Soto, C. Moraga, and L. Vergara, "BLENDS OF POLY(N-VINYL-2-PYRROLIDONE) AND DIHYDRIC PHENOLS: THERMAL AND INFRARED SPECTROSCOPIC STUDIES. PART IV," *Journal of the Chilean Chemical Society*, vol. 58, no. 4, pp. 2048–2052, 2013, doi: 10.4067/S0717-97072013000400032.

[25] "Polyvinylpyrrolidone (PVP) | Products | NIPPON SHOKUBAI." https://www.shokubai.co.jp/en/products/detail/pvp/ (accessed May 06, 2023).

[26] B. L. Wang, J. L. Wang, D. D. Li, K. F. Ren, and J. Ji, "Chitosan/poly (vinyl pyrollidone) coatings improve the antibacterial properties of poly(ethylene terephthalate)," *Appl Surf Sci*, vol. 258, no. 20, pp. 7801–7808, Aug. 2012, doi: 10.1016/j.apsusc.2012.03.181.

[27] M. Zheng, M. Gu, Y. Jin, and G. Jin, "Optical properties of silver-dispersed PVP thin film," 2001.

[28] C. Vigneswaran, M. Ananthasubramanian, and P. Kandhavadivu, "Biotechnology and biomaterials for hygienic and health care textiles," *Bioprocessing of Textiles*, pp. 398–433, 2014, doi: 10.1016/B978-93-80308-42-5.50008-1.

[29] “Polylactic acid Mw 60,000 26100-51-6.” https://www.sigmaaldrich.com/BE/en/product/aldrich/38534 (accessed May 06, 2023).

[30] T. Casalini, F. Rossi, A. Castrovinci, and G. Perale, “A Perspective on Polylactic Acid-Based Polymers Use for Nanoparticles Synthesis and Applications,” *Front Bioeng Biotechnol*, vol. 7, p. 259, Oct. 2019, doi: 10.3389/FBIOE.2019.00259/BIBTEX.

[31] “PLA (polylactic acid).” https://www.ferben.com/technology/corona/pla-polylactic-acid.kl (accessed May 06, 2023).

[32] T. Vu, P. Nikaeen, W. Chirdon, A. Khattab, and D. Depan, “Improved Weathering Performance of Poly(Lactic Acid) through Carbon Nanotubes Addition: Thermal, Microstructural, and Nanomechanical Analyses,” *Biomimetics*, vol. 5, no. 4, pp. 1–15, Dec. 2020, doi: 10.3390/BIOMIMETICS5040061.

[33] “Is PLA toxic? | Gianeco.” https://www.gianeco.com/en/faq-detail/1/19/is-pla-toxic (accessed May 06, 2023).

[34] S. N, A. K. S, P. A, and G. S, “Studies on Semi-crystalline Poly Lactic Acid (PLA) as a Hydrophobic Coating Material on Kraft Paper for Imparting Barrier Properties in Coated Abrasive Applications,” *Prog Org Coat*, vol. 145, Aug. 2020, doi: 10.1016/j.porgcoat.2020.105682.

[35] P. Shi, B. Niu, S. E, Y. Chen, and Q. Li, “Preparation and characterization of PLA coating and PLA/MAO composite coatings on AZ31 magnesium alloy for improvement of corrosion resistance,” *Surf Coat Technol*, vol. 262, pp. 26–32, Jan. 2015, doi: 10.1016/j.surfcoat.2014.11.069.

[36] J. E. Marshall *et al.*, “On the solubility and stability of polyvinylidene fluoride,” *Polymers*, vol. 13, no. 9. MDPI AG, May 01, 2021. doi: 10.3390/polym13091354.

[37] X. Zhao, J. Zhang, S. Chen, X. Wang, and J. Wang, “Effect of PPEGMA content on the structure and hydrophilicity of PVDF/PPEGMA blends prepared by in situ polymerization,” *Colloid Polym Sci*, vol. 291, no. 7, pp. 1573–1580, Jul. 2013, doi: 10.1007/s00396-013-2891-3.

[38] X. Chen, X. Han, and Q. D. Shen, “PVDF-Based Ferroelectric Polymers in Modern Flexible Electronics,” *Advanced Electronic Materials*, vol. 3, no. 5. Blackwell Publishing Ltd, May 01, 2017. doi: 10.1002/aelm.201600460.

[39] “PVDF - Polyvinlylideenfluoride | Vink Kunststoffen.” https://www.vinkkunststoffen.nl/kunststofsoorten/pvdf-polyvinylideenfluoride (accessed Apr. 02, 2023).

[40] “PVDF - Polyvinylidenfluoride - Electrisol Kunststoffen.” https://electrisol.nl/kunststof-materialen/pvdf-polyvinylidenfluoride/ (accessed Apr. 02, 2023).

[41] G. Peng *et al.*, “Effects of a New Crystal Structure of Poly(Vinylidene Fluoride-Hexafluoropropylene)/Poly(Mathyl Methacrylate) Blend Films on Discharge Efficiency”, Accessed: Apr. 25, 2023. [Online]. Available: www.rsc.org/advances

[42] “What is PVDF Plastic? | The Ultimate Guide - PlasticRanger.” https://plasticranger.com/what-is-pvdf/ (accessed Apr. 25, 2023).

[43] N. Kusumawati, P. Setiarso, S. Muslim, and N. Purwidiani, “Synergistic ability of PSf and pvdf to develop high-performance PSf/PVDF coated membrane for water treatment,” *Rasayan Journal of Chemistry*, vol. 11, no. 1, pp. 260–279, Jan. 2018, doi: 10.7324/RJC.2018.1112018.

[44] S. Zhang, L. Wu, F. Deng, D. Zhao, C. Zhang, and C. Zhang, “Hydrophilic modification of PVDF porous membrane: Via a simple dip-coating method in plant tannin solution,” *RSC Adv*, vol. 6, no. 75, pp. 71287–71294, 2016, doi: 10.1039/c6ra13634f.

[45] H. Wang *et al.*, “A robust superhydrophobic PVDF composite coating with wear/corrosion-resistance properties,” *Appl Surf Sci*, vol. 332, pp. 518–524, Mar. 2015, doi: 10.1016/j.apsusc.2015.01.213.

[46] C. Peng, S. Xing, Z. Yuan, J. Xiao, C. Wang, and J. Zeng, “Preparation and anti-icing of superhydrophobic PVDF coating on a wind turbine blade,” *Appl Surf Sci*, vol. 259, pp. 764–768, Oct. 2012, doi: 10.1016/j.apsusc.2012.07.118.

[47] S. Shrestha, B. Wang, and P. Dutta, “Nanoparticle processing: Understanding and controlling aggregation,” *Advances in Colloid and Interface Science*, vol. 279. Elsevier B.V., May 01, 2020. doi: 10.1016/j.cis.2020.102162.

[48] S. M. Stavis, J. A. Fagan, M. Stopa, and J. A. Liddle, “Nanoparticle Manufacturing-Heterogeneity through Processes to Products,” *ACS Appl Nano Mater*, vol. 1, no. 9, pp. 4358–4385, Sep. 2018, doi: 10.1021/acsanm.8b01239.

[49] E. Casals, E. Gonzalez, and V. F. Puntes, “Reactivity of inorganic nanoparticles in biological environments: Insights into nanotoxicity mechanisms,” *Journal of Physics D: Applied Physics*, vol. 45, no. 44. Nov. 07, 2012. doi: 10.1088/0022-3727/45/44/443001.

[50] X. Zhao *et al.*, “Environmentally benign and durable superhydrophobic coatings based on SiO 2 nanoparticles and silanes,” *J Colloid Interface Sci*, vol. 542, pp. 8–14, Apr. 2019, doi: 10.1016/j.jcis.2019.01.115.

[51] D. A. Schaeffer, G. Polizos, D. B. Smith, D. F. Lee, S. R. Hunter, and P. G. Datskos, “Optically transparent and environmentally durable superhydrophobic coating based on functionalized SiO2 nanoparticles,” *Nanotechnology*, vol. 26, no. 5, Jun. 2015, doi: 10.1088/0957-4484/26/5/055602.

[52] L. Cao, A. K. Jones, V. K. Sikka, J. Wu, and D. Gao, “Anti-Icing superhydrophobic coatings,” *Langmuir*, vol. 25, no. 21, pp. 12444–12448, Nov. 2009, doi: 10.1021/la902882b.

[53] S. Wang *et al.*, “Preparation of a durable superhydrophobic membrane by electrospinning poly (vinylidene fluoride) (PVDF) mixed with epoxy-siloxane modified SiO2 nanoparticles: A possible route to superhydrophobic surfaces with low water sliding angle and high water contact angle,” *J Colloid Interface Sci*, vol. 359, no. 2, pp. 380–388, Jul. 2011, doi: 10.1016/j.jcis.2011.04.004.

[54] D. Kumar, L. Li, and Z. Chen, “Mechanically robust polyvinylidene fluoride (PVDF) based superhydrophobic coatings for self-cleaning applications,” *Prog Org Coat*, vol. 101, pp. 385–390, Dec. 2016, doi: 10.1016/j.porgcoat.2016.09.003.

[55] A. J. Haider, R. H. Al-Anbari, G. R. Kadhim, and C. T. Salame, “Exploring potential Environmental applications of TiO2 Nanoparticles,” in *Energy Procedia*, Elsevier Ltd, 2017, pp. 332–345. doi: 10.1016/j.egypro.2017.07.117.

[56] Y. Zhao *et al.*, “Synthesis and optical properties of TiO2 nanoparticles,” *Mater Lett*, vol. 61, no. 1, pp. 79–83, Jan. 2007, doi: 10.1016/j.matlet.2006.04.010.

[57] L. Sang, Y. Zhao, and C. Burda, “TiO 2 Nanoparticles as Functional Building Blocks,” 2014, doi: 10.1021/cr400629p.

[58] S. Hamad, C. R. A. Catlow, S. M. Woodley, S. Lago, and J. A. Mejías, “Structure and Stability of Small TiO 2 Nanoparticles,” 2005, doi: 10.1021/jp0521914.

[59] “Skyspring Nanopowder and Nanoparticles.” https://ssnano.com/home---- (accessed May 22, 2023).

[60] “What are volatile organic compounds (VOCs)? | US EPA.” https://www.epa.gov/indoor-air-quality-iaq/what-are-volatile-organic-compounds-vocs (accessed May 22, 2023).

[61] “MATERIAL SAFETY DATA SHEET Acetone, 99+% 95389 **** SECTION 1-CHEMICAL PRODUCT AND COMPANY IDENTIFICATION ****.” [Online]. Available: http://www.fisher1.com/fb/itv?16..f97..msa0001.79..1..

[62] “Schildersziekte Chronische Toxische Encefalopathie (CTE) / Vergiftiging en Middelengebruik / Soorten hersenletsel hersenaandoeningen | Hersenletsel-uitleg.nl.” https://www.hersenletsel-uitleg.nl/soorten-hersenletsel-hersenaandoeningen/vergiftiging-en-middelengebruik/schildersziekte-chronische-toxische-encefalopathie-cte (accessed May 22, 2023).

[63] “Acetone ACS reagent, = 99.5 67-64-1.” https://www.sigmaaldrich.com/BE/en/product/sigald/179124 (accessed May 22, 2023).

[64] J. A. Young, “Chemical Education Today Chloroform CHCl 3,” 2008. [Online]. Available: www.JCE.DivCHED.org

[65] “What Is Chloroform, Cas No 67-66-3 Guide - ECHEMI.” https://www.echemi.com/products/pid_Rock3936-chloroform.html (accessed May 22, 2023).

[66] “The life science business of Merck operates as MilliporeSigma in the US and Canada,” 1907.

[67] M. Lora, J. S. Lim, and M. A. McHugh, “Comparison of the solubility of PVF and PVDF in supercritical CH2F2 and CO2 and in CO2 with acetone, dimethyl ether, and ethanol,” *Journal of Physical Chemistry B*, vol. 103, no. 14, pp. 2818–2822, Apr. 1999, doi: 10.1021/jp9844462.

[68] “Illustrated Glossary of Organic Chemistry - Ethanol.” http://www.chem.ucla.edu/~harding/IGOC/E/ethanol.html (accessed May 22, 2023).

[69] X. M. Li, D. Reinhoudt, and M. Crego-Calama, “What do we need for a superhydrophobic surface? A review on the recent progress in the preparation of superhydrophobic surfaces,” *Chem Soc Rev*, vol. 36, no. 8, pp. 1350–1368, Jul. 2007, doi: 10.1039/b602486f.

[70] X. Zhang, F. Shi, J. Niu, Y. Jiang, and Z. Wang, “Superhydrophobic surfaces: From structural control to functional application,” *J Mater Chem*, vol. 18, no. 6, pp. 621–633, 2008, doi: 10.1039/b711226b.

[71] M. Miwa, A. Nakajima, A. Fujishima, K. Hashimoto, and T. Watanabe, “Effects of the surface roughness on sliding angles of water droplets on superhydrophobic surfaces,” *Langmuir*, vol. 16, no. 13, pp. 5754–5760, Jun. 2000, doi: 10.1021/la991660o.

[72] J. Anthony Von Fraunhofer, “Adhesion and Cohesion,” *Int J Dent*, vol. 2012, 2012, doi: 10.1155/2012/951324.

[73] X. C. Z. K. Designed Research; T, X. C. Z. K. Performed Research; T, and T. E. Pnas, “Coexistence and transition between Cassie and Wenzel state on pillared hydrophobic surface,” 2009.

[74] “Theory of Wetting Action at Solid Surfaces.”

[75] A. B. D. Cassie and S. Baxter, “Wettability of porous surfaces,” *Transactions of the Faraday Society*, vol. 40, pp. 546–551, 1944, doi: 10.1039/tf9444000546.

[76] “5.4: Hydrolysis Reactions - Chemistry LibreTexts.” https://chem.libretexts.org/Courses/Georgia_Southern_University/CHEM_1152%3A_Survey_of_Chemistry_II_(GSU_-_Dr._Osborne)/05%3A_Organic_Chemical_Reactions/5.04%3A_Hydrolysis_Reactions (accessed May 06, 2023).

[77] “Hydrolysis | Definition, Examples, & Facts | Britannica.” https://www.britannica.com/science/hydrolysis (accessed May 06, 2023).

[78] M. Shakourian, S. Rahemi Ardekani, A. Bayat, E. Saievar-Iranizad, and W. Deferme, “Ultrasonic atomization based fabrication of superhydrophobic and corrosion-resistant hydrolyzed MTMS/PVDF coatings,” *JCIS Open*, vol. 7, Oct. 2022, doi: 10.1016/j.jciso.2022.100059.

[79] S. R. Ardekani, A. S. Rouh Aghdam, M. Nazari, A. Bayat, and E. Saievar-Iranizad, “A new approach for preparation of semi-transparent superhydrophobic coatings by ultrasonic spray hydrolysis of methyltrimethoxysilane,” *Prog Org Coat*, vol. 135, pp. 248–254, Oct. 2019, doi: 10.1016/j.porgcoat.2019.05.033.

[80] B. Xu and Q. Zhang, “Preparation and Properties of Hydrophobically Modified Nano-SiO2with Hexadecyltrimethoxysilane,” *ACS Omega*, vol. 6, no. 14, pp. 9764–9770, Apr. 2021, doi: 10.1021/acsomega.1c00381.

[81] “Contact Line Pinning - FLOW-3D v12.0 Development.” https://www.flow3d.com/modeling-capabilities/contact-line-pinning/ (accessed Nov. 11, 2022).

[82] R. D. Deegan, O. Bakajin, T. F. Dupont, G. Huber, S. R. Nagel, and T. A. Witten, “Capillary flow as the cause of ring stains from dried liquid drops.”

[83] J. H. Adair, E. Suvaci, and J. Sindel, “Surface and Colloid Chemistry,” *Encyclopedia of Materials: Science and Technology*, pp. 1–10, Jan. 2001, doi: 10.1016/B0-08-043152-6/01622-3.

[84] D. Instruments GmbH, “Optical contact angle measuring and contour analysis systems ranging from basic device to fully automated measuring systems for micro-structured samples”.

[85] “Contact Angle Measurement System OCA 15/20 – Wisconsin Centers for Nanoscale Technology – UW–Madison.” https://wcnt.wisc.edu/soft-materials-characterization-lab/oca-contact-angle-measurement-tool/ (accessed Apr. 23, 2023).

[86] “Dataphysics OCA15 Pro.” http://www.pss.aus.net/index.php?option=com_content&view=article&id=229&Itemid=142 (accessed Apr. 23, 2023).

[87] “OCA Optical contact angle measuring and contour analysis systems - DataPhysics Instruments.” https://www.dataphysics-instruments.com/products/oca/ (accessed Apr. 23, 2023).

[88] “OCA 15 EC - optical contact angle measuring instrument - Norleq.” https://norleq.com/en/produtos/oca-15-ec-optical-contact-angle-measuring-instrument/ (accessed Apr. 23, 2023).

[89] D. Instruments GmbH, “O C A 1 0 0 / 1 0 0 M i c r o.” [Online]. Available: www.dataphysics.de

[90] “Drop And Surface Analyzer (DASA) - Departement Materiaalkunde.” https://www.mtm.kuleuven.be/equipment/surfaces-interfaces-analysis/DASA/dasa (accessed Jun. 08, 2023).

[91] “DektakXT | Bruker.” https://www.bruker.com/en/products-and-solutions/test-and-measurement/stylus-profilometers/dektakxt.html?medium=cpc_search_SOM&campaign=SOM_Search&source=151530139132&keyword=dektak%20profilometer&device=c&s_kwcid=AL!14677!3!648966572604!p!!g!!dektak%20profilometer&gclid=EAIaIQobChMI8rm-iJbA_gIVC4ODBx0OMgSmEAAYASABEgIvCfD_BwE (accessed Apr. 23, 2023).

[92] “DektakXT Stylus Profiler 10 th Generation Stylus Profiling System Stylus Metrology Innovation with Integrity”.

[93] “What is a Profilometer? | GD&T Basics.” https://www.gdandtbasics.com/what-is-a-profilometer/ (accessed Apr. 23, 2023).

[94] “Profilometry - Nanoscience Instruments.” https://www.nanoscience.com/techniques/profilometry/ (accessed Apr. 23, 2023).

[95] “What is Optical Microscopy?” https://www.news-medical.net/life-sciences/What-is-Optical-Microscopy.aspx (accessed Apr. 23, 2023).

[96] “Zeiss Axiovert 25/40 MAT Microscope Light – Nanodyne Measurement Systems.” https://www.nano-dyne.com/led-microscope-lights/zeiss-axiovert-25-40-mat-microscope-light/ (accessed Apr. 23, 2023).

[97] “Zeiss Axiovert 40 mat inverted digital microscope.” https://www.cmrdi.sci.eg/pdd/Zeiss%20Axiovert%2040%20mat%20inverted%20digital%20microscope.html (accessed Apr. 23, 2023).

[98] “Scanning Electron Microscopy (SEM).” https://serc.carleton.edu/research_education/geochemsheets/techniques/SEM.html (accessed Apr. 23, 2023).

[99] “Scanning Electron Microscopy - Nanoscience Instruments.” https://www.nanoscience.com/techniques/scanning-electron-microscopy/ (accessed Apr. 23, 2023).

[100] "Scanning electron microscope (SEM) | Definition, Images, Uses, Advantages, & Facts | Britannica." https://www.britannica.com/technology/scanning-electron-microscope (accessed Apr. 23, 2023).